GDAŃSK UNIVERSITY OF TECHNOLOGY

The author of the doctoral dissertation: Hanna Świątek
Scientific discipline: Materials Engineering

DOCTORAL DISSERTATION

Title of doctoral dissertation: Synthesis and investigation of physical properties of selected ternary pnictide compounds

Title of doctoral dissertation (in Polish): Synteza i badania właściwości fizycznych wybranych trójskładniokowych pniktydków

Supervisor *signature*
prof. dr hab. inż. Tomasz Klimczuk

Gdańsk, year 2025

Abstract

The subject of this thesis is the synthesis and investigation of physical properties of selected families of ternary pnictides.

The first investigated group of materials are the equiatomic ATPn compounds, where A is a divalent alkaline earth or rare earth metal, T is a group 11 transition metal and Pn is a pnictogen. The main focus of this work was to develop and optimize synthesis methods for obtaining high-quality single crystals, which would allow for further study of their electronic structure and potential non-trivial topological properties. Single crystals of 10 compounds were obtained from liquid phase (flux) growth. Physical properties, such as electrical resistivity, heat capacity and magnetization, were examined for selected samples. The metal-like resistivity and the Sommerfeld coefficient values $\gamma \sim 0$ are consistent with the characteristics expected for topological semimetals. The second family, for which single crystals growth was conducted, are the $A\mathrm{Mg}_2Pn_2$ materials, where A = Sr, Ba and Pn = Sb, Bi. For the first time, the antimonides were grown in the form of bulk crystals. Measurements oh heat capacity showed low values of γ for all of the investigated compounds.

The last part of this thesis describes the synthesis and physical properties of a new superconducting material $\mathrm{Mg_4Pd_7As_6}$. Studies of electrical resistivity, heat capacity and magnetization show that it is a type-II superconductor with a critical temperature T_c = 5.5 K. The obtained electron-phonon coupling parameter indicated moderate coupling (λ = 0.72). Attempts to synthesize other members of the 4-7-6 family are described. The obtained compounds were tested for superconductivity, however, it was not observed in any of the samples (above T = 1.9 K). $\mathrm{Mg_4Pd_7As_6}$ is the first superconductor in the 4-7-6 family and at this stage of the research remains the only one.

The materials described in this thesis are an example of the variety of physical properties that can be encountered in the ternary systems containing pnictogen atoms.

Streszczenie

Przedmiotem niniejszej rozprawy są synteza i badania właściwości fizycznych wybranych grup trójskładnikowych pniktydków.

Pierwsza badana grupą materiałów to związki $ATPn$, gdzie A to dwuwartościowy metal ziem alkalicznych lub rzadkich, T to metal przejściowy 11. grupy, a Pn to pniktogen. Część badań poświęcona tej rodzinie skupiła się głównie na opracowaniu i optymalizacji metod otrzymywania wysokiej jakości monokryształów, co pozwoliło na ich dalsze badania mające na celu określenie ich struktury elektronowej i potencjalnych nietrywialnych właściwości topologicznych. Kryształy 10 związków $ATPn$ otrzymano przy użyciu metody wzrostu z fazy ciekłej (wzrost przy użyciu topnika). Dla wybranych próbek zostały przebadane właściwości fizyczne, takie jak rezystywność, ciepło właściwe i magnetyzacja. Wykazywany przez materiały metaliczny charakter przewodnictwa i bliskie zeru wartości parametru Sommerfelda γ są zgodne z oczekiwanymi dla półmetali topologicznych. Drugą grupą materiałów, których monokryształy otrzymano, są związki $A\mathrm{Mg}_2Pn_2$, gdzie A = Sr, Ba i Pn = Sb, Bi. Kryształy zawierające antymon po raz pierwszy zostały otrzymane w formie objętościowej. Przeprowadzone pomiary ciepła właściwego wykazały niskie wartości parametru γ dla wszystkich przebadanych związków.

Ostatnia część pracy opisuje syntezę i właściwości fizyczne nowego materiału nadprzewodzącego $\mathrm{Mg_4Pd_7As_6}$. Badania oporu elektrycznego, ciepła właściwego i magnetyzacji wykazały, że $\mathrm{Mg_4Pd_7As_6}$ jest nadprzewodnikiem II-rodzaju o temperaturze krytycznej T_c = 5,5 K. Wartość sprzężenia elektron-fonon wskazuje na umiarkowane sprzężenie (λ = 0,72). Rozprawa zawiera opis prób syntezy wybranych związków o stechiometrii 4-7-6. Otrzymane materiały zostały przetestowane pod kątem nadprzewodnictwa, jednak nie zostało ono wykryte w żadnej z próbek (powyżej temperatury 1,9 K). $\mathrm{Mg_4Pd_7As_6}$ jest pierwszym, i na tym etapie badań jedynym, nadprzewodnikiem w rodzinie związków 4-7-6.

Materiały opisane w rozprawie są przykładem różnorodności właściwości występujących w układach trójskładnikowych zawierającyh atomy pniktogenów.

Contents

Chapter 1

Aim and scope of the work

As the development and advancement of current technologies heavily depends on discovery of new materials, the search for novel, interesting compounds is an on-going endeavor. After years of research, many binary compounds are known and fully characterized, resulting in a need to focus on more complicated systems. Ternary compounds, as the next simplest group, offer much more variety without introducing excessive complexity. Thus, the main aim of the conducted research was to investigate selected families of ternary pnictide compounds containing alkaline earth metals or rare earth metals. As the "ternary pnictide" classification encompasses a large variety of compounds, the specific families were chosen based on the interesting physical properties they exhibit: the sought-after properties were superconductivity or potentially non-trivial topological character.

The discovery of topological materials in the recent years has opened up a new frontier in the study of condensed-matter physics. Moreover, the theoretical predictions have brought on renewed interest in materials that, in many cases, have been known for years. The experimental confirmations are, however, hindered by the lack of high-quality single-crystal samples which are necessary for detailed characterization. Hence, the first stage of the work focused on developing or optimizing single crystal growth of two families of materials: equiatomic $ATPn$ compounds with valence electron count of 18, where A = alkaline earth metal or Yb/Eu, T = group 11 transition metal, Pn = As, Bi, Sb, and layered $A\mathrm{Mg}_2Pn_2$ compounds where A = Ba, Sr and Pn = Sb or Bi.

The second part of the work focused on the search for new superconducting compounds crystallizing in the cubic $\mathrm{U}_4\mathrm{Re}_7\mathrm{Si}_6$ structure. It should be noted that superconductivity has not previously been revealed in any of the materials in this family.

Chapter 2

Introduction

2.1 Quantum materials

The advancement of new technologies has always been driven, to a large degree, by development of new materials. The rapid progress and newly-arising challenges require a constantly on-ongoing search for novel materials, able to meet the requirements.

Many of the currently investigated, promising classes of materials can be brought together under the umbrella term of "quantum materials". This broad classification is generally taken to mean materials which exhibit novel physical properties, which cannot be approximated by classical description. These exotic properties can arise due to the collective nature of the electrons in the system caused by unique electron correlations, often underlined by magnetism and observed in systems with partially filled d- or f-electron shells. Interesting properties can also often be observed in systems with reduced dimensionality, for example due to confinement of electrons to sheets in 2-dimensional materials [1, 2].

This diverse category includes both the more well-know materials such as graphene or superconductors, and the more recent additions such as spin ices, quantum spin liquids and topologically non-trivial materials [3, 1]. These materials find application in many fields, including electronics, information and computational technologies, energy usage and storage. Figure 2.1 presents a non-exhaustive list of some quantum phenomena exhibited by different classes of materials, together with their potential technological applications.

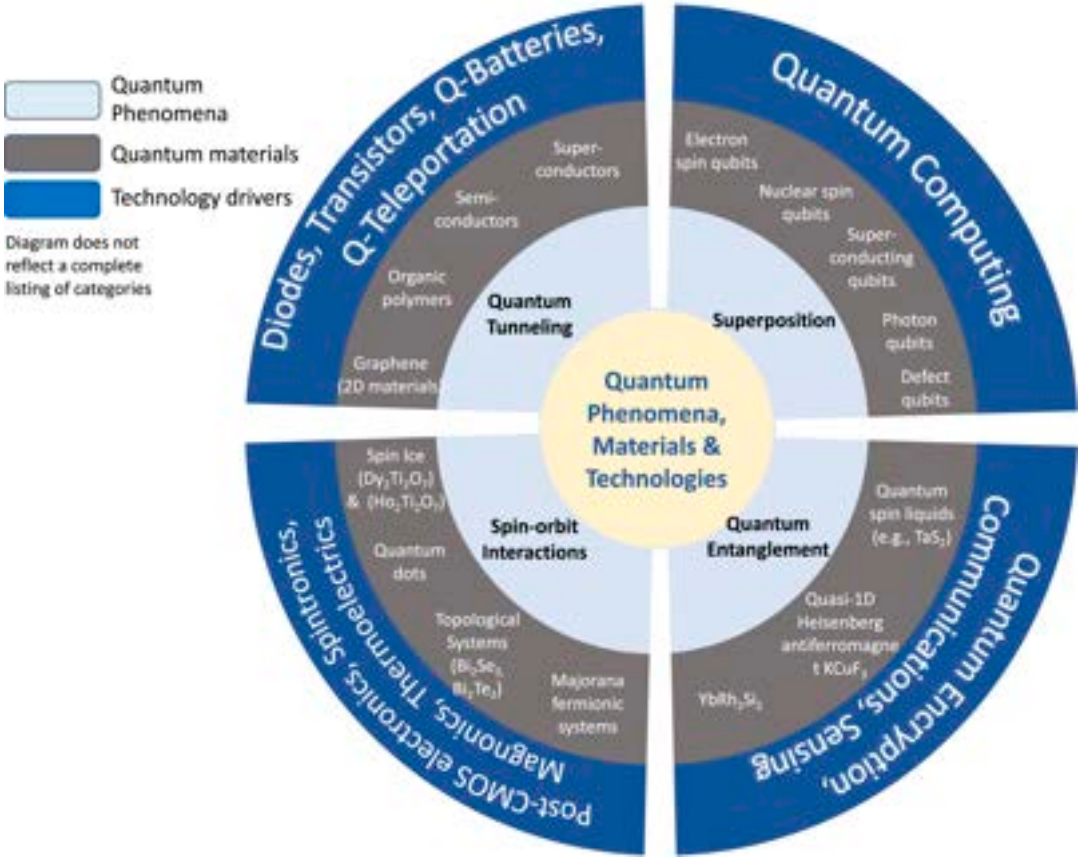

FIGURE 2.1: Correlations of select quantum phenomena with recently developed materials that effectively illustrate quantum behaviors and the technologies in which they can be applied. Reprinted from [4] under CC-BY license (Copyright 2024 Harris and Andalib).

2.2 Topological materials

Study of topologically non-trivial materials is a thriving field in condensed matter physics of the 21^{st} century. These materials exhibit unique physical properties, which can be understood using insights from the mathematical field of topology (which is concerned with properties that are invariant under continuous deformations). The foundation of the current research lies in the studies dating back to the early 1980s, related to the integer quantum Hall effect (QHE) in 2-dimensional systems in strong magnetic fields [5, 6]. Near the end of the decade, a new model for QHE in the absence of an external magnetic field was developed [7], proposing how the effect could instead arise from the movement of electrons through the crystal lattice. This model turned out to be crucial for developing a new class of materials: topological insulators.

A significant theoretical advancement came after the turn of the century

[8, 9, 10], and soon after the first experimental realisations of topological insulators followed [11, 12, 13, 14]. The main characteristic of these materials is the presence of an energy gap, making the material insulating in the bulk, coupled with the presence of conducting edge/surface states. The conducting states are topologically-protected, making them immune to defects or surface imperfections.

In the following years, the field of topological materials expanded to new classes of materials, such as topological superconductors and topological semimetals. The latter are characterized by the presence of robust bulk band crossing points. Depending on whether the bands are degenerate or not, the materials can be divided into Dirac semimetals (DSM) or Weyl semimetals (WSM), respectively. In case of a 1-dimensional crossing (as opposed to a 0D point crossing), the material is defined as a nodal-line semimetal [15]. A comparison of the band crossings is presented in Figure 2.2.

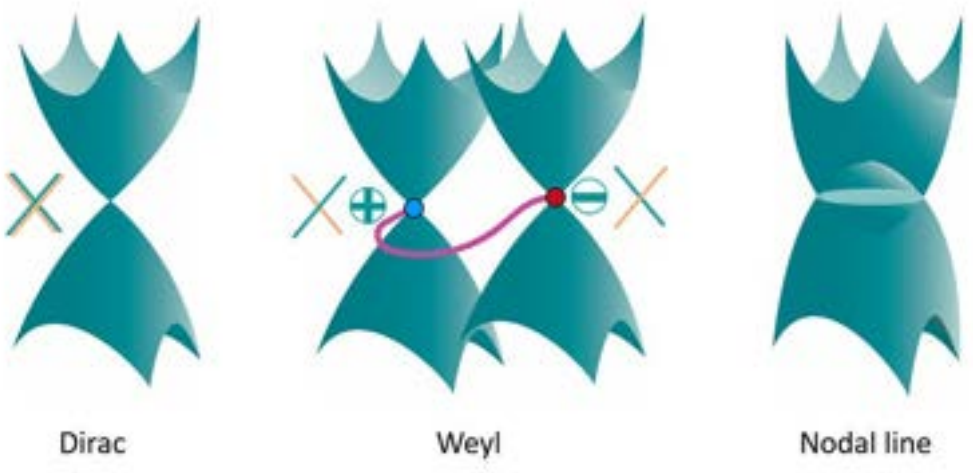

FIGURE 2.2: Schematic representation of band crossing in Dirac, Weyl, and Nodal line semimetal. Positive and negative signs indicate the opposite chirality of the Weyl points. Adapted from [15] under CC-BY license (Copyright 2020 American Chemical Society).

In 2019, the results of a high-throughput search for topological phases among the 'high-quality' materials (defined by the authors as those for which the atomic positions and structure are precisely determined in the Inorganic Crystal Structure Database) were reported [16], building on the previously developed theory of topological quantum chemistry [17]. The investigation indicated that topologically non-trivial materials are not just rare anomalies, but that almost 30 % of the considered compounds are topological in some

way (with roughly 12 % being topological insulators).

Even though many compounds have been predicted to host non-trivial topological states, experimental confirmations are less common, as high-quality single crystals are needed for the measurement techniques necessary to investigate the electronic structure of materials.

2.3 Superconductivity

The first discovery of superconductivity dates back to 1911 and was reported by a Dutch physicist Heike Kamerlingh Onnes. It followed his first successful attempt of liquefying helium three years prior, thus opening a new chapter of low-temperature physics. The phenomenon was detected as an unexpected sharp drop in the electrical resistance versus temperature measurement of a mercury sample occurring at 4.2 K. The recorded data can be seen in Figure 2.3(a). The same behaviour was shortly after observed for lead and tin (near 7.2 K and 3.7 K, respectively). The temperature of this transition to a zero resistivity state, called the critical temperature T_c, is one of the main characteristics of a superconducting material. In pure materials this transition should occur in a narrow range of temperature and broader transition indicates poor quality of the sample.

Another fundamental property of superconducting materials was first discovered over 20 years later by Meissner and Ochsenfeld. When an external magnetic field is applied to a superconductor, screening currents are induced within a thin layer close to the surface, generating a field opposite in direction and equal in strength. As this exactly cancels the external field, the magnetic field is not simply prevented from entering (as would be the case for a "perfect" conductor) but completely expelled from within the material if the temperature is below T_c. This is illustrated in Figure 2.3(b). In other words, the magnetic flux density inside the bulk of a superconductor is equal to zero ($B = 0$) and its magnetization can be described by the equation $H = -M$, leading to a magnetic susceptibility $\chi = -1$. This perfectly diamagnetic response of a superconductor is now commonly referred to as the Meissner effect.

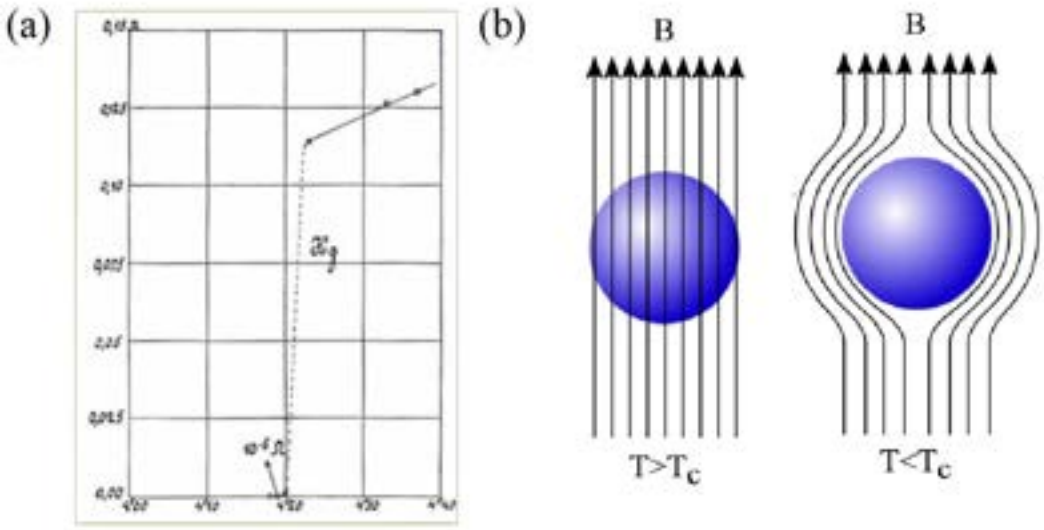

FIGURE 2.3: (a) The first ever recorded superconducting transition, observed for a sample of mercury [18](b) Illustration of the Meissner effect for a sample in external magnetic field as the temperature is lowered below T_c [19].

This property, however, also has its limit. If the external magnetic field is strong enough the superconductor will transition into the normal state, even when the temperature is below T_c. The relation between this critical magnetic field H_c and T_c can be approximated using the equation:

$$H_c(T) = H_c(0)\left(1 - \left(\frac{T}{T_c}\right)^2\right) \tag{2.1}$$

where $H_c(0)$ is the critical field at $T = 0$ K.

As more superconducting elements (and compounds) were discovered, a different reaction to external magnetic field started being observed. These materials were then referred to as type-II superconductors. In low fields, the material behaves as previously expected for type-I superconductor, exhibiting perfect diamagnetism. When a certain value, called the lower critical field H_{c1}, is exceeded, the magnetic flux starts to penetrate the bulk of the material. The superconductor is then said to be in a mixed state (also referred to as a vortex state). The flux vortices can move throughout the material (unless they get pinned in place by inhomogeneities) and tend to arrange in a regular pattern. Their density increases with the external magnetic field, until at a certain point, corresponding to the upper critical field H_{c2}, the material is driven to the normal state. The comparison of magnetization of type-I and

type-II superconductors is presented in Figure 2.4. Metals tend to be superconductors of type I (with the exception of Nb, V and Tc), while an overwhelming majority of alloys show type II superconductivity.

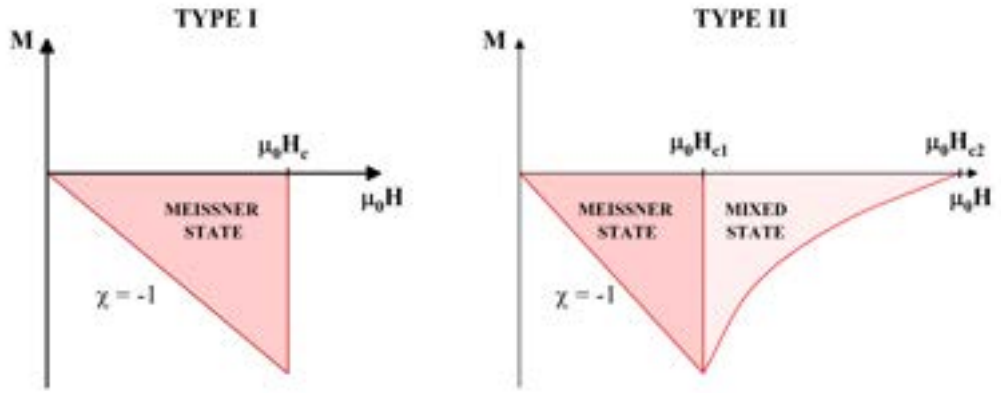

FIGURE 2.4: Comparison of magnetization for type I and type II superconductors.

The final critical parameter capable of destroying superconductivity is the density of electric current J_c. Thus, the material can only exist in the superconducting state when the values of all three of these parameters are within a well-defined range. This connection can be seen in Figure 2.5, which presents the boundary between the normal and superconducting state of the material.

The electrodynamics of superconductors are well-described by the phenomenological theory, proposed by the London brothers in the 1930s [20]. Most notably, it correctly describes the Meissner effect and introduces the concept of a characteristic penetration depth, which defines the distance up to which the magnetic field is able to penetrate the sample. It is one of the characteristic scales of a superconductor. The magnetic field within the material diminishes exponentially according to:

$$B(x) = B_0 \exp\left(\frac{-x}{\lambda_L}\right) \tag{2.2}$$

where $B(x)$ is the magnetic induction at a distance x from the surface and λ_L is the London penetration depth. Within this distance, the field is reduced by a factor of e and vanishes in the bulk of the material. The relation is presented in Figure 2.6.

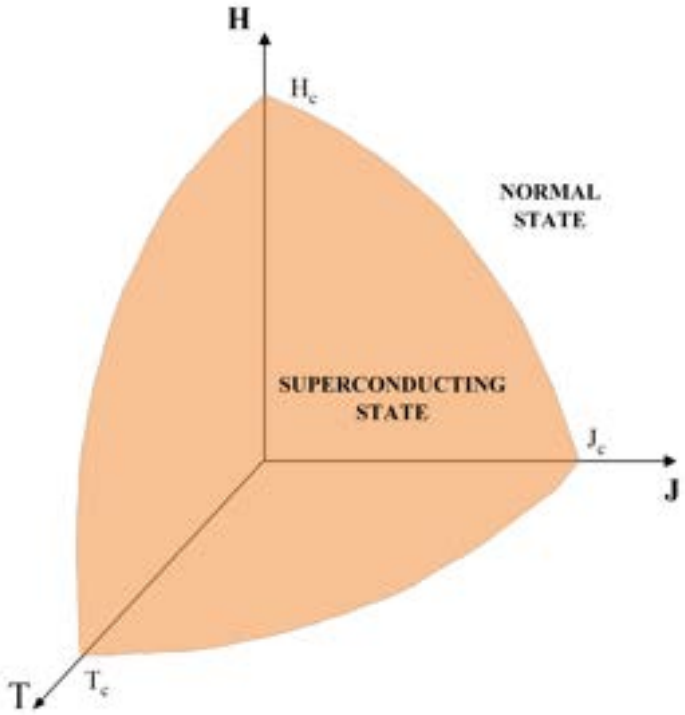

FIGURE 2.5: The relation between the critical parameters, forming the J-H-T surface separating the superconducting state from the normal one.

λ_L can be defined as:

$$\lambda_L = \sqrt{\frac{m_e}{\mu_0 n_s e^2}}, \tag{2.3}$$

where m_e - electron mass, μ_0 - vacuum permeability, n_s - superconducting electron density and e - electron charge.

A second important, phenomenological theory was proposed in the 1950s by V. L. Ginzburg and L. D. Landau [21], based on the theory of second-order phase transitions. It introduced an order parameter $\Phi(r)$, related to the local density of superconducting electrons (n_s). The value of this parameter can change only gradually over a certain characteristic distance ξ_{GL}, called the coherence length, which is the second characteristic scale of a superconducting material. As this theory allows for the n_s to change, a temperature dependence of λ_L could now be defined as:

$$\lambda(T) = \sqrt{\frac{2b}{\mu_0 a(T_c - T)} \cdot \frac{m_e}{2e^2}}, \tag{2.4}$$

where a and b are positive coefficients.

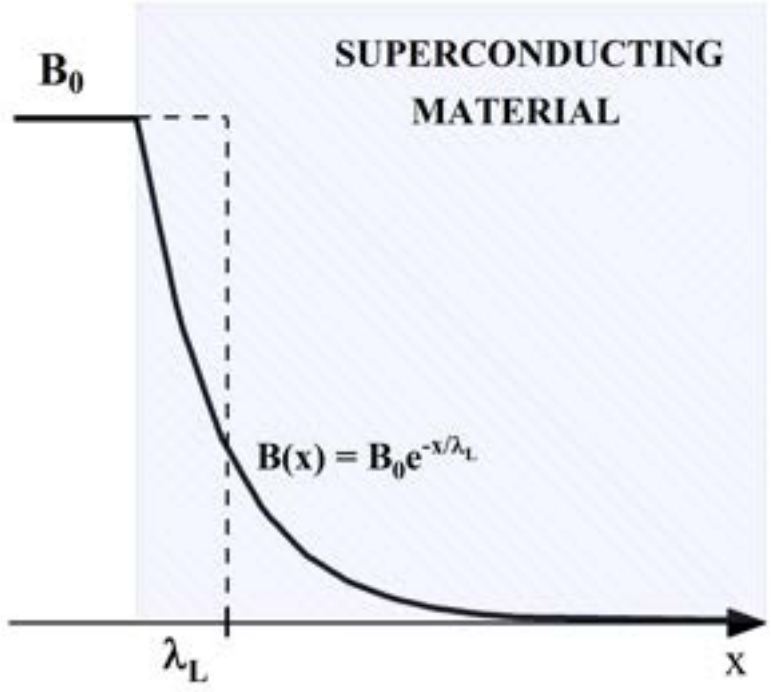

FIGURE 2.6: Penetration of magnetic flux into a superconductor.

The relation between these two characteristic scales can be expressed in terms of the Ginzburg-Landau parameter κ_{GL} defined as:

$$\kappa_{GL} = \frac{\lambda_{GL}}{\xi_{GL}}. \tag{2.5}$$

The obtained value of κ_{GL} is used to classify the type of the superconductor, with $\kappa_{GL} < \frac{1}{\sqrt{2}}$ corresponding to type-I superconductors and above that for type-II. κ_{GL} can also be used to relate the values of upper and lower critical field for type-II superconductors, according to:

$$H_{c1} H_{c2} = H_c^2 \ln \kappa \tag{2.6}$$

where H_c is the thermodynamic critical field, which can be understood as an approximate critical field of a given superconductor, if it were of a type-I instead.

The 1950s also brought the first microscopic theory of superconductivity, later known as BCS theory, proposed by John Bardeen, Leon Cooper, and John R. Schrieffer [22, 23]. The foundation of the theory is the existence

of a phonon-mediated attractive interaction between two electrons, resulting in a creation of Cooper pairs. In a simplified view, an electron moving through a crystal lattice causes a disturbance in the charge distribution of the positively-charged atom cores. This local increase of positive charge attracts a second electron, with an opposite spin and momentum. Such interaction between the two electrons leads to a decrease in energy of the system and leads to an opening of a superconducting energy gap.

The BCS also lead to the following relation for the critical temperature T_c:

$$T_c = 1.13\frac{\hbar\omega_D}{k_B}\exp\left(-\frac{1}{N(E_F)V}\right) \tag{2.7}$$

where k_B is the Boltzmann constant, ω_D is the Debye frequency, $N(E_F)$ is the density of state at the Fermi level and V is the Cooper pair interaction.

Another important contribution of the BCS theory is the derivation of the relation between the critical temperature and the energy gap $\Delta(0)$:

$$2\Delta(0) = 3.52k_BT_c \tag{2.8}$$

The discussed parameters are important for characterizing any new superconductor. They can generally be obtained from three basic measurements: electrical resistivity, magnetization and heat capacity.

2.4 Overview of the families of the investigated compounds

2.4.1 *ATPn*

According to a survey published by Fornasini and Merlo in 1995, close to a 1000 ATX compounds have been reported, where A is a trivalent rare earth metal, and almost 300 where A is a divalent alkaline earth metal or Eu/Yb, with T and X being a d- and p-block element, respectively [24].

First reports of successful synthesis and crystal structures of equiatomic ternary pnictide compounds (ATX, where X = Pn) come from 1970s [25, 26, 27, 28], with even more compounds reported throughout the next two decades [29, 30]. A large series of 19 compounds where A = Ca, Sr, Ba, Eu,

Yb; T = Cu, Ag, Au and Pn = Sb, Bi comes from a study published by Merlo et al. in 1990. [30]. A majority of these compounds are charge balanced, with a valence electron count VEC = 18, corresponding to a closed-shell configuration. Together with the previously reported compounds, all of them were found to crystallize in one of the following five structure types: ZrBeSi (hexagonal, s.g. $P6_3/mmc$, no. 194), LiGaGe (hexagonal, s.g. $P6_3mc$, no. 186), ZrNiAl (hexagonal, s.g. $P\bar{6}2m$, no. 189), TiNiSi (orthorhombic, s.g. Pnma, no. 62) or MgAgAs (half-Heusler-type structure, cubic, s.g. $F\bar{4}3m$, no. 216). The given structures can be considered to be the ternary ordered variants of Ni_2In, $CaIn_2$, Fe_2P, $PbCl_2$ and CaF_2, respectively, and with the exception of the cubic structure, all the remaining ones can be easily derived from the well-known layered AlB_2 aristotype, through a series of symmetry-reducing distortions or ordering on B-sites. A simplified scheme of these relations is presented in Figure 2.1, while comprehensive descriptions are given in [31, 32].

A phase diagram of crystal structures of compounds containing alkaline earth metals in relation to the radii of the constituent elements can be found in [34]. Structure types of several compounds are marked as "not known", however, based on other reports, both SrAuP and SrAuAs were found to crystallize in the ZrBeSi-type structure as well [29], while MgAgSb is tetragonal at room temperature but adopts the cubic half-Heusler structure above 360 °C [35]. Examples of compounds crystallizing in different crystal structures are presented in Table 2.1.

In a later report by Merlo et al. electrical resistivity of selected Bi-bearing compounds was investigated, however, the measurements were only conducted down to 10 K [36]. Generally, all of the investigated compounds showed metallic temperature dependence, with CaCuBi and YbCuBi showing anomalous jumps in their resistivity curves, with non-linear behavior and negative curvature below 150 K.

A more recent work by Xu et al. [37] presents a crystal growth protocol for 9 $ATPn$ compounds (A = Ca, Sr, Ba; T = Ag, Au; Pn = As, Bi). Electrical resistivity measurements show them all to be metallic, with low residual resistivity ratios (RRR < 5). Additionally, a resistivity drop signifying a possible superconducting transition is observed around 6 and 4 K, for SrAgBi and BaAgBi respectively. Signs of "filamentary" superconductivity in SrAgBi

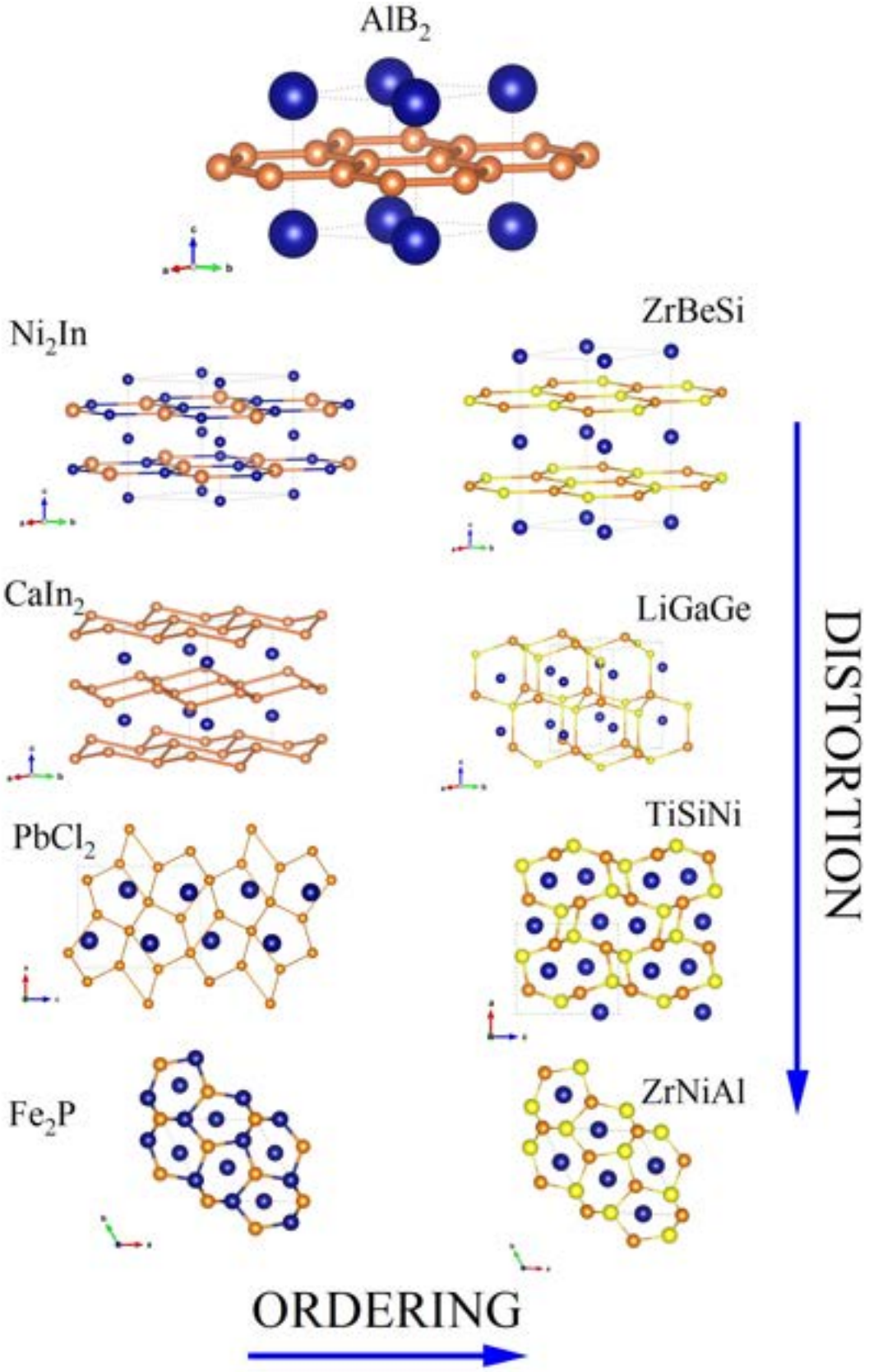

FIGURE 2.7: Common crystal structures of ternary 111 compounds with their related binary variants. Image created using VESTA [33].

TABLE 2.1: Examples of 111 pnictide compounds crystallizing in ZrBeSi, LiGaGe, ZrNiAl and TiSiNi-type structures.

ZrBeSi	LiGaGe	ZrNiAl	TiSiNi
P63/mmc (194)	P63mc (186)	P62m (189)	Pnma (62)
BaAgBi	CaAgBi	CaAgAs	CaAgSb
BaAgAs	YbAgBi	CaAgP	MgCuP
CaAuAs	YbCuBi (RT)		MgCuAs
CaCuSb			
SrAgAs			
SrAgBi			
SrAuBi			
SrAuAs			
YbCuBi (HT)			

were also reported in [38], however, the transition was observed at a lower temperature of 2.9 K. Surface superconductivity at T_c = 2.1 K was reported for SrCuBi (increasing to 4.8 K under pressure) [39] and at T_c = 2.4 K for SrAuBi [40]. In all three mentioned compounds the transition was observed in the electrical resistivity and magnetization measurements, with no jump detected in the specific heat data.

Several of the members of the *ATPn* family containing alkaline earth metals have also been predicted to host various topological phases. BaTBi (T=Au, Ag and Cu), BaAgAs, SrAgAs and SrAgBi have been proposed as 3D DSMs [41, 42, 43, 44, 45, 46]. SrAgBi has subsequently been confirmed to be a spin-orbit coupling-induced type-II 3D DSM [47], while magnetoresistance measurements of SrAgAs showed Shubnikov-de Haas oscillations [48]. The coexistence of three different Dirac points has been predicted in CaAgBi by Chen et al. [49], which could provide a great opportunity to study the interplay between them, if it became verified experimentally. CaAgAs has been predicted to be a nodal line semimetal (converting to topological insulator, upon considering spin-orbit coupling) [50], with experimental works reporting typical metallic resistivity behavior, abundance of p-type carriers and bulk valence band crossing the Fermi level at the Γ-point [51, 52].

2.4.2 $A\mathrm{Mg_2}Pn_2$

$A\mathrm{Mg_2}Pn_2$ compounds belong to the larger family of layered AM_2Pn_2 phases. While several compounds with this stoichiometry have been found to adopt the I4/mmm, Pnma, R$\bar{3}$m or P4/mmm space groups, a significant majority (including all of the Mg-bearing compounds) crystallizes in the trigonal $\mathrm{CaAl_2Si_2}$-type crystal structure (s.g. P$\bar{3}$m1, no. 164). The bonding in these compounds can be understood through Zintl formalism, with a charge transfer from the electropositive A^{2+} layer to the covalently bonded $[\mathrm{Mg_2}Pn_2]^{2-}$ layer, resulting in charge-balanced formulas. The crystal structure can also be described in relation to the binary compound $\mathrm{Mg_3Sb_2}$ (which can be thought of as $\mathrm{MgMg_2Sb_2}$), where 2 crystallographically distinct Mg sites are present. Substitution of A atoms in place of the Mg(1) atoms, which constitute the layer in-between the $[\mathrm{Mg_2Sb_2}]^{2-}$ slabs, increases the c/a lattice parameter ratio and lengthens the interlayer distances. This leads to the anisotropic properties of the ternary compounds, as opposed to $\mathrm{Mg_3Sb_2}$, which should not be considered a layered compound as both Mg(1)-Sb and Mg(2)-Sb are covalently bonded with similar bond strength [53]. The two structures are presented in Figure 2.8.

A series of 9 Mg-bearing compounds $A\mathrm{Mg_2}Pn_2$, where A = Ca, Sr, Ba and Pn = As, Sb, Bi, was reported by Deller and Eisenmann in 1977 [54]. Another 13 AM_2Pn_2 compounds, where M = Zn, Cd, Mg, were reported a few years later by Klüfers et al., extending the family by several phosphides as well as replacing the alkaline earth metals by rare earth metals (Eu, Yb, Lu, Y) [55].

In 2011, structure and physical properties of single crystals of three bismuthides, $\mathrm{CaMg_2Bi_2}$, $\mathrm{EuMg_2Bi_2}$ and $\mathrm{YbMg_2Bi_2}$, were investigated by May et al. [56]. $\mathrm{EuMg_2Bi_2}$ was found to order antiferromagnetically around 7 K, while $\mathrm{YbMg_2Bi_2}$ showed only weak diamagnetic moment, suggesting a divalent (non-magnetic) state of Yb. All three of the compounds were found to be p-type conductors.

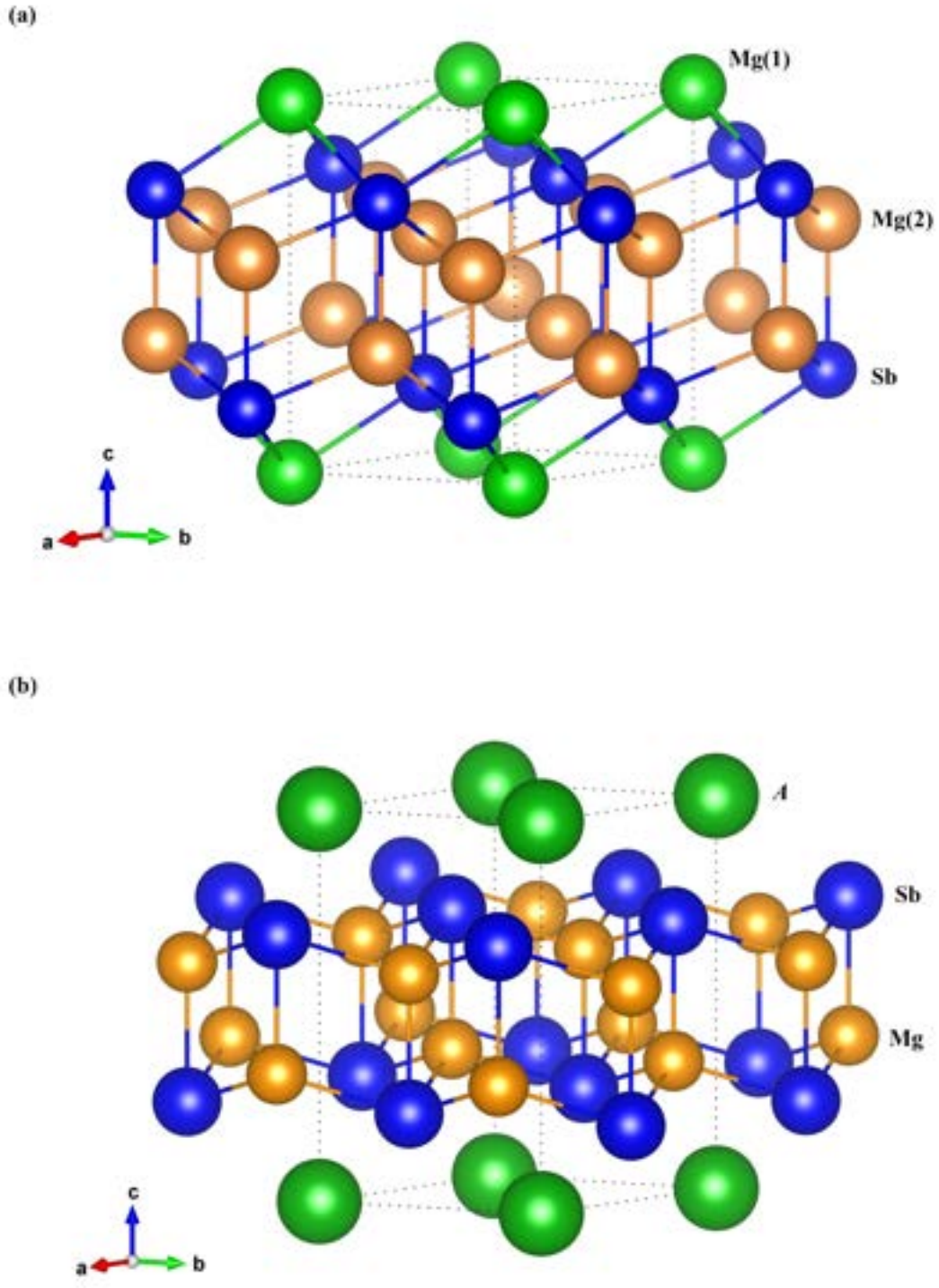

FIGURE 2.8: Comparison of the crystal structures of (a) Mg_3Sb_2 and (b) AMg_2Sb_2. Image created using VESTA [33].

More recently, $BaMg_2Bi_2$ was proposed to be a topological 3D DSM [57], followed by experimental confirmation, through the combined results of angle-resolved photoemission spectroscopy (ARPES) and first-principles calculations of band structure [58]. In the same study $SrMg_2Bi_2$ was found to be an ordinary insulator with a bulk band gap. Signs of surface superconductivity have also been reported for $BaMg_2Bi_2$ via resistivity measurements, with T_c in the range of 4.77 - 5.17 K and no transition observed in the specific heat data [59].

2.4.3 $A_4T_7Pn_6$

The family of ternary intermetallic compounds with a stoichiometry of 4:7:6 dates back to 1978, where the crystal structure of its first member, $U_4Re_7Si_6$, was reported by Akselrud et al. [60]. It crystallizes in a cubic structure (space group $Im\bar{3}m$, no. 229) with the number of formula units per unit cell $Z = 2$ and a lattice parameter $a = 8.224$ Å. It can be derived from a Cu_3Au-type structure (s.g. $Pm\bar{3}m$, no. 221), with U atoms located on the gold sites, Cu-sites partially occupied by all of the Si atoms and some Re atoms, with the remaining Re located on the interstitial octahedral sites according to the formula $U_4(Re_6Si_6)Re$ [61]. Full occupation of these sites would lead to a $CaTiO_3$-type (perovskite) structure, where they would be filled by Ti atoms (with Ca at Au sites and O at Cu sites). This way, the $U_4Re_7Si_6$ crystal structure can be considered an intermediate between the described structures, where only one in four octahedral sites is occupied. The comparison of the three structures is presented in Figure 2.9, where the atoms on the octahedral sites are marked in green (Re(2) in Figure 2.9(d) and Ti in Figure 2.9(f)). This partial insertion of interstitial Re causes a slight distortion, as it shifts the Si atoms towards the unoccupied octahedral sites, as seen in Figure 2.9(d), which shows the view of the $U_4Re_7Si_6$ structure along the c axis.

Over the next two decades, more silicides and germanides have been discovered, constituting a majority of the more than 70 compounds reported to date. The structure withstands various substitutions, even with differing valence electron numbers and sizes of the comprising atoms. Uranium can be replaced by magnesium, rare-earth metals or group 4 transition metals - titanium, zirconium and hafnium (elements that are formally divalent, trivalent and tetravalent, respectively) [62]. On the Re-site, other transition metals such as Tc, Co, Rh, Ir, Ru, and Os can commonly be found. The VEC can

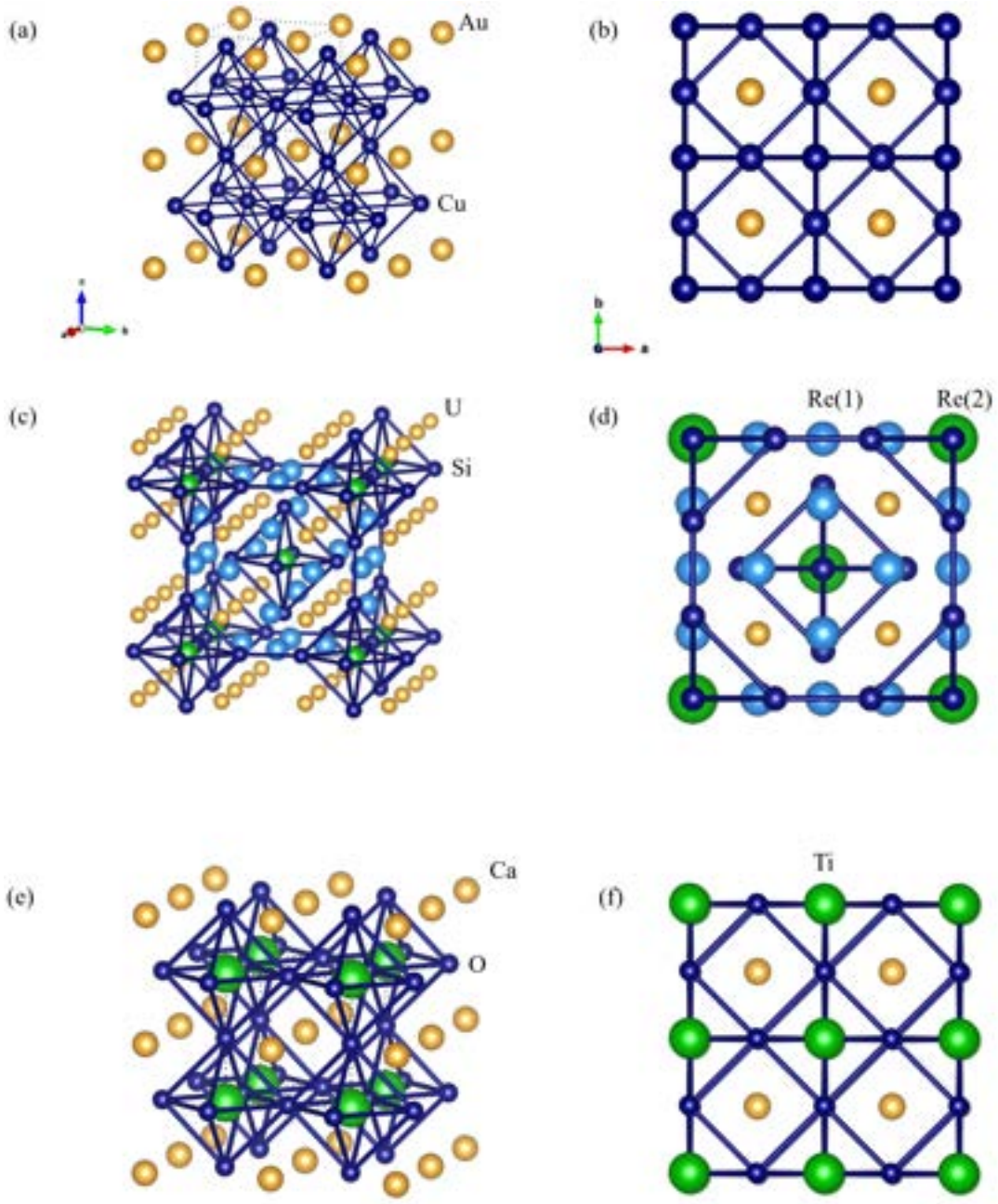

FIGURE 2.9: Comparison of (a,b) Cu_3Au, (c,d) $U_4Re_7Si_6$ and (e,f) $CaTiO_3$ crystal structures. Atoms occupying the interstitial octahedral sites are marked in green (Re(2) atoms in $U_4Re_7Si_6$ and Ti atoms in $CaTiO_3$). Image created using VESTA [33].

range from 85 (5/atom) for $U_4Tc_7Ge_6$ [63] to 105 (6.18/atom) for $Lu_4Rh_7Sb_6$ [64]. According to a hypothesis formulated by Engel et al. [61] the occurrence of the $U_4Re_7Si_6$ structure type can be roughly predicted based on the relative size of the A and T atoms, r_A/r_T, where the investigated compounds have a ratio of 1.28 or less and larger values are observed for $BaAl_4$-derived structures.

The first record of a 4:7:6 pnictide came from Noel et al. in 2000 [65]. Based on single-crystal X-ray diffraction data, the compound $U_4Ru_7As_6$ was found to be isostructural with $U_4Re_7Si_6$, with a lattice parameter of a = 8.3048 Å. More pnictides were reported only a year later by Wurth et al., for the first time containing magnesium on the A-site. The list of new compounds included three more arsenides: $Mg_4Rh_7As_6$, $Mg_4Ir_7As_6$ and $Yb_4Rh_7As_6$, as well as one phosphide $Mg_4Rh_7P_6$ (which, incidentally, to this day remains the only P-bearing compound in this family) [66]. The lattice parameters of the reported compounds are presented in Table 2.2.

TABLE 2.2: Lattice parameters of the 4:7:6 pnictides reported by Wurth et al. [66]

	$Mg_4Rh_7As_6$	$Mg_4Ir_7As_6$	$Mg_4Rh_7P_6$	$Yb_4Rh_7As_6$
Lattice constant [Å]	8.066	8.082	7.841	8.254

The crystal structure of the first antimonide, $Yb_4Rh_7Sb_6$, was reported by Leithe-Jasper et al. [67] in 2006, followed by the first attempt at characterizing the physical properties of any pnictide 4:7:6 family member by Schellenberg et al. [68]. The magnetization measurements give a reduced magnetic moment value of 3.16(1) μ_B/Yb (compared to the expected value of 4.54 μ_B/Yb for Yb^{3+}), suggesting an intermidiate-valence character of the compound. This was later followed by a series of antimonides $RE_4T_7Sb_6$, where RE = Gd – Lu and T = Ru or Rh [64], which included magnetic measurements of the Ru-bearing members. The compounds containing Dy, Ho, Er or Tm were found to exhibit Curie-Weiss paramagnetism, ordering antiferromagnetically below 10 K, 5.1 K and 4 K, for $Dy_4Ru_7Sb_6$, $Ho_4Ru_7Sb_6$ and $Er_4Ru_7Sb_6$, respectively. No ordering was observed for $Tm_4Ru_7Sb_6$. Based on the reduced value of magnetic moment of 3.71 μ_B/Yb, $Yb_4Ru_7Sb_6$ was found to be an intermediate-valent compound, similarly to its Rh-analogue.

The final arsenide, $Yb_4Ru_7As_6$, was recently reported by Hirose et al. as the first compound in the Yb-Ru-As system [69], bringing the total number of 4:7:6 pnictides to 22 (16 antimonides, 5 arsenides and 1 phosphide). $Yb_4Ru_7As_6$ orders antiferromagnetically below T_N = 2.5 K, with the effective magnetic moment (μ_{eff} = 4.28-4.45 μ_B/Yb) close to that expected for Yb^{3+}. Additionally, based on the value of the electronic specific heat coefficient (γ = 120 mJ/Yb-mol K^2) obtained from specific heat measurements, it was found

to be a moderately heavy-fermion compound.

Reviewing the literature clearly shows that most of the reported 4:7:6 compounds contain rare earth metals or, slightly less commonly, actinides. The three aforementioned magnesium-bearing compounds are, so far, the only exceptions. In addition to that, as no physical properties of these compounds were examined, the 4:7:6 intermetallics containing alkaline earth metals remain open to further investigations.

Chapter 3

Methodology

3.1 Sample preparation

Samples of investigated compounds were obtained mainly via two methods: solid-state reaction for polycrystalline samples and flux growth for single crystals.

Solid-state reaction method is the most common technique for synthesizing inorganic solids. They involve heating the mixture of solid reactants at elevated temperatures for a given time. However simple it may sound, choosing the right reaction parameters might not be that easy, as there are many factors that need to be considered, including the choice of the reactants (pure elements vs. pre-reacted precursors), the ratio in which they will be used (stoichiometric or off-, in order to account for possible loss of easily evaporating elements), selection of the crucible material, temperature and duration of the heating, quenching method, and the atmosphere of the reaction. The reactions are usually carried out in sealed tubes, which are either fully evacuated or back-filled with argon, providing protective atmosphere and preventing oxidation at elevated temperatures. The most commonly used tubes are quartz ones, which limit the maximum temperature of the reaction to 1200 °C. Higher temperatures can be reached when using, for example, sapphire tubes.

Several attempts to obtain polycrystalline samples employed an arc-melting technique, using an Edmund Bühler MAM-1 arc furnace. Once melted, the buttons are turned over and re-melted to ensure homogeneity; when needed, additional heat-treatment can be used.

For single crystal growth, the most frequently applied method is growth with application of molten flux. There are several advantages to this method.

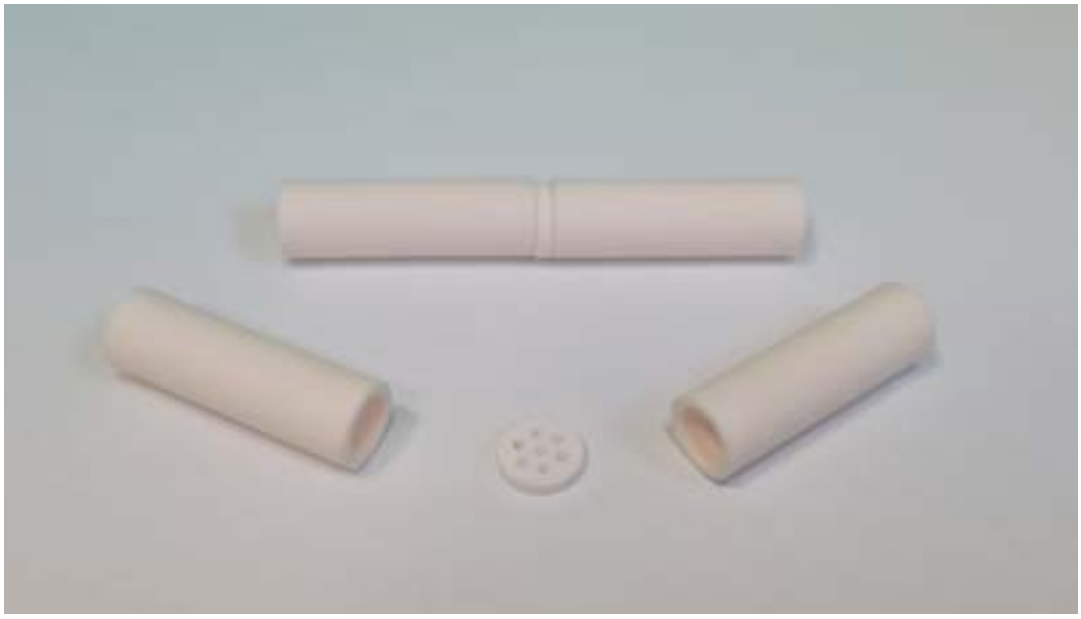

FIGURE 3.1: A set of crucibles and a filter used for flux growth of single crystals.

The main one is that it allows for a lowered temperature of the reaction, compared to synthesis in a solid state. The molten flux, acting as a reaction medium, increases the reaction rate by increasing the diffusion and mobility of the reactants. Generally, pure elements or simple salts with low melting temperatures are selected as flux. It is also common to, when possible, use one of the constituents of the target compound as flux to avoid the introduction of additional elements/compounds and minimize the risk of inclusions in the crystals or growth of undesired side phases during the reaction. If the self-flux method is not possible, another choice can be selected by analyzing binary phase diagrams of constituent elements and the potential flux.

The growth is usually carried out using a set of crucibles, a growth crucible containing the reactants and a catch crucible, separated by a frit-disc, as seen in Figure 3.1. Alternatively, the catch crucible can be replaced by a wad of quartz wool. The material of the crucible has to be chosen on the basis of the constituent elements, so that it does not undergo any reaction with the melt. Some of the used materials include alumina (Al_2O_3), boron nitride (BN), zirconium oxide (ZrO_2), magnesium oxide (MgO) or graphite (C). Al_2O_3 crucibles are the most frequently used ones, as they can be used with most of the common flux elements and are relatively cheap, compared to some more sophisticated materials. However, they are still not suitable for all growths. If the starting mixture of elements contains a significant amount

of rare earth metals, a BN crucible may be required.

The growth can be conducted in a standard chamber furnace. In the most straightforward growths, after the temperature is raised high enough to achieve a liquid phase (T_{liq}), and enough time has passed to allow for proper homogenization of the melt, the temperature is slowly lowered to allow for crystal growth. Finally, after the crucible is cooled down to a chosen temperature (T_{cent}), the still-liquid flux is removed, usually by centrifugation. Depending on the growth, additional steps may be added to achieve satisfactory results. As an example, a beneficial effect of temperature fluctuations at the liquid stage was described in [70] for MnBi crystals, where the furnace door was repeatedly, briefly opened in order to agitate the melt, which resulted in significantly larger crystals. A schematic of a heating profile is presented in Figure 3.2, including an additional stage that attempts to recreate such fluctuations near T_{liq} by rapidly (180 °C/h) cycling between two temperatures T_{f1} and T_{f2}.

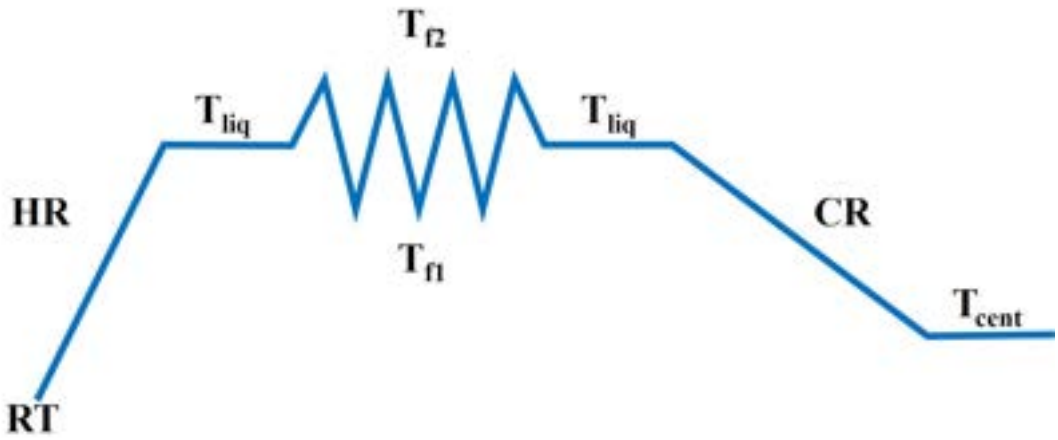

FIGURE 3.2: Schematic of a temperature profile used for flux growth of single crystals, where HR - heating rate, T_{liq} - temperature of the liquid phase, CR - cooling rate, T_{cent} - temperature of centrifugation and T_{f1} and T_{f2} - range of fluctuations introduced at high temperature

The obtained crystals can often be coated with a left-over layer of flux, which can be removed by chemical etching or by mechanical means. Alternatively, depending on the chosen flux, the centrifuging step can be forgone in favor of chemically etching all of the flux. This method can be particularly helpful in case of very small crystals that would not be caught by the frit disc.

Regardless of the employed technique, all easily oxidizing or toxic elements were handled in an argon-filled glovebox. As an additional precaution in case of As-bearing compounds, the prepared ampoules were then sealed in a second, larger tube, as can be seen in Figure 3.3, and the synthesis was conducted in vented furnaces positioned under an exhaust system.

FIGURE 3.3: Photo of a double-sealed quartz tube, after heating. Dark marks can be seen on the contained crucible set.

Further details and specific conditions of the syntheses are described in appropriate chapters.

Information about the chemical elements used for synthesis is listed in Table 3.1.

TABLE 3.1: Information about the chemical elements used during synthesis.

Chemical element	Purity (%)	Source
Mg	99.9	Onyxmet
Ca	99.9	Onyxmet
Sr	99.9	Onyxmet
Ba	99.9	Onyxmet
Rh	99.95	Mennica-Metale
Ir	99.95	Mennica-Metale
Pd	99.95	Mennica-Metale
Pt	99.95	Mennica-Metale
Cu	99.9	Onyxmet
Ag	99.9	Mennica-Metale
As	99.9	Onyxmet
Sb	99.9	Onyxmet
Bi	99.99	Onyxmet
Pb	99.9	Onyxmet
RE (Eu, Yb)	99.9	Onyxmet

3.2 Measurement techniques

3.2.1 Crystal structure and composition

The crystal structure and the phase purity of the samples were examined by powder x-ray diffraction (pXRD), using a Bruker D2 Phaser 2nd generation diffractometer with Cu-Kα radiation (λ = 1.5404 Å) and LYNXEYE XE-T detector. The experimental data was analysed by means of LeBail (using Bruker Topas software) or Rietveld method (using GSAS-II) [71].

Energy dispersive X-ray (EDX) spectroscopy was used as a non-destructive, supplementary investigation method for single crystals, to estimate the chemical composition Data were collected using FEI Quanta 250 FEG Scanning Electron Microscope (SEM) and analysed in TEAM EDS software.

3.2.2 Measurements of physical properties

All of the physical properties of the samples were investigated using the Evercool II Quantum Design Physical Property Measurement System (PPMS), which allows for the measurements to be performed for the temperatures down to 1.9 K and under applied magnetic field up to 9 T.

Electronic transport measurements were carried out using a four-probe method, with electrical contacts made out of platinum wires with a 50 μm diameter attached to the flat, polished surface of the sample with a silver epoxy paste (Epo-Tek H20E).

Heat capacity at constant pressure was measured using a dual slope, relaxation method, in which the temperature response of the sample is recorded during a heating period followed by a cooling period of the same length. For the measurement to be accurate, one side of the sample needs to be polished and placed on the sample platform using grease (Apiezon N) to ensure proper thermal contact with the platform.

Magnetization measurements were performed via vibrating sample magnetometer (VSM), in which the voltage created by oscillating the sample near a detection coil is measured. The samples can be measured both in a powdered form and as a solid piece, but the shape of the sample needs to be considered during analysis as it affects the measurement results.

Selected compounds were tested for superconductivity down to 400 mK using Quantum Design MPMS 3 SQUID magnetometer with Helium-3 refrigerator, courtesy of Prof. Tyrel M. McQueen from the Institute for Quantum Matter, Johns Hopkins University in Baltimore, MD (USA).

Chapter 4

ATPn compounds

The work on the 111 compounds started with developing an improved synthesis protocol for compounds that were already reported previously, in order to obtain higher-quality samples that could be used for thorough characterization of physical properties, including their non-trivial topological character through ARPES measurements. The crystal growth method and physical properties of selected compounds were presented as an oral presentation during the Polish Conference on Crystal Growth 2022 (Konferencja Polskiego Towarzystwa Wzrostu Kryształów 2022) and as a poster during 48^{th} Congress of Polish Physicists (48. Zjazd Fizyków Polskich).

The obtained single crystals were a subject of investigation in the TOTEM (engineering TOpological quantum phases in hexagonal TErnary coMpounds) project (PRIN 2022 - PE3, Consiglio Nazionale delle Ricerche, SPIN), lead by dr. Federico Bisti (University of L'Aquila) and dr. Paola Gentile (CNR-SPIN). A manuscript containing the results of measurements conducted on BaAgAs and SrAgBi is under preparation.

4.1 Crystal growth and crystal structure

The first series of synthesis attempts was focused on six silver-bearing compounds containing alkaline earth metals: CaAgBi, CaAgAs, BaAgBi, BaAgAs, SrAgBi and SrAgAs. The growths were later extended to crystals containing rare earth metals and/or copper. All of the crystal growth experiments were conducted in standard sets of the alumina Canfield crucibles, which were sealed in evacuated, and argon back-filled quartz tubes. For bismuth-bearing compounds, self-flux method was always the preferred route. Similarly, for the synthesis of the arsenides, bismuth was also the first choice of the flux, as self-flux growth would not be possible in this case due to several factors, among which are avoiding working with excessive amounts of arsenic and the fact that arsenic undergoes sublimation if the pressure is below 28 atm.

4.1.1 CaAgBi

In the case of CaAgBi crystal growth, following the assertion given by Sasmal et al. [72] that "excess Ag was necessary to obtain single crystals", the first attempt was made using a 1:2:20 ratio of the elements (Ca:Ag:Bi). A prepared sealed ampule was placed in a chamber furnace heated to 1050 °C and kept there for 8 h to allow for proper homogenization of the melt. Halfway through, several temperature fluctuations were introduced between 950 °C (T_{f1}) and 1060 °C (T_{f2}). After that, the furnace was slowly cooled to 420 °C, where the ampule was taken out and placed in a centrifuge in order to separate CaAgBi crystals from the molten flux. The growth resulted in small crystals, in the shape of slightly distorted hexagons and dimensions of 1 - 2 mm – significantly smaller than in the referenced report [72]. As this size was not satisfactory, further attempts were made, modifying the ratio of the elements by lowering the amount of bismuth flux for all the samples and changing the excess amount of silver that was used in each of them (all the other synthesis parameters remained unchanged). The experiments showed that changing the latter parameter strongly influences the size and shape of the obtained crystals. However, this relation is not as simple as more silver directly translating into better growth. This can be seen in Figure 4.1, where examples of the obtained crystals are presented in order of increasing silver content and it is clear that one of the middle compositions actually results in the smallest crystals of the four.

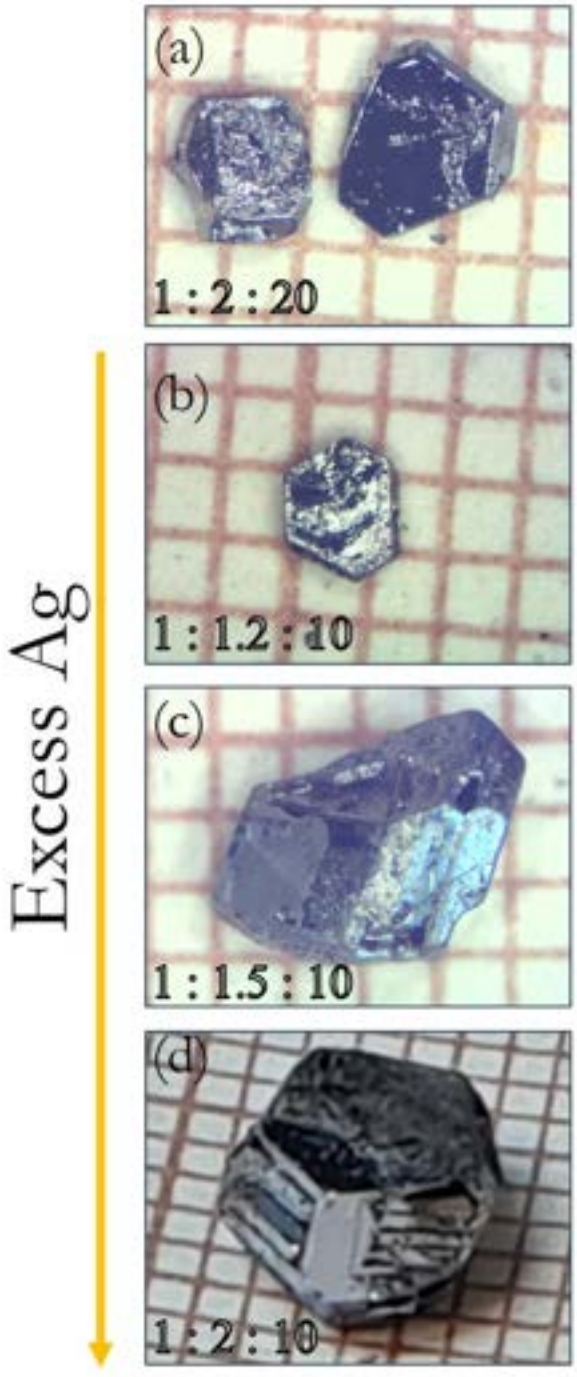

FIGURE 4.1: Comparison of CaAgBi single crystals obtained from compositions with varying excess of silver and flux amount.

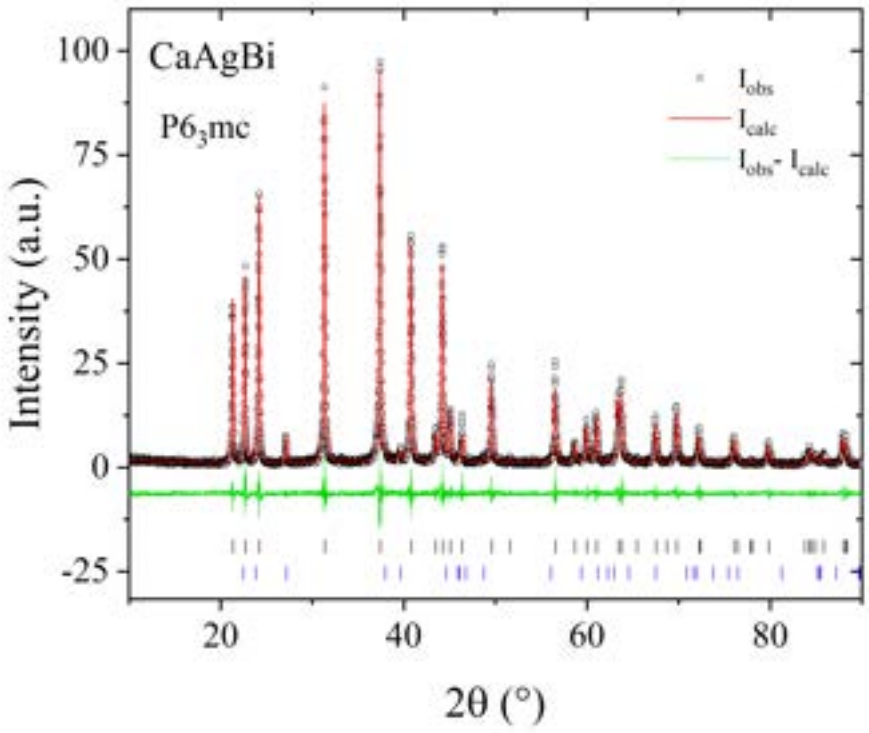

FIGURE 4.2: pXRD pattern of CaAgBi obtained from the starting ratio of 1:2:10 (black points), with a LeBail fit (red line) and vertical bars marking the expected positions of the Bragg reflections of the target compound (upper row, black), and of bismuth (lower row, blue). The difference between the observed and calculated intensities is shown below in green.

The last tested composition, corresponding to the 1:2:10 ratio, was decided to be the most promising one and was then used as a starting point for the synthesis of several other compounds. The pXRD diffraction pattern of the sample with the starting ratio of 1:2:10 is presented in Figure 4.2, together with the results of the LeBail analysis. The crystal structure was confirmed to be the hexagonal P63mc structure (s.g. no. 186). Additional presence of metallic bismuth was detected, connected to the flux left over at the surface of the crystal. The positions of the expected reflections of the P63mc phase are marked by the upper line of ticks and those of bismuth by the bottom line. The lattice parameters were calculated to be a = 4.8019(5) Å and c = 7.8260(7) Å, which is consistent with the previously reported values of a = 4.8113(4) Å and c = 7.8273(9) Å [73].

4.1.2 CaAgAs

The first composition that was tried was a slightly modified version of the one suggested by Xu et al. [37], with the only change being a slight increase of the amount of silver, resulting in the ratio of 1:1.2:1:9, instead of 1:1:1:9 (Ca:Ag:As:Bi). The heating profile was identical to the one used for CaAgBi. After centrifuging, a 5 mm x 4 mm x 3 mm cluster was obtained, which was easily separable into thin, elongated single crystals. The individual crystals had lengths up to 3 mm. Additional attempts were made to test the influence of silver levels for this compound, however, in this case larger excess of silver was detrimental to crystal growth. Increasing the relative amount of silver to 1.5 resulted in just one small single crystal being obtained, and further increase to 2 (as previously used in CaAgBi) resulted in no observable growth at all. The pXRD pattern is presented in Figure 4.3. The obtained lattice parameters are a = 7.2080(3) Å and c = 4.2703(4) Å.Besides the target phase and metallic bismuth, there is another unidentified impurity phase present in the sample, which can be seen from many unindexed reflections.

4.1.3 CaAgSb and CaCuSb

The initial attempt followed a slightly modified version of the procedure proposed for RE-doped compound $Ca_{1-x}RE_xAg_{1-y}Sb$ [74] using Pb flux, however, no crystal growth was observed. Both of the compounds were later obtained successfully, albeit unintentionally, while attempting to grow single crystals of $CaCu_4Sb_2$ and $CaAg_4Sb_2$. The ratio of elements used in the growths was equal to 1:4:6 in case of $CaAg_4Sb_2$ and 10:34:63 for $CaCu_4Sb_2$, corresponding to the eutectic points on the Ag-Sb and Cu-Sb phase diagrams. The sealed ampules were heated to 850 °C, held there for 12 h and cooled to 670 °C at a rate of 4 °C/h, at which point they were centrifuged. The collected pXRD patterns are presented in Figure 4.4. CaAgSb crystallizes in an orthorhombic crystal structure, with lattice parameters a = 7.7105(3) Å, b = 4.5979(2) Å and c = 8.3795(4) Å, while CaCuSb adopts a hexagonal structure with a = 4.4516(2) Å and c = 8.1326(4) Å.

4.1.4 BaAgAs

According to Xu et al. [37], using a nominal composition of 1:1:1 of Ba:Ag:As resulted in the growth of $BaAg_{1.837}As_2$, in the form of plate-like crystals crystallizing in a variant of the tetragonal $ThCr_2Si_2$-type structure, with only

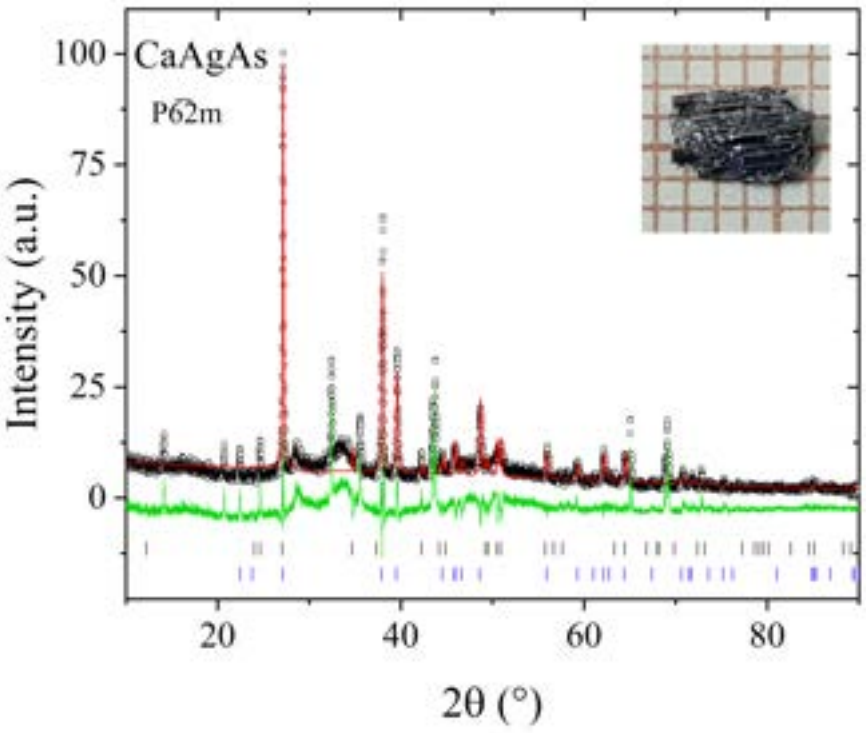

FIGURE 4.3: pXRD pattern of CaAgAs, with a LeBail fit (red line) and vertical bars marking the expected positions of the Bragg reflections of the target compound (upper row, black), and of bismuth (lower row, blue). The difference between the observed and calculated intensities is shown below in green.

very small needle-like crystals of BaAgAs found among them. For successful growth of BaAgAs, an excess of Ba was used and the amount of bismuth flux was significantly increased, resulting in a 2.5:1:1:20 (Ba:Ag:As:Bi) ratio. The report also indicates that a far slower cooling rate of 1 K/h was necessary. Even though those changes were found to result in a successful synthesis, they are less than optimal for crystal growth. The increased amount of bismuth flux is inherently connected to lowering the amount of the other constituents, as we are restricted by the total volume of the crucible used in the experiment – this limits the maximum size of the crystal that could be obtained. The significantly slowed down cooling rate also extends the experiment to close to a month (more than doubling the time needed for the typical crystal growth experiment), which is especially impractical in the investigation stage, where the best route is still being established. For that reason, several experiments were conducted to see whether both of these changes had to be made at the same time, or whether one of them had a much stronger influence on the crystal growth and would be sufficient on its own. In the first

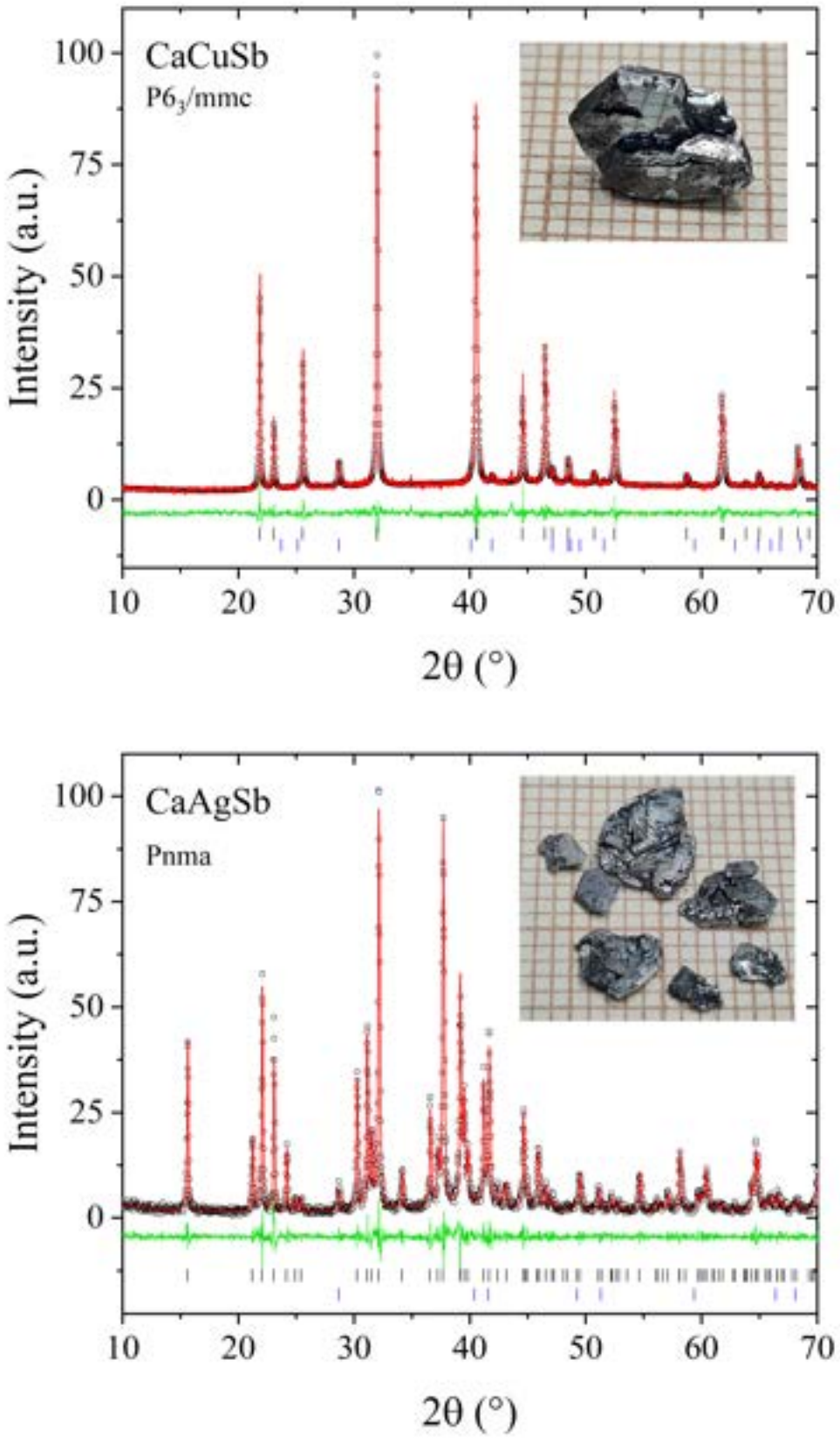

FIGURE 4.4: pXRD patterns of CaCuSb and CaAgSb, with a LeBail fit (red line) and vertical bars marking the expected positions of the Bragg reflections of the target compound (upper row, black), and of antimony (lower row, blue).

experiment the reported ratio of 2.5:1:1:20 (Ba:Ag:As:Bi) was used, however, the cooling rate was not changed and stayed at 3 K/h. This resulted in the growth of elongated crystals of BaAgAs, with lengths up to 3 mm. The obtained crystals are comparable in size to the ones presented in the referenced report. The pXRD pattern is presented in Figure 4.5(a). The compound crystallized in the hexagonal P63/mmc crystal structure with the obtained lattice parameters a = 4.607(4) Å and c = 8.915(6) Å, in agreement with the reported values of 4.613 Å and 8.896 Å [28]. Metallic bismuth is detected in the sample from the surface of the ground crystals. Anallysis of the EDX spectrum, seen in 4.5(b), collected from the crystal shows an element ratio of 34:30:34, and a negligible presence of bismuth. A similar slight Ag deficiency was also previously reported for SrAgBi crystals [47].

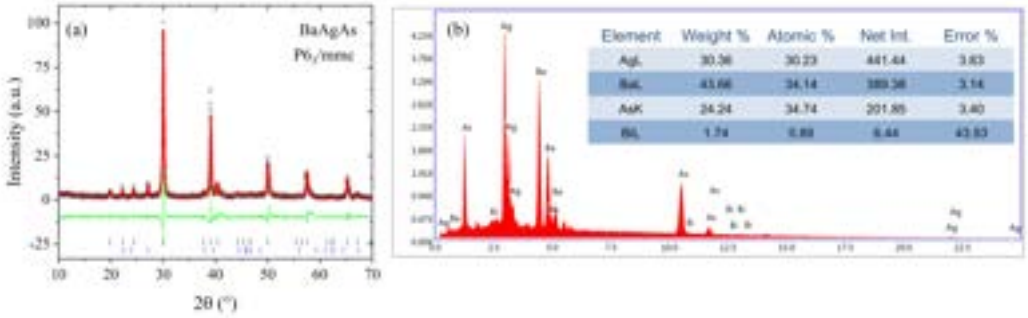

FIGURE 4.5: pXRD pattern of BaAgAs, with a LeBail fit (red line) and vertical bars marking the expected positions of the Bragg reflections of the target compound (upper row, black), and of bismuth (lower row, blue). The difference between the observed and calculated intensities is shown below in green. (b) EDX spectrum of the same crystal

The second attempt used the 1:1.2:1:9 ratio. This went against the recommendation of increasing the relative amount of barium compared to silver, nonetheless it was chosen, as it previously resulted in a successful growth of the CaAgAs crystals. The extracted product was composed of very thin, flat crystals, layered in a "scale-like" manner in the growth crucible. The individual layers were extremely fragile, and hard to separate while keeping them intact, both from each other and from the walls of the crucible. The crystals had an intense metallic luster. Their composition was investigated using EDX. The atomic percentage ratio of Ba:Ag:As is close to 26:33:41, corresponding to a composition of $BaAg_{1.25}As_{1.5}$, which places it somewhere in-between the target compound and the “plate-like” crystals obtained by Xu et al. [37] in their initial attempt. The obtained spectrum is presented in Figure 4.6, together with the SEM images, clearly showing the layered character

of the crystal. The bright white areas correspond to small bismuth droplets leftover on the surface of the crystals.

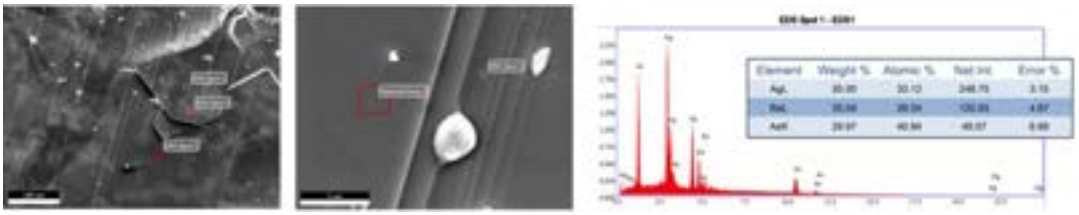

FIGURE 4.6: SEM images and EDX spectrum of the $BaAg_{1.25}As_{1.5}$ single crystal.

The final experiment again used the 1:1.2:1:9 ratio, but the cooling rate was lowered to the recommended 1 K/h. The result was a mixture of the two reaction products, composed mostly of the plate-like crystals similar to those obtained in the previous attempt with some smaller, elongated crystals of BaAgAs. The crystals obtained in these three attempts are compared in Figure 4.7. These results seem to indicate that applying both of these changes is not actually necessary. The targeted 111 crystals were obtained both when only the nominal ratio of elements was changed, and when the cooling rate was lowered without adjusting the ratio. In this case, changing the starting ratio of elements is a more preferable solution, as it keeps the time of the experiment relatively short and results in the 111 crystals being the only product of the reaction.

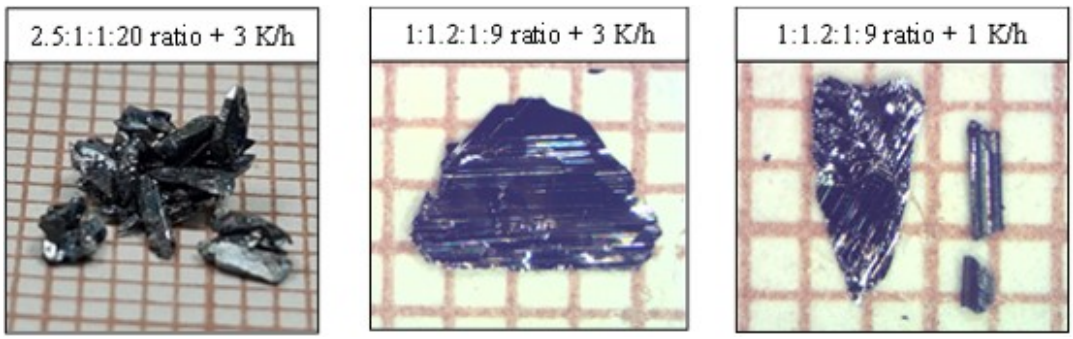

FIGURE 4.7: BaAgAs single crystals obtained from three different attempts varying the ratio of the elements (Ba:Ag:As:Bi) and the cooling rate of the crystal growth.

4.1.5 BaAgBi

As reported by Xu et al. [37] using bismuth self-flux results in plate-like $BaAg_{1.837}Bi_2$ crystals, which can be avoided by using lead as flux instead. The first attempt used the elements Ba:Ag:Bi:Pb in the 1:1:1:15 ratio. This resulted

in a multitude of small crystals, the size of roughly 1 mm x 1 mm x 1 mm. All the crystals were thoroughly covered in a layer of lead which could not be removed during centrifuging. Removing it later also proved to be quite problematic. The standard method of chemical etching using a mixture of acetic acid and 30% solution of hydrogen peroxide did not work well, as the etchant promptly attacks the crystals as well. A mixed method of alternating a very brief chemical etching followed by carefully polishing the surface of the sample proved successful at removing all the lead, however, some of the actual sample was also lost in the process and due to the small starting size of the crystals, the final result was quite poor.

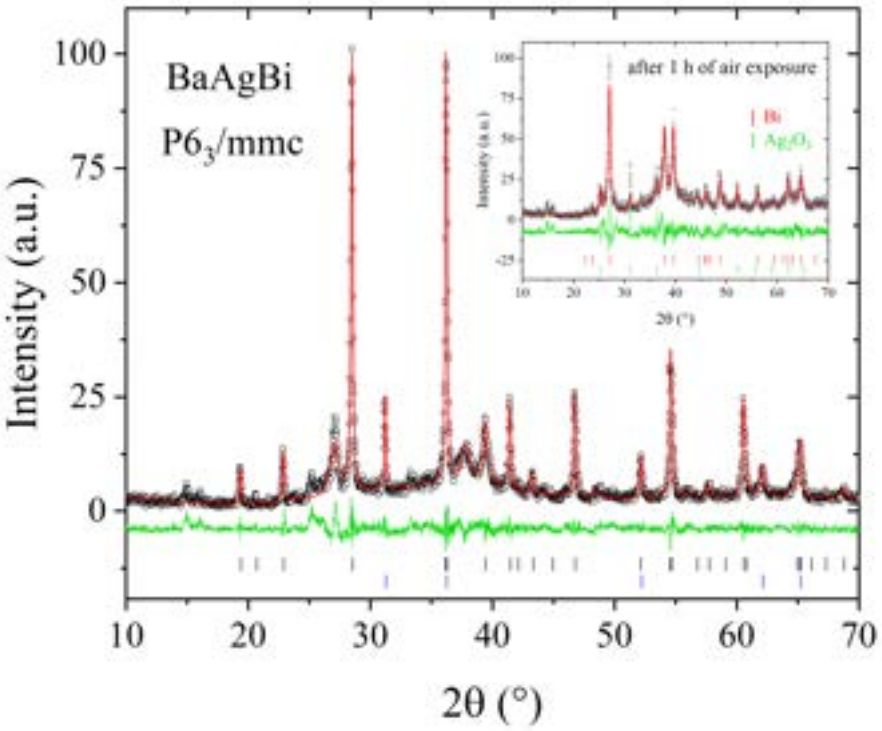

FIGURE 4.8: pXRD pattern of BaAgBi, with a LeBail fit (red line) and vertical bars marking the expected positions of the Bragg reflections of the target compound (upper row, black), and of lead (lower row, blue). The difference between the observed and calculated intensities is shown below in green. Inset: pXRD pattern collected on the same sample after it has been exposed to air for 1 hour. Marked Bragg reflections correspond to Bi (upper row, red) and Ag_2O_3 (lower row, green).

Figure 4.8 shows the pXRD pattern of a freshly-ground BaAgBi crystals

obtained from Pb flux. The compound is confirmed to crystallize in the expected hexagonal crystal structure (space group P63/mmc), with the calculated lattice parameters a = 4.949(3) Å and c = 9.132(5) Å, in agreement with the previously reported values of 4.953(1) Å and 9.146(3) Å [30]. Additional reflections coming from the Pb flux are indicated by the lower line of the vertical bars. Subsequent patterns collected from the same powdered sample showed that BaAgBi is highly air-sensitive. After an hour, the 111 phase is no longer detectable at all and, instead, metallic bismuth and silver oxide can be identified in the collected pattern (see inset of Figure 4.8).

The later attempts focused on finding a feasible synthesis route employing bismuth flux. Based on the previous experiments with BaAgAs crystals, which were plagued with the same problem of the 1:1.837:2 phase growth, a similar approach was tested. The relative ratio of Ba:Ag was again changed in order to make silver the limiting element of the reaction. BaAgBi crystals were successfully grown using the 2.5:1:1:20 ratio of the elements, however, the crystals were once again heavily coated with leftover flux. The comparison of the obtained crystals is presented in Figure 4.9.

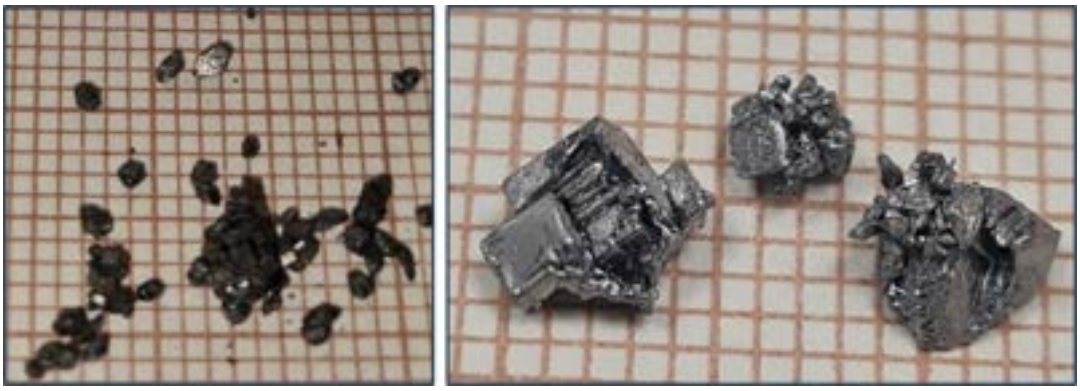

FIGURE 4.9: Comparison of BaAgBi crystals obtained from Pb flux (on the left) and from Bi flux (on the right).

4.1.6 SrAgAs

For the synthesis of SrAgAs crystals, the previously tested ratio of 1:1.2:1:9 (Sr:Ag:As:Bi) employing a slight excess of silver was used. The pXRD pattern is presented in Figure 4.10. The compound crystallizes in the hexagonal crystal structure P63/mmc with lattice parameters a = 4.5277(3) Å and c = 8.2941(9) Å, very close to the reported values of 4.529(1) and 8.921(2) Å [28]. The compound is stable in air.

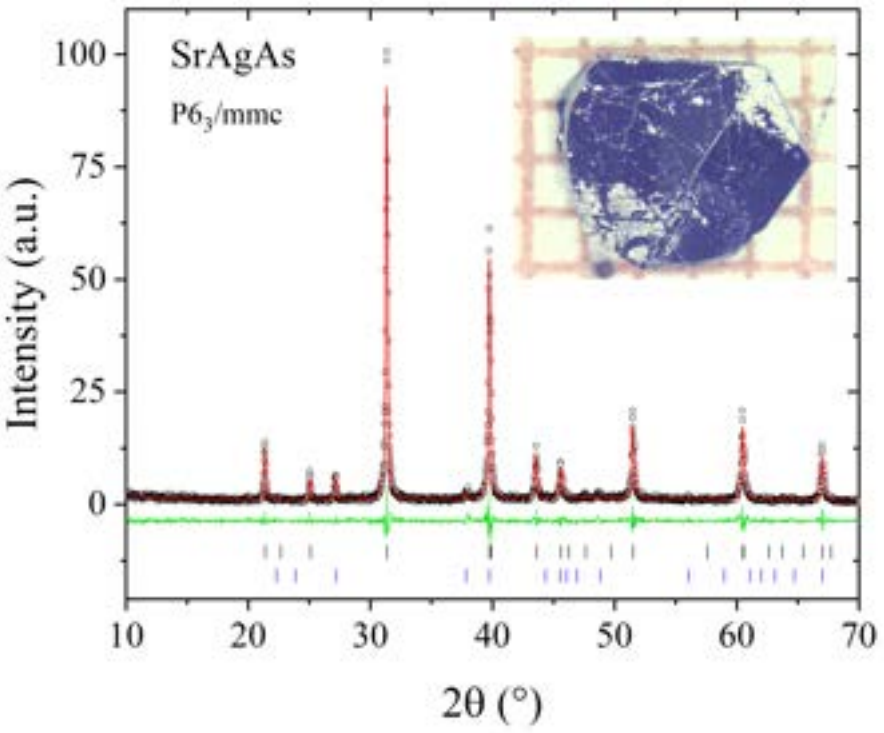

FIGURE 4.10: pXRD pattern of SrAgAs, with a LeBail fit (red line) and vertical bars marking the expected positions of the Bragg reflections of the target compound (upper row, black), and of metallic bismuth (lower row, blue). The difference between the observed and calculated intensities is shown below in green.

4.1.7 SrAgBi

For Sr-bearing crystals, as was the case for Ca-based compounds, the level of silver excess for the bismuthide had to be higher than for the arsenide analogue. The same ratio of 1:2:10 (Sr:Ag:Bi) was employed. The obtained crystals are presented in Figure 4.11 along with the pXRD pattern. As is the case for all the other Ag-bearing compounds, the crystal structure is hexagonal (P63/mmc) with lattice parameters a = 4.5275(3) Å and c = 8.2938(9) Å, which is significantly smaller than the values found in literature, where a = 4.876(1) and c = 8.480(2) Å [30]. The compound was found to be air-sensitive, but significantly more stable than BaAgBi.

4.1.8 YbCuBi and YbAgBi

Single crystals of two bismuthides, where the alkaline earth metal was replaced by ytterbium, were obtained from an element ratio of 1:2:10. The

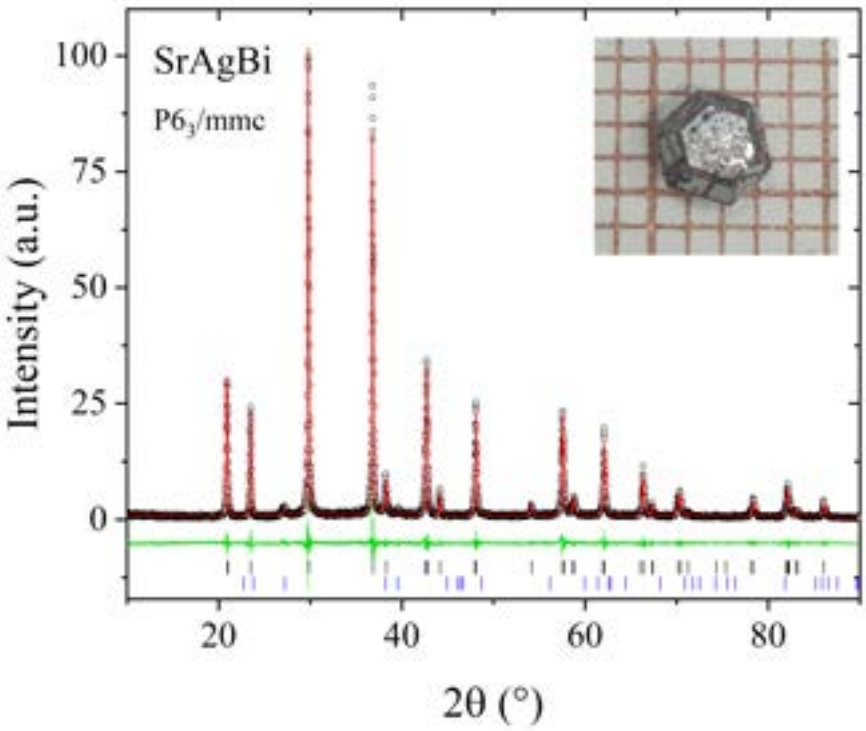

FIGURE 4.11: pXRD pattern of SrAgAs, with a LeBail fit (red line) and vertical bars marking the expected positions of the Bragg reflections of the target compound (upper row), and of metallic bismuth (lower row). The difference between the observed and calculated intensities is shown below in green.

pXRD patterns and the crystals are presented in Figure 4.12. The obtained lattice parameters are a = 4.5811(4) Å and c = 7.857(1) Å for YbCuBi and a = 4.8061(4) Å and c = 7.7762(9) Å for YbAgBi, consistent with the values reported in [30].

The corresponding arsenides, YbAgAs and YbCuAs, could not be obtained following this method.

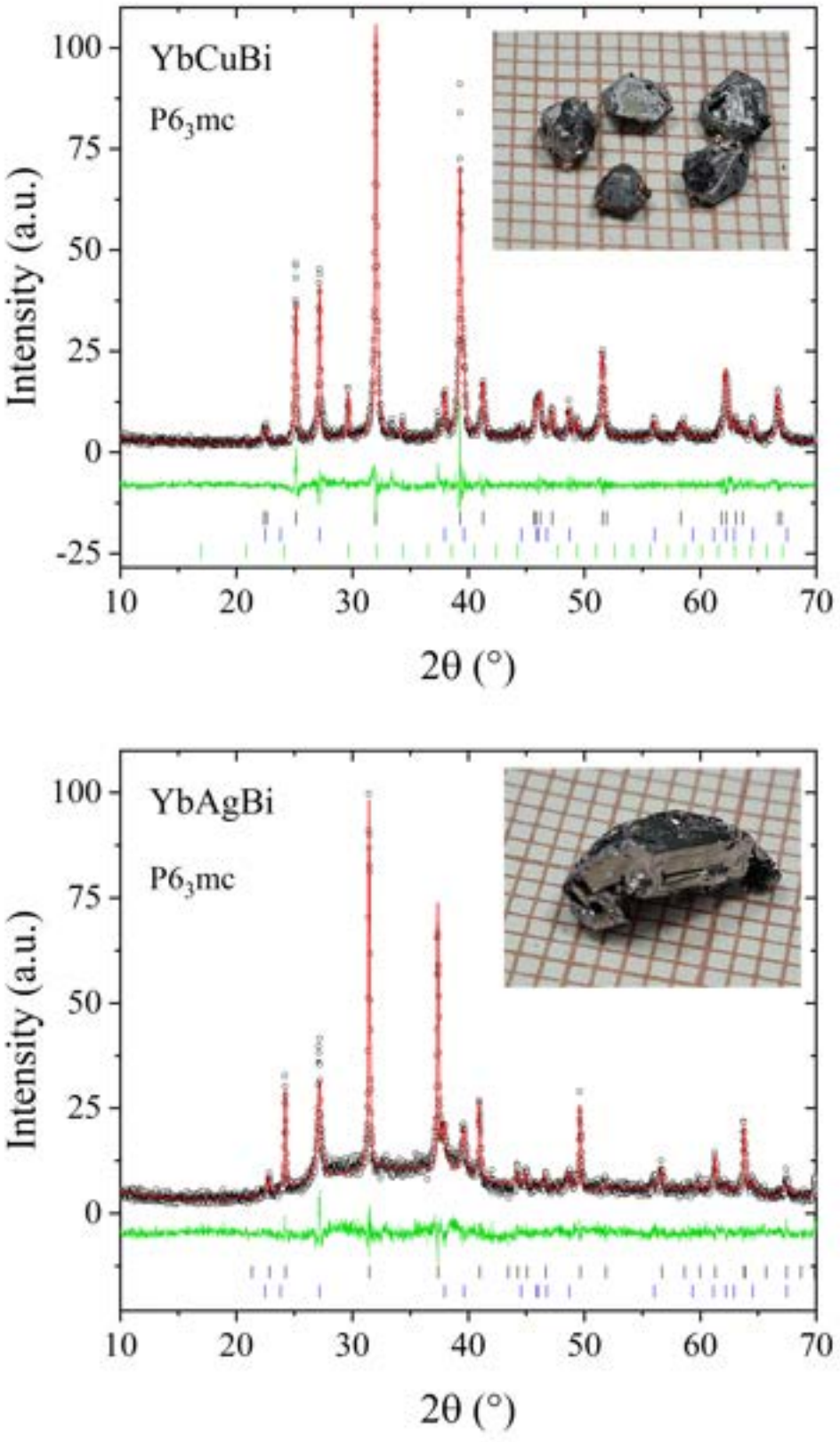

FIGURE 4.12: pXRD pattern of YbCuBi and YbAgBi with a LeBail fit (red line) and vertical bars marking the expected positions of the Bragg reflections of the target compound (black), bismuth (blue) and Yb_2O_3 (green, in the YbCuBi pattern).

4.1.9 Chemical doping attempts

Preliminary results of ARPES measurements performed at VUV Photoemission beamline at Elettra Sincrotrone (Trieste) on selected samples (SrAg*Pn* and BaAg*Pn*, where *Pn* - Bi, As) indicated that the Dirac point could not be directly detected due to the p-doped character of the samples. Several experiments focused on a partial substitution of the divalent A-element with a rare earth metal (La/Eu) in SrAgBi, SrAgAs, BaAgBi and BaAgAs were attempted, in order to shift the Fermi level. Various *A*:*RE* variations were tested, however, EDX analysis showed that none of the obtained crystals contained both of the elements.

Surprisingly, the addition of Eu to the starting elements strongly affected the growth of BaAgAs. Using a 0.75(Eu):2.5(Ba):1:1:20 Pb ratio resulted in a growth of just one, bulk crystal, which can be seen in Figure 4.13 (the original BaAgAs crystals can be seen in Figure 4.7). As the EDX data showed no presence of Eu in the crystal, this procedure seems to be a viable, improved route to obtain pure, bulk BaAgAs crystals.

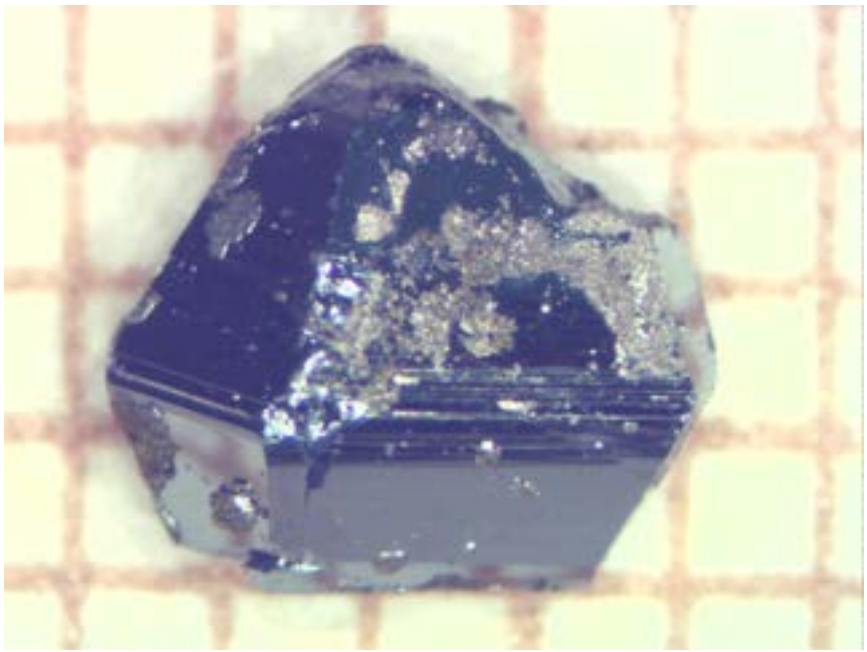

FIGURE 4.13: A single crystal of BaAgAs, obtained from a doping attempt from a 0.75:2.5:1:1:20 (Eu:Ba:Ag:As:Pb) element ratio.

4.2 Physical properties

Electrical resistivity of selected samples (CaAgBi, SrAgBi, YbCuBi and YbAgBi), was measured in the temperature range of 1.9 K – 300 K. As can be seen in Figure 4.14 all three samples exhibit typical metallic behavior, with resistivity values decreasing as the temperature is lowered. The RRR values, RRR = ρ(300 K)/ρ(1.9 K), were determined to be 3.2, 4.2, 4.7 and 3.1, for CaAgBi, SrAgBi, YbCuBi and YbAgBi, respectively. For single crystals, the values are relatively small, but comparable to the ones previously reported for other compounds in this family [38, 37, 75]. All three compounds have very close values of residual resistivity (19 - 22 $\mu\Omega$) and room temperature resistivity (67 - 77 $\mu\Omega$).

Contrary to the results presented by Xu et al. [37], no superconducting transition was found around 6.2 K for SrAgBi. In the referenced report, this superconducting transition is ascribed to a presence of some kind of a secondary phase, which could lead to a conclusion that the crystal obtained here is of better quality, as it does not contain this superconducting impurity phase. A drop in resistivity appears below 2.7 K, however, the full transition could not be observed as it was outside of the measuring range (below 1.9 K). This data somewhat matches the previous report on SrAgBi [38], where the onset of filamentary superconductivity appears between 2.85 and 3.3 K, for various crystals. The authors of [38] suggested that the superconductivity of the sample is extrinsic, due to a very low superconducting fraction (less than 1.5%) and no anomaly in the specific heat data. A superconducting $SrBi_3$ impurity is suggested as a possible source, even though its transition temperature is reported to be 5.6 K [76].

A similar transition can also be observed in YbAgBi data, where the drop can be seen near 2.85 K (the onset of the transition could appear at any point below 3.3 K, but cannot be estimated precisely due to too few data points). An alternative explanation for the observed transition in both of the examined compounds could be related to a meta-stable compound $AgBi_2$, proposed by Matthias et al. in their overview of superconducting bismuth compounds [77]. $AgBi_2$, forming at the inter-face of the two elements, was found to be superconducting with T_c = 2.78 - 3 K, exhibiting "full Meissner signal and heat capacity anomaly".

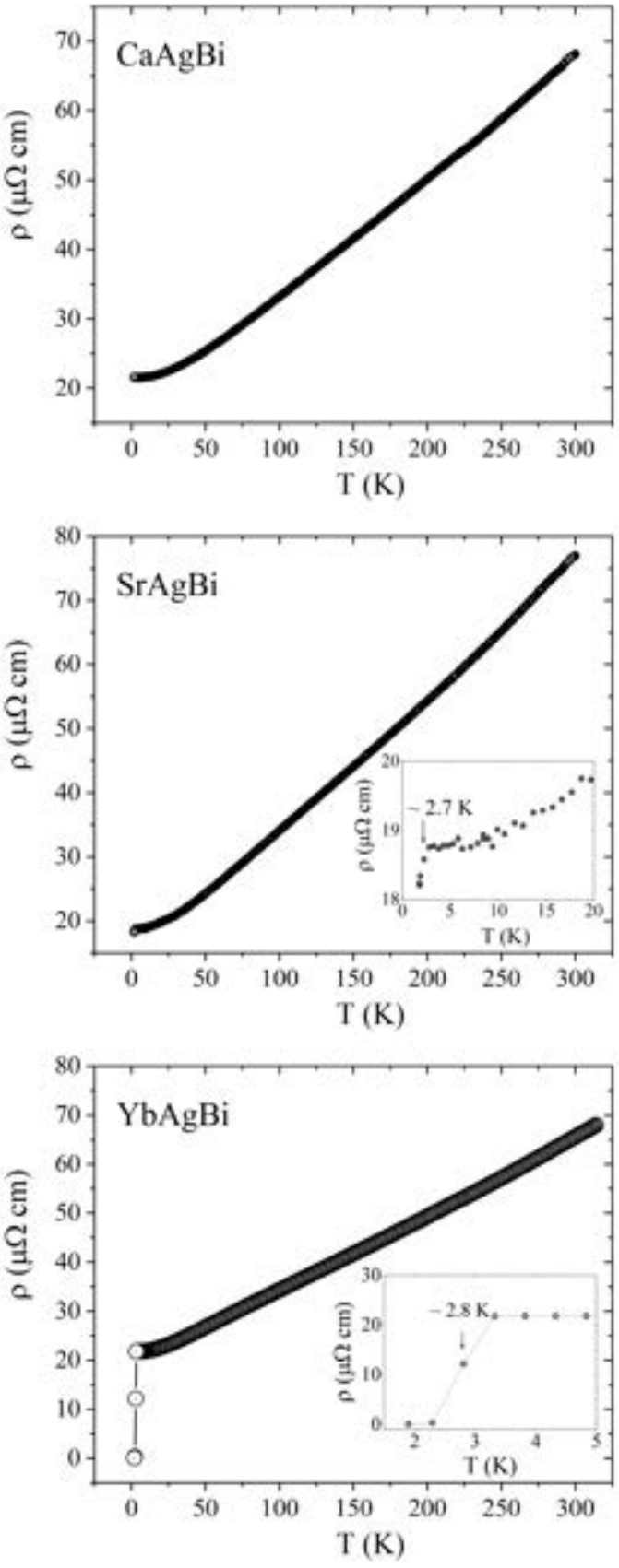

FIGURE 4.14: Electrical resistivity of single crystals of CaAgBi, SrAgBi, YbCuBi and YbAgBi.

Figure 4.15 shows the magnetoresistance (MR) data, collected at a constant temperature of 1.9 K, with the applied magnetic field in the range of 0 – 9 T. MR was calculated according to the formula:

$$MR = \frac{\rho(H) - \rho(0)}{\rho(0)} \times 100\% \tag{4.1}$$

where $\rho(0)$ and $\rho(H)$ are the resistivity in the absence and in the presence of the applied magnetic field. MR for all four compounds is positive. Both CaCuSb and CaAgSb show linear, non-saturating MR, which at 9 T reaches 20 % for CaCuSb, and double that for CaAgSb. YbAgBi data shows a sharp increase at low field (< 1 T), which is one of the signs of possible weak antilocallization (WAL) and was previously reported for several other ternary bismuthides, such as ScPtBi, SrAgBi and CaAgBi [38, 72, 78]. The highest MR is exhibited by YbCuBi, nearing 110 %.

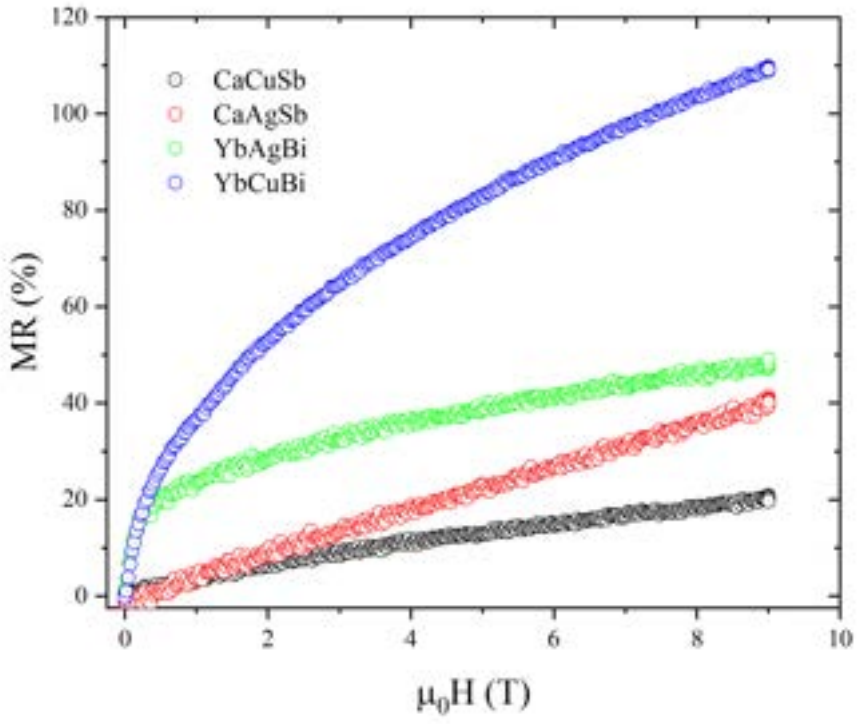

FIGURE 4.15: Magnetoresistance of selected 111 compounds measured at 1.9 K in the magnetic field range of 0-9 T.

For selected samples, the temperature-dependent heat capacity was measured in the range of 1.9 K – 260 K. The results are collected in Figure 4.16. The measurements were conducted under zero applied magnetic field. No

phase transitions are observed forr any of the samples. At higher temperatures, heat capacity of all of the bismuthides reaches the value of ~ 75 J mol^{-1} K^{-1} predicted by the Dulong-Petit limit:

$$C = 3nR \tag{4.2}$$

where R is the universal gas constant ($R = 8.314$ J mol^{-1} K^{-1}) and n is the number of atoms per formula unit (here, $n = 3$). For the two compounds containing As, the highest achieved values remain slightly below the predicted ones.

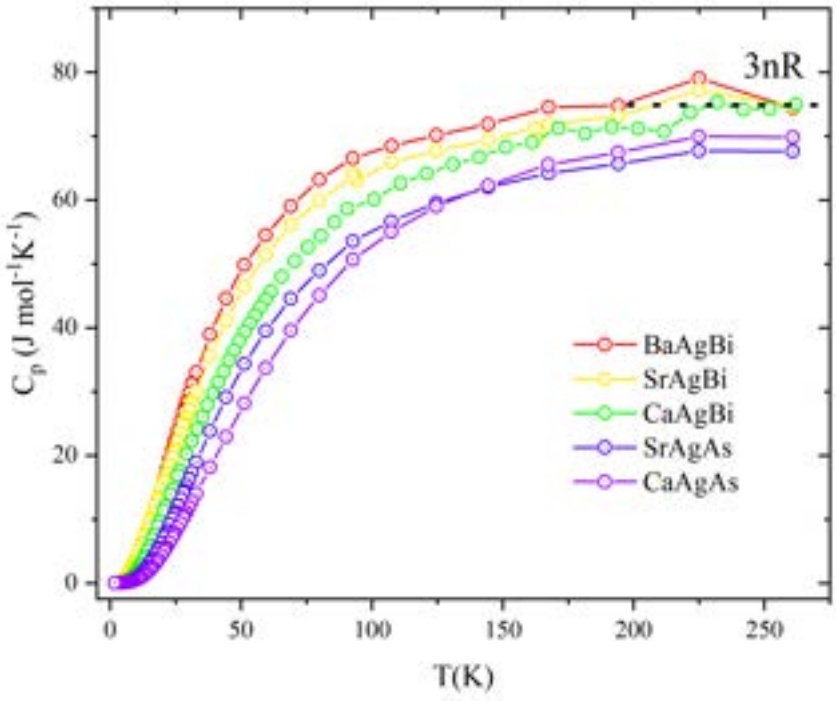

FIGURE 4.16: Temperature dependence of specific heat of selected 111 samples.

The low temperature region is presented in Figure 4.17. In non-magnetic materials, total heat capacity can usually be described by:

$$C_p = C_{el}(T) + C_{ph}(T) = \gamma T + \beta T^3 \tag{4.3}$$

which, alternatively, can be written as:

$$\frac{C_p}{T} = \gamma + \beta T^2 \tag{4.4}$$

where γ is the Sommerfeld coefficient. By presenting the data as C_p/T versus T^2, a linear dependence should be observed. It is clear that the samples, with the exception of CaAgBi, do not show the expected behavior and applying the two-term fitting function resulted in negative values of γ and/or β in all cases, including CaAgBi. A better fit was obtained by adding an additional lattice heat-capacity term, according to the formula:

$$\frac{C_p}{T} = \gamma + \beta T^2 + \delta T^4 \tag{4.5}$$

where the δ contribution is added to account for the deviation from the linear behaviour of the C_p/T curves. Initially, the fitting was performed with all of the parameters unrestrained. In the case of bismuthides, this resulted in error values that were quite high (for both the γ and β parameters), and γ values were equal to 0 within the obtained error values. Since the density of states $N(E_F)$ is directly proportional to the Sommerfeld coefficient, this indicates a lack of the electronic states at the Fermi level, in line with the predictions about the semi-metallic topological properties of these materials.

A final fit was performed with γ value fixed to 0. The values of the β parameter obtained during these two procedures, and the subsequently calculated Debye temperatures, are very close, however, the standard errors are decreased by one order of magnitude. The comparison of the obtained values is presented in Table 4.1. With the current set of data there seems to be no clear trend of the Debye temperature changing depending on the alkaline earth metal used in the compound.

TABLE 4.1: Comparison of the parameters obtained from the unrestrained fit and by fixing the value of γ = 0 for selected 111 compounds

	Unrestrained fit			Fit with fixed $\gamma = 0$	
	γ $\left(\text{mJ mol}^{-1}\text{ K}^{-2}\right)$	β $\left(\text{mJ mol}^{-1}\text{ K}^{-4}\right)$	θ_D (K)	β mJ $\text{mol}^{-1}\text{ K}^{-4}$)	θ_D (K)
CaAgBi	0.2(5)	0.9(2)	186(14)	0.92(5)	185(3)
SrAgBi	0(1)	0.5(3)	226(45)	0.55(4)	220(5)
BaAgBi	0.3(6)	1.1(1)	174(5)	1.12(4)	173(2)
CaAgAs	0.4(2)	0.18(5)	318(23)	0.27(2)	278(7)
SrAgAs	0.3(2)	0.38(5)	248(11)	0.55(6)	220(8)

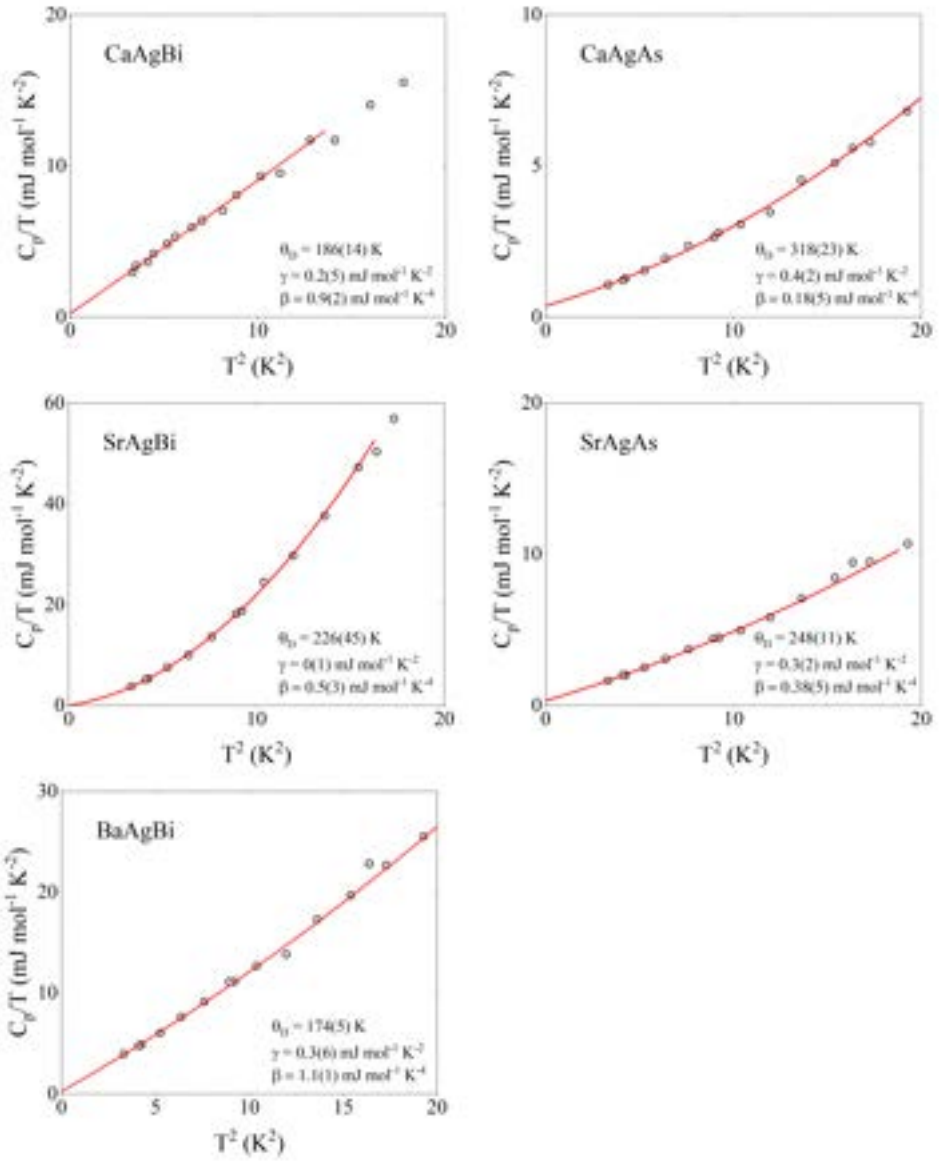

FIGURE 4.17: C_p/T versus T^2 heat capacity data of selected 111 compounds in the low-temperature region, where the red lines represent the fit to Equation 4.5.

For Yb-bearing compounds, YbAgBi and YbCuBi, temperature-dependent magnetization measurements were performed. The χ vs T data is presented in Figure 4.18. The maximum observed in YbCuBi, shown in the inset of the figure, can be ascribed to the presence of an antiferromagnetic impurity Yb_2O_3 with T_N = 2.3 K [79]. At the lowest temperatures χ values are one order of magnitude lower than previously reported for YbTBi compounds [80]. Data was fitted according to the modified Curie-Weiss law:

$$\chi = \frac{C}{T - \theta_{\mathrm{CW}}} + \chi_0 \tag{4.6}$$

where χ_0 is the temperature-independent contribution to susceptibility, C is the Curie constant and and θ_{CW} is the Curie-Weiss temperature. For both of the compounds χ_0 values are of the order of 10^{-5} emu mol^{-1}, however the value is negative for YbCuBi and positive for YbAgBi. Both of the θ_{CW} are negative (θ_{CW} = -4.23 K for YbCuBi and θ_{CW} = -1.34 K for YbAgBi). The obtained C values lead to effective magnetic moments that are an order of magnitude lower than expected for Yb^{3+} (4.54 μ_B), μ_{eff} = 0.177 μ_B for YbAgBi and μ_{eff} = 0.408 μ_B for YbCuBi. This indicates that Yb in the 111 compounds is in a non-magnetic 2+ state and the observed Curie tail is due to the presence of paramagnetic impurities. There is no sign of the superconducting transition in YbAgBi, further pointing towards an extrinsic character of the superconductivity observed in the resistivity measurement.

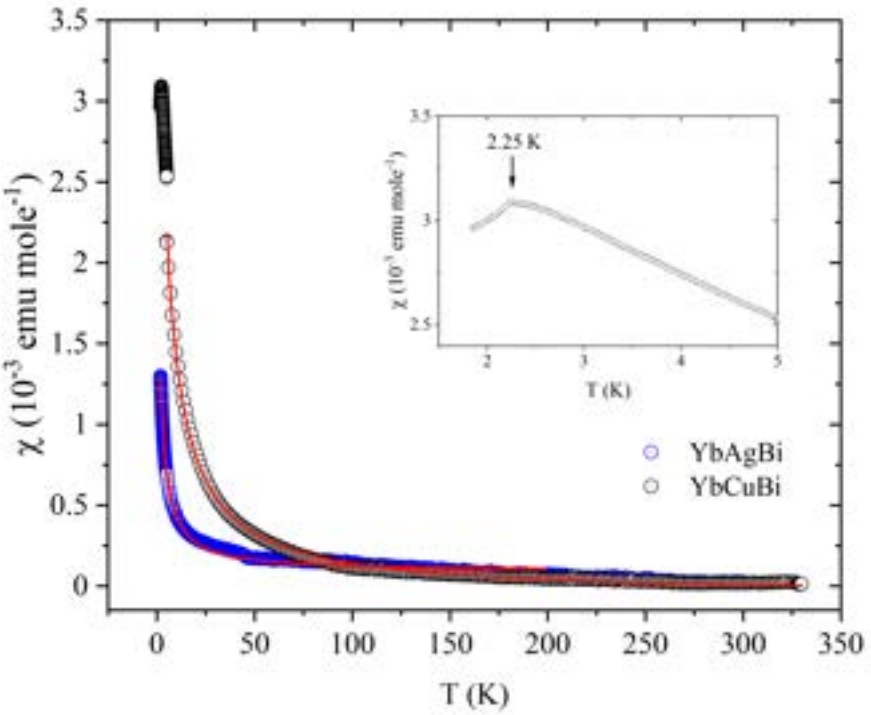

FIGURE 4.18: Temperature dependence of molar magnetic susceptibility of YbCuBi and YbAgBi. The red lines represent a fit to the modified Curie-Weiss law (Equation 4.6). Inset: close-up view of the low temperature region of YbCuBi data, where an antiferromagnetic transition ascribed to Yb_2O_3 can be seen.

Chapter 5

$A\mathrm{Mg_2}Pn_2$ compounds

Single crystals of four $A\mathrm{Mg_2}Pn_2$ compounds, where A = Ba, Sr and Pn = Bi, Sb were obtained through flux crystal growth. The compounds described in this section have been investigated in collaboration with dr Chiara Bigi (Synchrotron SOLEIL) and dr Federico Mazzola (CNR-SPIN), who performed the ARPES measurements. A publication containing results pertaining to $\mathrm{BaMg_2Bi_2}$ has been submitted to *Physical Review B*. The manuscript is attached as Appendix A.

5.1 Crystal growth

5.1.1 Bismuthides $A\mathrm{Mg_2Bi_2}$

According to [59] the single crystals of $\mathrm{BaMg_2Bi_2}$ could be obtained through self-flux growth by using constituent elements in a 1:5:9 ratio, while [58] uses a 1:4:6 ratio for both the Ba- and Sr-bearing bismuthides.

Initially, following [59], the 1:5:9 ratio was used for both $\mathrm{BaMg_2Bi_2}$ and $\mathrm{SrMg_2Bi_2}$. The alumina crucible containing the mixed elements was placed in an evacuated tube, heated to 900 °C, held there for 12 h and slowly cooled to 650 °C at a rate of 1 °C/h. The Sr-bearing compound could not be centrifuged at this temperature and the centrifuging had to be re-tried after raising the temperature to 700 °C in order to re-melt the flux, at which point it was successful. The obtained single crystals of $\mathrm{BaMg_2Bi_2}$ typically had a size of a few millimeters, had a smooth surface with an intense metallic luster, and clear signs of hexagonal habit. An example of a crystal is presented in Fig 5.1.

The $\mathrm{SrMg_2Bi_2}$ crystals obtained from the first growth were significantly smaller and more irregularly-shaped. Examples of crystals obtained from

FIGURE 5.1: Example of a $BaMg_2Bi_2$ single crystal.

several batches with varying elemental ratios are presented in Fig 5.2, with the largest, most well-formed crystals obtained as a result of a 1:5:15 ratio.

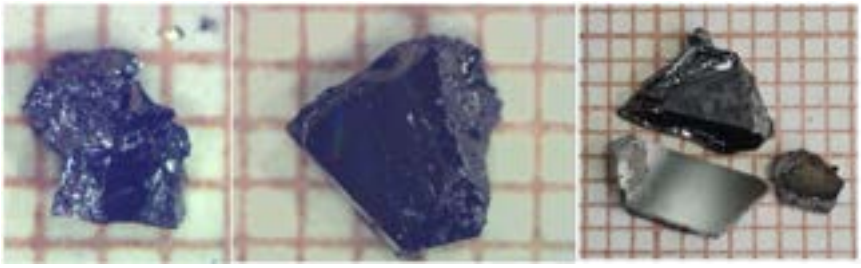

FIGURE 5.2: Comparison of $SrMg_2Bi_2$ single crystals, obtained from (from left to right) 1:5:9, 1.25:5:9 and 1:5:15 ratio of starting elements.

5.1.2 Antimonides AMg_2Sb_2

High quality, bulk crystals of $BaMg_2Sb_2$ and $SrMg_2Sb_2$ have not previously been reported. In the only experimental work related to these compound, the crystals are described as "thin, silvery, platelets", which needed to be extracted from a larger irregular chunk [54].

A self-flux growth using a 1:5:9 ratio, following the heating profile used for the bismuthides. Both of the growths resulted in a parallel growth of two reaction products. All crystals were of a 2-3 m x 2 m x 1 mm size. The crystals could not be distinguished visually, however, EDX analysis of individual crystals revealed them to be the targeted compound and Mg_3Sb_2. The surface of the obtained $BaMg_2Sb_2$ crystals was not particularly smooth; an SEM image showed that it was covered in thin, uneven layers with clear hexagonal forms. The obtained crystals can be seen in Fig 5.3(a) and Fig 5.3(b).

Further experiments focused on optimizing the growth, in order to eliminate the secondary Mg_3Sb_2 phase. Several growths containing a larger amount of Ba/Sr were performed, in a range of 1-1.6:5:9. In case of $BaMg_2Sb_2$ the outcomes were unchanged, while in the case of $SrMg_2Sb_2$, the 1.25:5:9 ratio resulted in an irregular, clumped growth. As can be seen in the optical microscopy image in Fig 5.4(a), individual, small crystals of the target compound could be distinguished in the mass, but could not be separated from it unscathed. Over the course of the experiments, it was found that the growth resulted in Sr/$BaMg_2Sb_2$ as the only product as long as the Mg:Sb ratio was equal to 1:3; both 1:3:9 and 1:5:15 growths yielded satisfactory results, which can be seen in Figure 5.3(c) and Fig 5.4(b), for $BaMg_2Sb_2$ and $SrMg_2Sb_2$ respectively. The additional uneven growths on the surface of $BaMg_2Sb_2$ have also been eliminated.

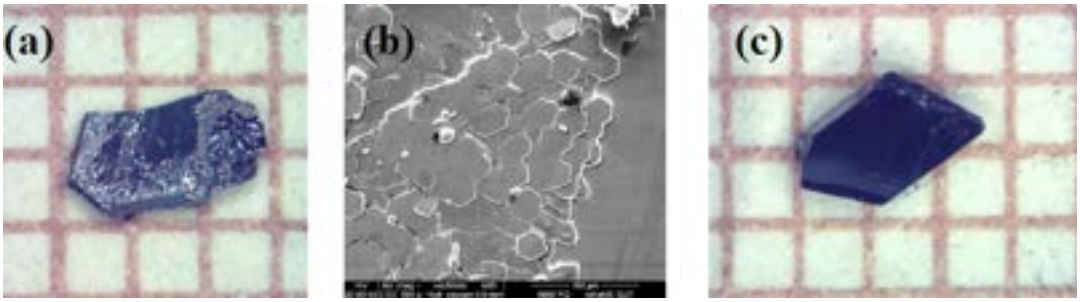

FIGURE 5.3: (a) Single crystal of $BaMg_2Sb_2$ obtained from a 1:5:9 ratio, (b) SEM image of the surface and (c) a single crystal obtained from an optimized growth using a 1:3:9 ratio.

Based on all of the performed growths it can be concluded that the amount of the alkaline metal has little influence over the outcome of the growth.

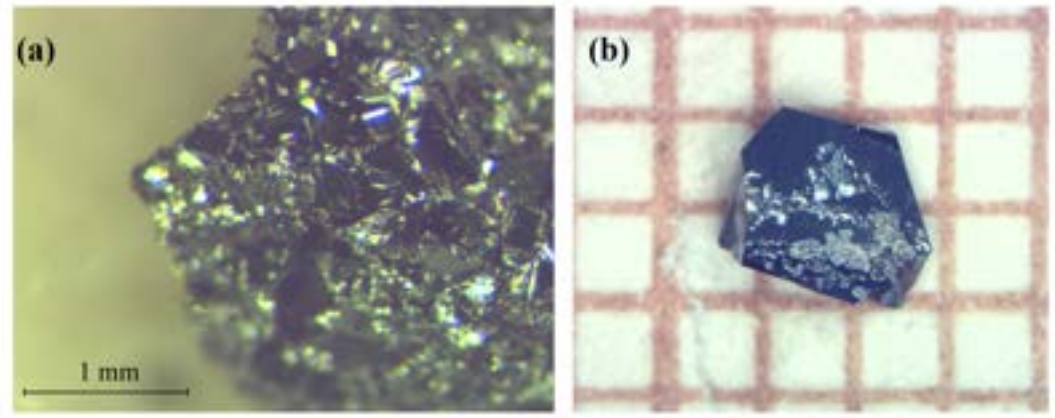

FIGURE 5.4: (a) $SrMg_2Sb_2$ crystals obtained from a 1.25:5:9 ratio and (b) a single crystal obtained from an optimized growth using a 1:5:15 ratio.

5.2 Crystal structure and physical properties

The pXRD patterns collected from the powdered single crystals of AMg_2Pn_2 compounds are presented in Figure 5.5. All four compounds crystallize in the same space group, $P\bar{3}m1$. The lattice parameters of the AMg_2Pn_2 compounds, obtained from LeBail analysis, are collected in Table 5.1, alongside the previously reported reference values. The lattice parameters change as expected, according to the atomic radii of the constituent elements (resulting in the largest unit cell found for the $BaMg_2Bi_2$ compound). Both the a and c parameters for all four of the investigated compounds are consistently slightly smaller than the reference values.

TABLE 5.1: Lattice parameters of AMg_2Pn_2 compounds obtained from LeBail analysis of pXRD data compared with the previously reported values from [54].

	Lattice parameters obtained from LeBail analysis [Å]	Reference lattice parameters [Å]
$BaMg_2Bi_2$	a = 4.8505(3)	4.90
	c = 8.2250(6)	8.33
$BaMg_2Sb_2$	a = 4.7667(2)	4.80
	c = 8.1296(4)	8.21
$SrMg_2Bi_2$	a = 4.7887(2)	4.83
	c = 7.9394(4)	7.98
$SrMg_2Sb_2$	a = 4.7029(2)	4.73
	c = 7.8201(4)	7.85

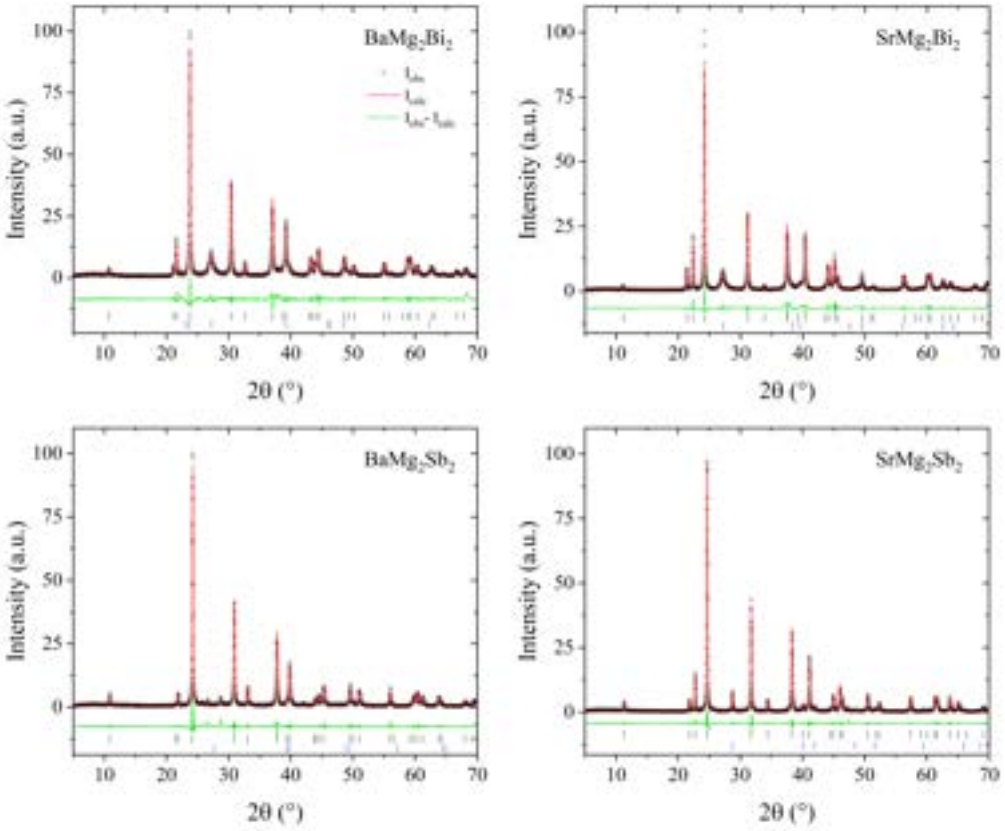

FIGURE 5.5: pXRD patterns of the AMg$_2Pn_2$ compounds (black points), with a LeBail fit (red line) and vertical bars marking the expected positions of the Bragg reflections of the targeted compound (upper row, black), and of elemental bismuth/antimony (lower row, blue). The difference between the observed and calculated intensities is shown below in green.

The measurement was repeated on the same powdered samples after 24 hours of air exposure in order to check the stability of the compounds. No decomposition was observed for any of the samples.

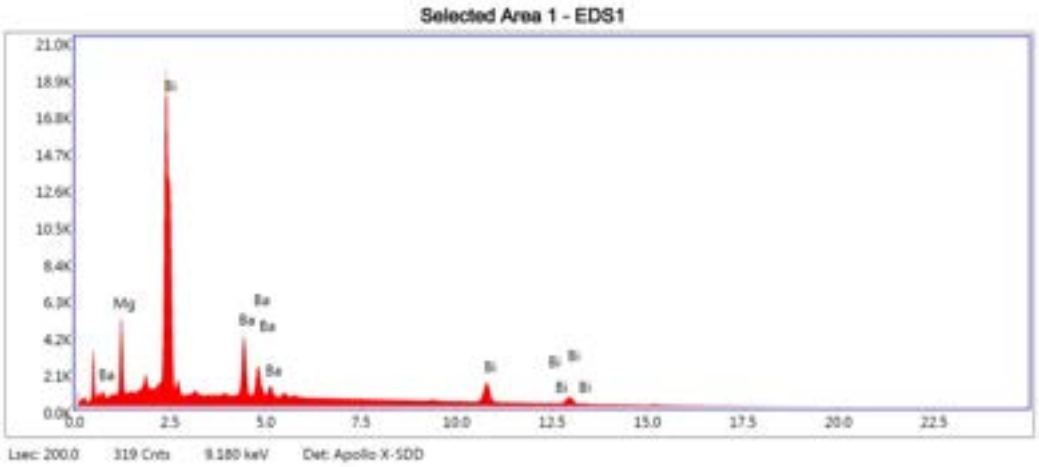

eZAF Smart Quant Results

Element	Weight %	Atomic %	Net Int.	Error %	Kratio	Z	A	F
MgK	9.58	44.09	192.91	8.87	0.0393	1.4546	0.2824	1.0000
BiM	63.60	34.06	924.08	1.89	0.5650	0.9347	0.9496	1.0009
BaL	26.82	21.86	208.37	4.69	0.2275	1.0025	0.8442	1.0023

FIGURE 5.6: The results of EDX analysis of the $BaMg_2Bi_2$ crystal shown in Figure 5.1.

From EDX analysis of the bismuthides, the elemental ratios across multiple tested crystals are in the range of 19-22:44-46:34-37 (A:Mg:Bi), indicating a consistent excess of Mg in relation to Bi for both of the compounds (an example of the results is presented in Fig 5.6). The issue of hole-doping due to off-stoichiometry was also encountered in [58]. In contrast to the bismuthides, the elemental ratio odbtained from EDX for $BaMg_2Sb_2$ is equal to 20:39:41, very close to the exact expected stoichiometry, for both the main body of the crystal and the uneven surface layers present on the crystal in the initial crystal growths.

The temperature dependence of heat capacity of all four samples was measured in the temperature range of 1.8 K to 200 K and is presented in Figure 5.7. The values of heat capacity are slightly higher for the bismuthides, in the whole temperature range, with the exception of the data points collected at the highest temperature. No phase transitions were observed down to the lowest measured temperature, including the $BaMg_2Bi_2$ compound, for which surface superconductivity was previously reported (no specific heat jump was reported in [59] either).

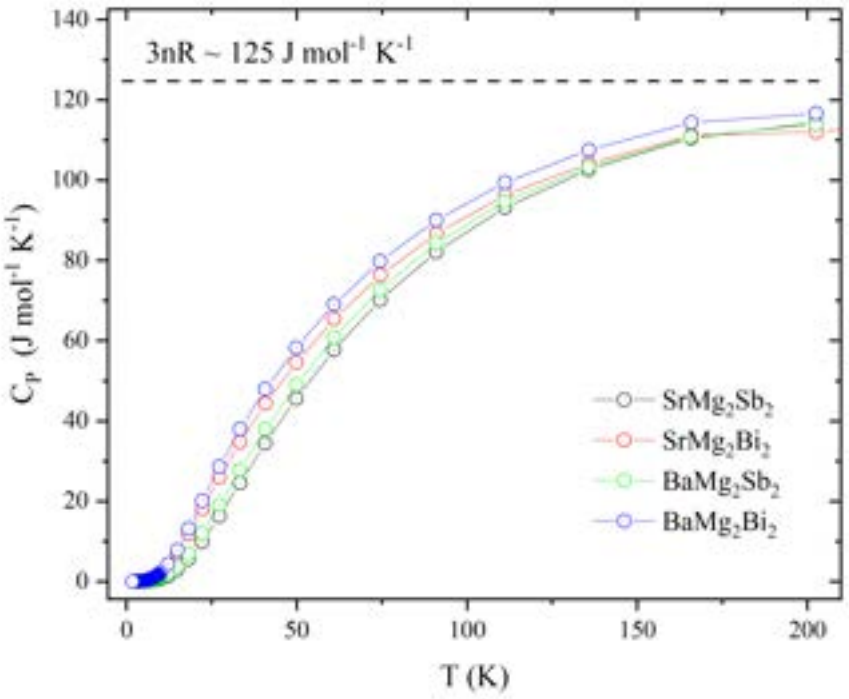

FIGURE 5.7: Heat capacity of the AMg_2Pn_2 compounds in the temperature range of 1.8 - 200 K.

Low temperature specific heat of the four compounds is presented in Figure 5.8, plotted as C_p/T versus T^2. The data shows a quadratic curvature, which is more pronounced in case of the two bismuthides. As attempting a linear fit in this region resulted in negative intercept values, the data was again fitted by including the additional δT^4 term (according to Eq. 4.5). A similar procedure, involving two additional terms, was performed by Pakhira et al. for $EuMg_2Bi_2$ [81], which is also considered to be a topological semimetal candidate.

The parameters obtained from the low temperature fit are collected in Table 5.2. Within the obtained error, the γ value for $SrMg_2Sb_2$ is equal to zero. For the other three compounds the values are also quite low, consistent with the previously reported $\gamma \approx 0$ for the related compounds $CaMg_2Bi_2$, $EuMg_2Bi_2$ and $YbMg_2Bi_2$ [56], which was attributed to low carrier concentrations. The θ_D values obtained for antimonides are higher than for the corresponding bismuthides.

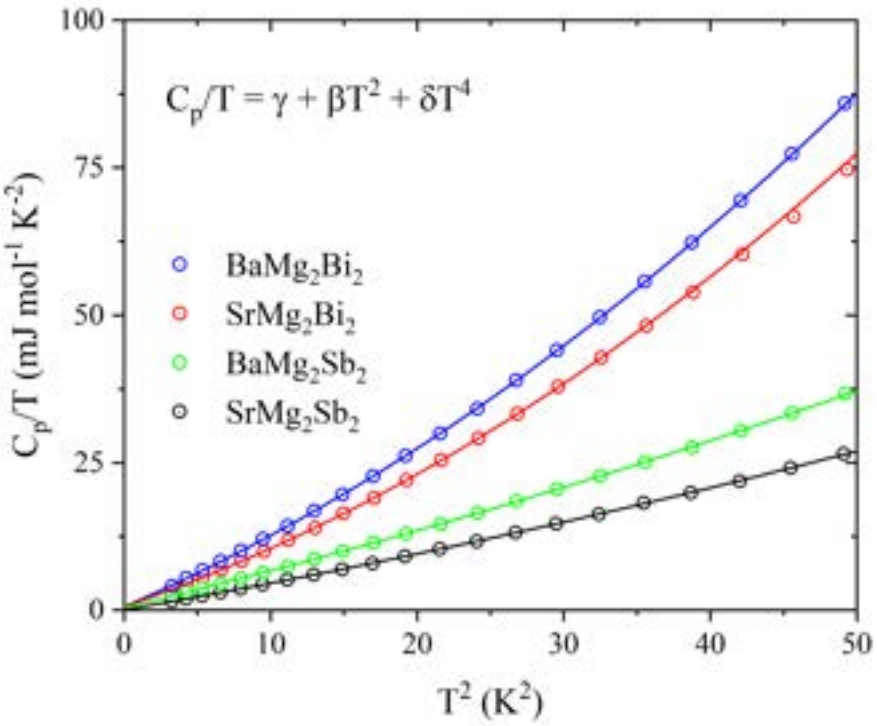

FIGURE 5.8: C_p/T versus T^2 heat capacity data of the AMg$_2Pn_2$ compounds in the low-temperature region, where the red lines represent the fit to Equation 4.5.

TABLE 5.2: Parameters obtained from the low temperature specific heat data of the AMg$_2Pn_2$ compounds.

	$BaMg_2Bi_2$	$BaMg_2Sb_2$	$SrMg_2Bi_2$	$SrMg_2Sb_2$
$\gamma(mJmol^{-1}\,K^{-2})$	0.59(7)	0.44(2)	0.63(4)	0.06(3)
$\beta(mJmol^{-1}\,K^{-4})$	1.08(1)	0.599(3)	0.846(6)	0.432(4)
$\delta(mJmol^{-1}\,K^{-6})$	0.0133(3)	0.0027(1)	0.0138(2)	0.0021(1)
$\theta_D(K)$	208.0(6)	253.2(4)	225.6(5)	282.3(9)

Electrical resistivity measurements were attempted for all four compounds but were ultimately unsuccessful, due to degradation of the samples. Contrary to the previously reported stability of at least a week in [58] and the pXRD data collected from powdered crystals after showing no decomposition over 24 hours, the crystals used for the measurements were found to physically disintegrate over the course of the measurement. Crumbling of the samples was particularly noticeable on the edges, but the top surface was also affected, disturbing the electrical contacts and making data collection impossible.

Chapter 6

$A_4T_7Pn_6$ compounds

The investigation of this family of compounds ensued after the previously unreported compound, $Mg_4Pd_7As_6$, was detected incidentally as one of the reaction products of a synthesis targeting another compound. Motivated by a recent report of a new compound, $MgPd_2Sb$, found to be the first Mg-based full Heusler superconductor (T_c = 2.2 K [82]), an attempt was made to obtain its As-bearing analogue $MgPd_2As$. The initially targeted compound $MgPd_2As$ was never obtained, however $Mg_4Pd_7As_6$ was synthesized and found to be a superconductor.

The characterisation of $Mg_4Pd_7As_6$, including the synthesis, physical properties and theoretical calculations, was published in *Advanced Electronic Materials* [83], in collaboration with dr hab. Bartłomiej Wiendlocha and dr Sylwia Gutowska (AGH University of Science and Technology, Kraków).

6.1 $Mg_4Pd_7As_6$

6.1.1 Synthesis and crystal structure determination

The synthesis procedure used for $MgPd_2Sb$ consisted of a two-step solid state reaction using a PdSb precursor and an excess of magnesium. Following the exact procedure using an equivalent Pd-As precursor did not yield the desired phase; the originally targeted $MgPd_2As$ was never synthesized. Instead, the main phase of the sample appeared to crystallize in a body-centered cubic structure with a large unit cell ($\sim$ 8.2 Å). This previously unreported compound was found to belong to the $U_4Re_7Si_6$ family.

The first several intentional synthesis attempts targeting $Mg_4Pd_7As_6$, using a pre-reacted Pd-As precursor or pure elements, did not yield a single-phase sample and the presence of large amounts of Pd_2As was detected in

the pXRD patterns in both approaches.

For further attempts, an alternative precursor Mg_3As_2 was employed. Magnesium flakes and arsenic pieces were taken in an approximately 3:2 ratio, with a slight excess of Mg (5 %) to account for its evaporation during heating. The elements were sealed in an evacuated quartz tube and heated to 580 °C in a chamber furnace. After 48 h, the obtained reddish material was thoroughly ground into powder in a glovebox, due to its possible toxicity and instability in air. The precursor was then mixed with palladium powder and freshly-ground arsenic in a 4:21:10 (Mg_3As_2:Pd:As), effectively resulting in an element ratio of 4:7:6. After thorough mixing, the powder was pressed into a pellet, placed in an alumina crucible and sealed. It was then heated to 570 °C at a rate of 25 °C/h, held there for 50 h and finally air-quenched to room temperature. After re-grounding and re-pressing the powder, the heating was repeated at a higher temperature of 590 °C, in hopes of improving the crystallization of the sample. The pXRD pattern is shown in Figure 6.1. The crystal structure was refined by Rietveld method, the details of which are presented in Table 6.1. The analysis leads to the calculated lattice parameter of a = 8.2572(1) Å which, despite similar values of the atomic radii of the included transition metals, is noticeably larger than for the analogue $Mg_4T_7As_6$ compounds (see Table 2.2).

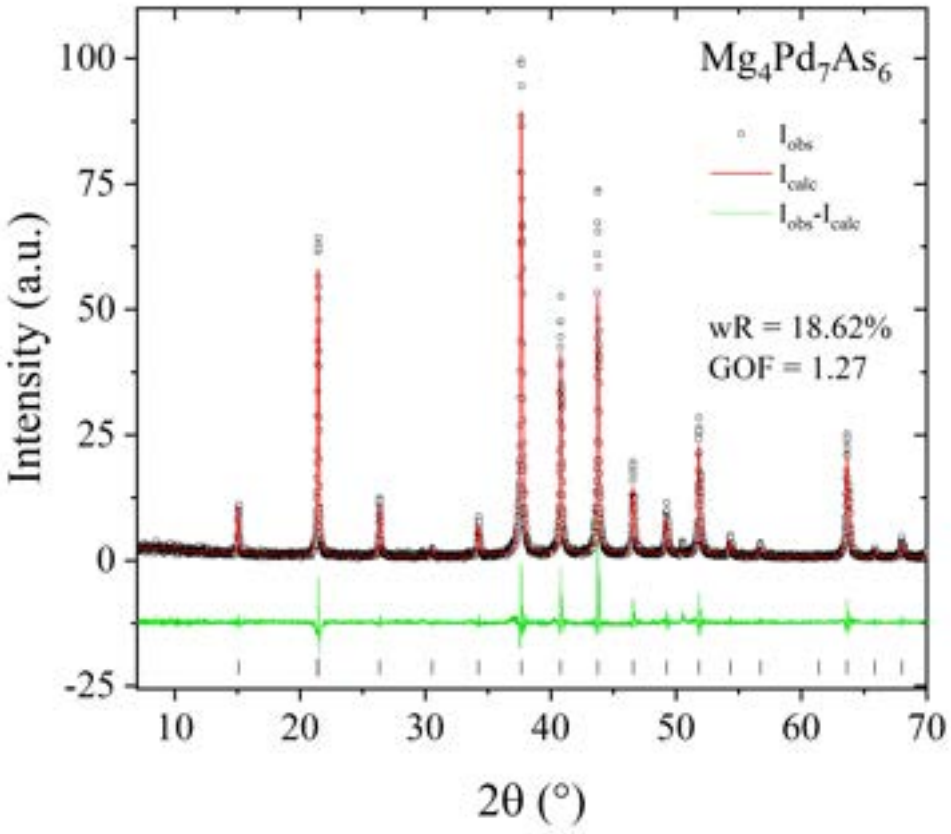

FIGURE 6.1: pXRD pattern of $Mg_4Pd_7As_6$ (black points) with a Rietveld fit (red line). Vertical bars mark the position of the expected Bragg reflections of the $Im\bar{3}m$ structure. The difference between the observed and calculated intensities is shown below in green.

TABLE 6.1: Crystallographic data of $Mg_4Pd_7As_6$ obtained from the Rietveld refinement. Numbers in parentheses are uncertainties of the least significant digits.

$Mg_4Pd_7As_6$, T = 300 K				
Space group	*Im-3m* (no. 229)			
Unit cell parameter a	8.2570(1) Å			
Cell volume	562.94(3) Å^3			
Z	2			
Formula weight	1291.55 g/mol			
Density	7.620 g/cm^3			
Structure parameters:				
	x	y	z	U_{iso} (Å^2)
Mg(8c)	1/4	1/4	1/4	0.018(2)
Pd(12d)	0	1/4	1/2	0.040(1)
Pd(2a)	0	0	0	0.030(1)
As(12e)	0	0	0.3094(2)	0.031(1)

Various experiments focused on varying the temperature of the reaction in the 540 – 590 °C range showed that the side phases present in the sample are quite sensitive to temperature changes, even as slight as 5 °C. The additional pXRD reflections, corresponding to Pd_2As and another unidentified compound, appeared interchangeably, seemingly depending more heavily on whether the temperature was lowered or raised in relation to the previous heating step and less on the temperature of the reaction itself.

An attempt was made to obtain single crystals of the compound following the route previously described by Wurth et al. [66] for the analogue compounds, $Mg_4Ir_7As_6$ and $Mg_4Rh_7As_6$, where single crystals were grown from constituent elements in a lead melt, with the Mg:M:As:Pb element ratio of 1:2:2:20 for M=Rh and 4:7:6:≈30 for M=Ir. The growths were carried out in alumina crucibles placed in evacuated tubes, partially back-filled with argon. The ampules were heated for approximately 48 h at 1000 °C, after which the solid lead matrix was dissolved using a mixture of glacial acetic acid (CH_3COOH) and 30% solution of hydrogen peroxide. Small metallic-gray cube- and octahedron-shaped crystals of the target compounds were found among other reaction products [66].

The crystal growth was recreated using 4:7:6:30 (Mg:Pd:As:Pb) ratio, with a total mass of ≈ 3 g. The material was placed in an alumina crucible, with a second crucible placed on top of it to minimize possible evaporation. In order to minimize the risks associated with working with arsenic, the elements were weighted in a glove box and the crucible containing the material was double sealed in two quartz tubes. The sealed ampule was placed in a chamber furnace at 400 °C, heated to 1000 °C at a rate of 40 °C/h and held there for 48 hours. Upon taking it out and cooling down to room temperature, noticeable, brown markings could be seen on the crucible and light signs of damage to the inner quartz tube could be observed, in a form of "spider-web" fractions near the bottom. The lead flux was etched away using the aforementioned 1:1 hydrogen peroxide and acetic acid mixture. While still submerged in the etching liquid, the obtained precipitate consisted of a light gray powder with no visible crystals of any significant size. Once the mixture was filtered, flushed with deionized water and left to dry in air the precipitate quite quickly changed color to milky-white. The pXRD pattern of the dried powder shows the presence of an apatite compound $Pb_5(AsO_4)_3OH$, and triclinic $Pb_2As_2O_7$ or possibly monoclinic $PbHAsO_4$. Due to this issue,

crystal growth using lead as flux was determined to not be a viable method for $Mg_4Pd_7As_6$.

6.1.2 Physical properties

Characterization of $Mg_4Pd_7As_6$ started with measuring the zero-field-cooled (ZFC) and field-cooled (FC) dc magnetization as a function of temperature below 6 K. The measurement was conducted in the applied magnetic field μ_0H = 1 mT. Figure 6.2 presents the volume magnetic susceptibility χ_v, where a transition to a superconducting state can be clearly seen in the ZFC data. A much weaker diamagnetic response can also be seen in the FC data, which is typical for polycrystalline materials and is associated with flux penetration and pinning at the grain boundaries of the sample. The superconducting transition temperature T_c was determined from the intersection of a horizontal line following the extrapolated normal state data and a line lying along the steepest slope of the ZFC curve (the two lines are marked in blue in the figure). The obtained value was T_c = 5.5 K.

The presented data has been corrected for the demagnetization effects, with a demagnetization factor (N) determined from the volume magnetization vs. magnetic field measurement, according to a method which will be described in the subsequent section. After the correction the ZFC curve reaches the value of -1 at the lowest temperatures, indicating that the sample is fully in a superconducting (Meissner) state and exhibiting full shielding.

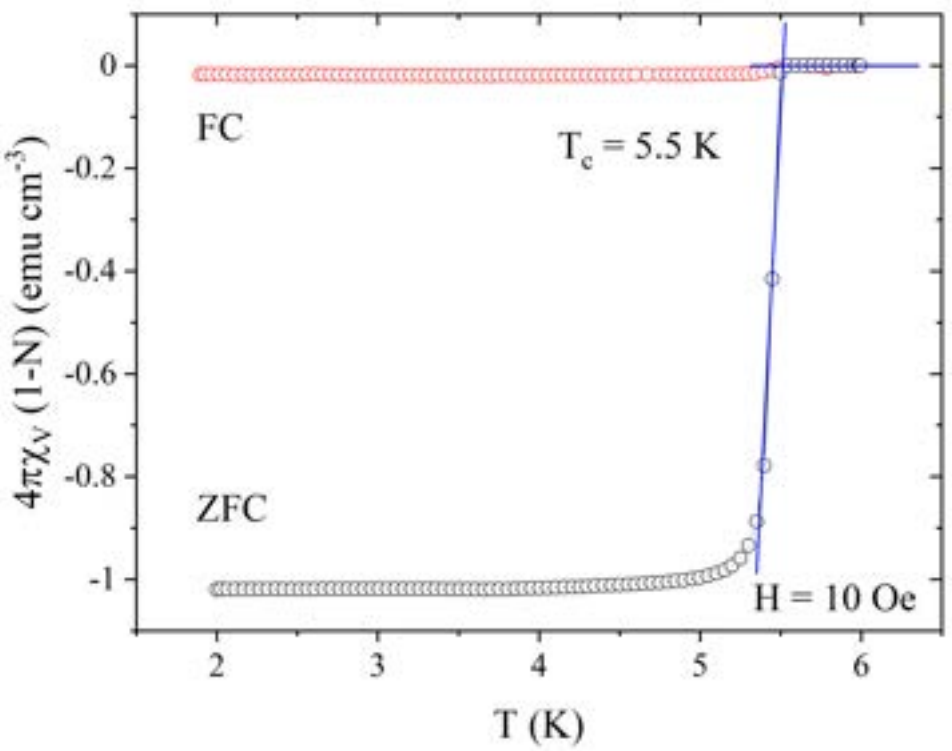

FIGURE 6.2: Zero-field-cooled (ZFC) and field-cooled (FC) magnetic susceptibility curves of $Mg_4Pd_7As_6$ corrected for the demagnetizing factor.

The results of a sequence of isothermal magnetization measurements conducted under low applied magnetic field is presented in Figure 6.3. The data was collected at several temperatures below the T_c, ranging from 1.9 to 5 K. The shape of the curves indicates that $Mg_4Pd_7As_6$ is a type II superconductor (the characteristic behaviour is visible clearly only for the higher temperatures). The 1.9 K data was used to determine the demagnetization factor. Assuming a perfectly diamagnetic response, the collected $M_v(H)$ data can be fitted with a linear function $M_{fit} = aH + b$. The obtained slope can then be used to calculate N from the formula:

$$-a = \left(\frac{1}{4\pi(1-N)}\right) \tag{6.1}$$

This resulted in $N = 0.58$, a value which is in the range expected for the general shape of the sample used in the measurement.

From this series of measurements, the lower critical field $H_{c1}(0)$ could be determined by evaluating the points at which the curves deviate from the expected linear behavior. The linear fit $M_{fit} = aH + b$ was also applied

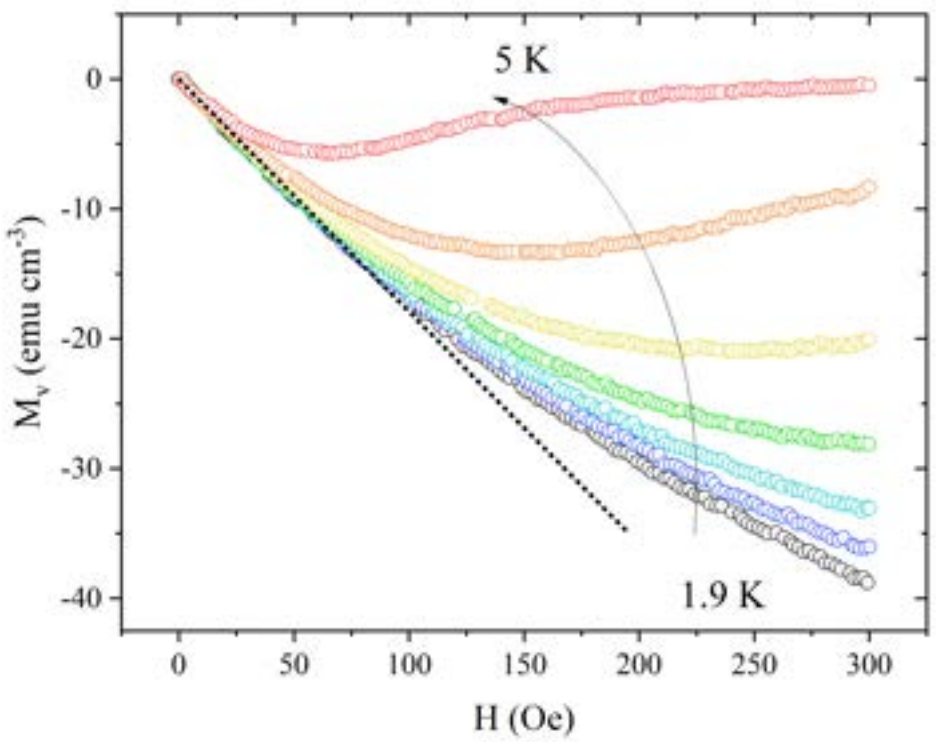

FIGURE 6.3: Isothermal $M_v(H)$ measurements measured for temperatures below the T_c.

to the remaining curves. A plot illustrating the difference between the experimental data points and the obtained fit, M_v - M_{fit}, was constructed for each temperature. $H^*_{c1}(T)$ values were taken as the point at which the line following the original deviation from the linear behaviour crossed the horizontal M_v - M_{fit} = 0 line. Due to the noisiness present in the low-field region of the measurements, this crossing point could not always be determined in a straightforward manner. In order to estimate the resultant uncertainty of $H^*_{c1}(T)$, the data points scattered around the 0 line were surrounded by an "envelope". The uncertainty was then defined as the span between the points at which the M_v - M_{fit} curve crosses the upper and the lower level of the threshold lines. Example of the curves for two selected temperatures are presented in Figure 6.4.

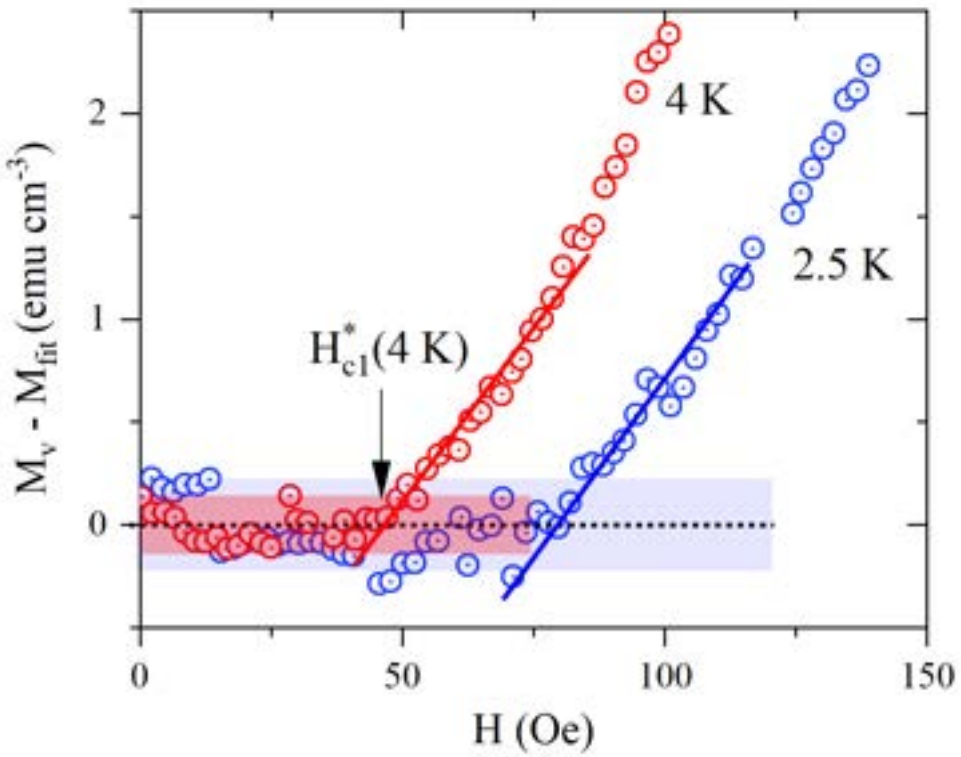

FIGURE 6.4: Examples of the M_v - M_{fit} curves used to determine $H^*_{c1}(T)$ for selected temperatures.

Figure 6.5 shows the points obtained via this method plotted as a function of temperature. One additional data point corresponding to the lower critical field estimated from a subsequent zero-field electrical resistivity measurement is marked with a blue triangle. The data were fitted with an equation:

$$H^*_{c1}(T) = H^*_{c1}(0)\left(1 - \left(\frac{T}{T_c}\right)^2\right) \tag{6.2}$$

resulting in a value of $H^*_{c1}(0)$ equal to 95(1) Oe. Correcting this result for the previously established demagnetization factor according to the $H_{c1}(0) = H^*_{c1}(0)/(1-N)$ relation gave the final value of $H_{c1}(0) = 226(3)$ Oe.

The temperature-dependent electrical resistivity ρ(T) of $Mg_4Pd_7As_6$ is presented in the main panel of Figure 6.6. The measurement was conducted in the temperature range of 1.9 – 314 K, in applied magnetic field ranging from 0 to 1.6 T. The resistivity of the sample decreases in the full temperature range ($\frac{d\rho}{dT} < 0$), showing typical metallic behaviour. The RRR of the sample, defined as RRR = ρ(300 K)/ρ_0, where ρ_0 is the resistivity value taken right

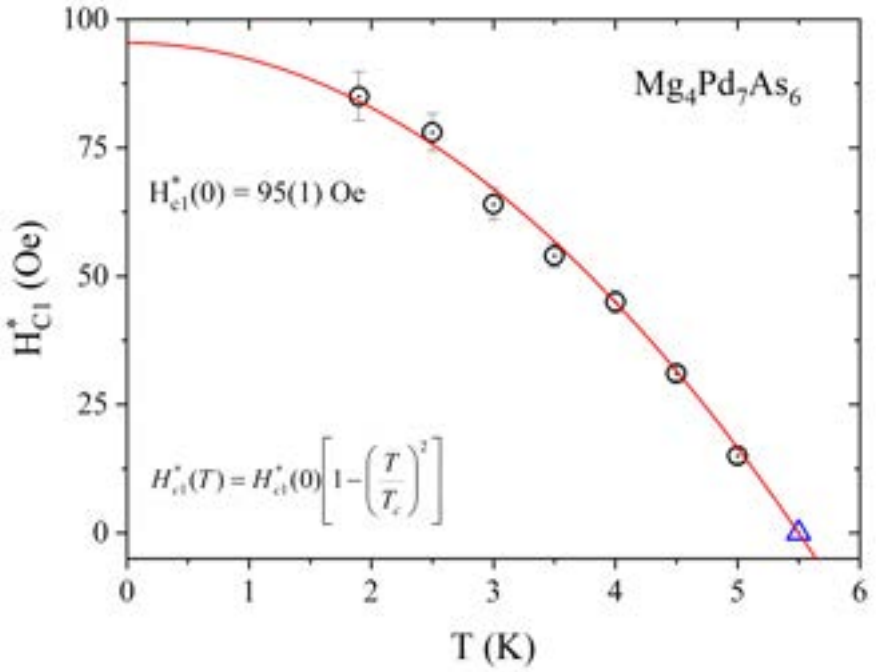

FIGURE 6.5: Temperature dependence of the lower critical field H_{c1} determined from isothermal $M_v(H)$ measurements. The additional zero-field data point marked as a blue triangle is taken from the subsequent electrical resistivity measurement.

above T_c, is close to 4. This relatively low value is expected for a polycrystalline material. The inset of Figure 6.6 shows the magnetic field dependence of resistivity ρ(H) at the lowest measured T = 1.9 K. For this temperature the upper critical field H_{c2} can be estimated to be 1.66 T (taken as the mid-point of the superconducting transition).

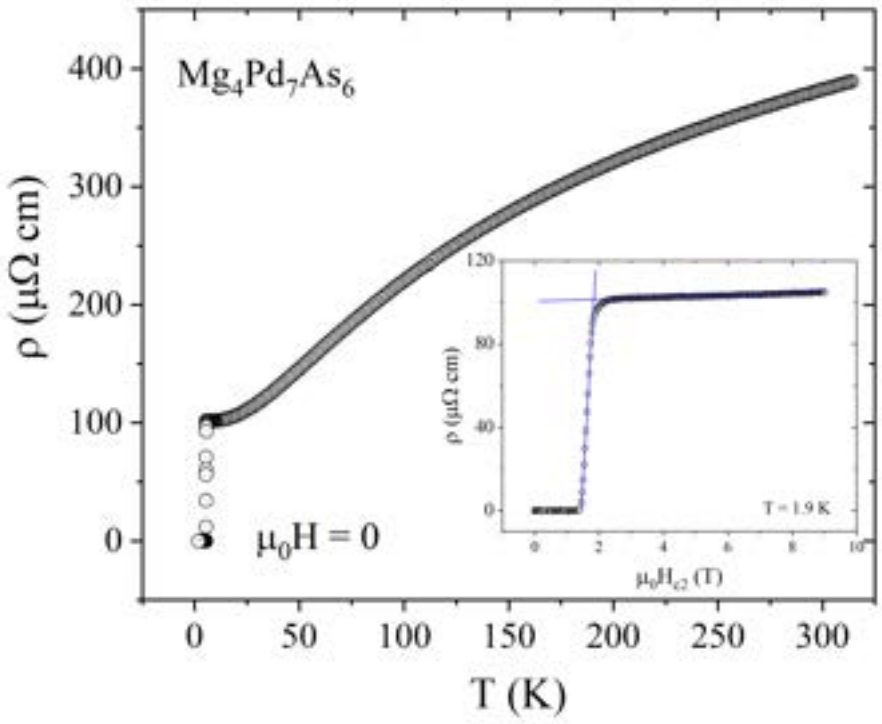

FIGURE 6.6: Temperature dependence of electrical resistivity of $Mg_4Pd_7As_6$ in the absence of external magnetic field. Inset: magnetic field dependence measured at a constant temperature of 1.9 K, with the estimated upper critical field marked by the intersection of the curve with a horizontal line at half-height

A close-up of the resistivity drop in the low temperature region is presented in Figure 6.7. T_c can be defined as the temperature corresponding to the 50% drop of the resistivity value and is equal to 5.51 K, in agreement with the value obtained from the magnetization measurement. In the zero-field measurement the transition into the superconducting state is sharp, with a width close to 0.05 K. The transition starts to broaden for increasing values of the applied magnetic field and shifts to lower values, until it falls outside of the measurement temperature range for fields > 1.6 T.

Taking the temperature values corresponding to the half-heights of each of the $\rho(T)$ curves, a plot of H_{c2} vs. temperature can be constructed and the value of $H_{c2}(0)$ can be calculated. The data points shown in Figure 6.8 were fitted using the Ginzburg-Landau function:

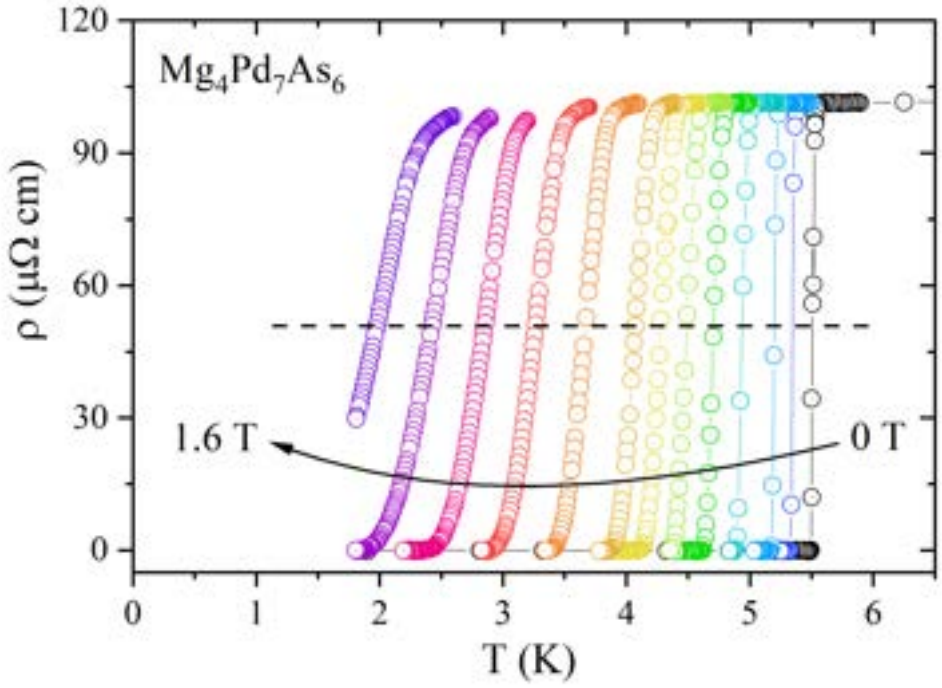

FIGURE 6.7: Low-temperature region of the electrical resistivity curves in the vicinity of the superconducting transition, under applied magnetic fields between 0 and 1.6 T.

$$H_{c2}(T) = H_{c2}(0)\frac{1-\left(\frac{T}{T_c}\right)^2}{1+\left(\frac{T}{T_c}\right)^2} \tag{6.3}$$

The fit yielded $\mu_0 H_{c2}(0) = 2.09(1)$ T. The previously estimated point of $H_{c2}(1.9)$ = 1.66 T is added to the plot and marked with a blue star. Although it was not part of the fitted data its value is consistent with the obtained fit line, falling only marginally above it.

Having obtained both the upper and lower critical field values the next two important parameters related to the fundamental length scales of a superconductor can be determined. The coherence length ξ_{GL}, defined as the distance within which the superconducting electron concentration cannot significantly change in an applied magnetic field, can be obtained from the Ginzburg-Landau formula:

$$H_{c2} = \frac{\Phi_0}{2\pi\xi_{GL}^2} \tag{6.4}$$

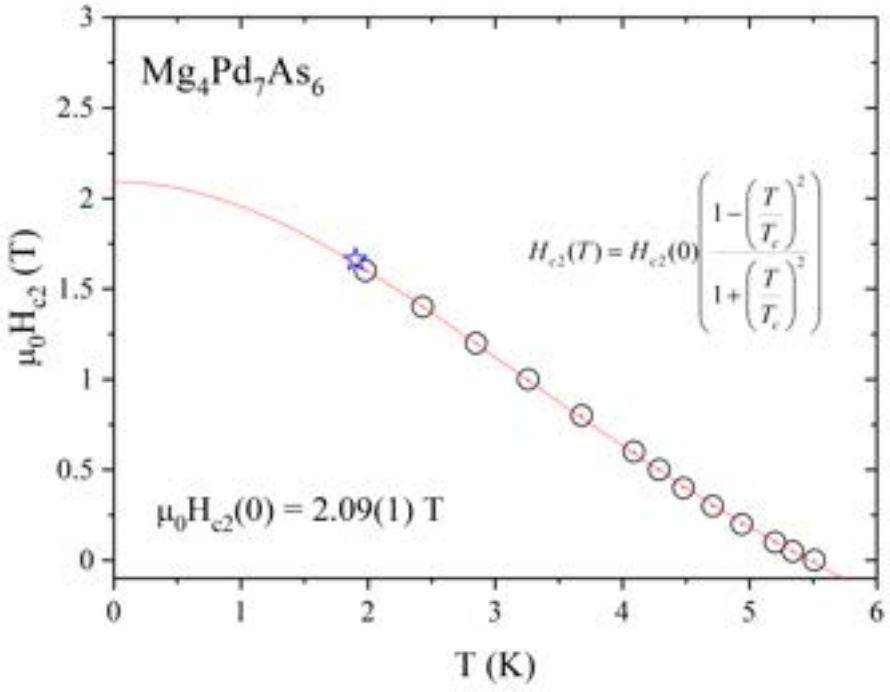

FIGURE 6.8: Temperature dependence of the upper critical field $H_{c2}(T)$ determined from resistivity measurements (marked with black circles) and the point estimated from ρ(H) measurement (marked with a blue star).

where Φ_0 = hc/(2e) is the quantum flux. Using the $\mu_0 H_{c2}(0) = 2.09$ T value gives $\xi_{GL}(0) = 125$ Å.
From the relation:

$$H_{c1} = \frac{\Phi_0}{4\pi\lambda_{GL}^2} \ln(\frac{\lambda_{GL}}{\xi_{GL}}) \tag{6.5}$$

the superconducting penetration depth λ_{GL} can be calculated, related to the depth up to which the magnetic field can penetrate a superconductor. Using $\mu_0 H_{c1}(0) = 22.6$ mT results in λ_{GL} = 1346 Å.

These two parameters can be connected to each other via the Ginzburg-Landau parameter κ_{GL} according to the relation:

$$\kappa_{GL} = \frac{\lambda_{GL}}{\xi_{GL}}. \tag{6.6}$$

Using the obtained $\xi_{GL}(0)$ and λ_{GL} parameters, κ_{GL} is estimated to be 10.7, which according to the Ginzburg-Landau theory firmly classifies it as a type-II superconductor (as $10.7 \gg \frac{1}{\sqrt{2}}$).

Finally, this parameter together with the upper and lower critical field values can be used to obtain the thermodynamic critical field from:

$$H_{c1}H_{c2} = H_c^2 \ln \kappa \tag{6.7}$$

giving $\mu_0 H_c(0) = 136$ mT.

To complete the characterization of the superconducting properties and confirm the bulk character of superconductivity in $Mg_4Pd_7As_6$ the specific heat was measured in the temperature range of 1.9 – 210 K, with an applied magnetic field ranging from 0 to 3.5 T. The zero-field temperature dependence of specific heat is presented in Figure 6.9. At higher temperatures (near room temperature) the values are expected to approach the value of 424 J mol^{-1} K^{-1}, according to the Dulong-Petit limit $C = 3nR$ (here $n = 17$).

The blue line shows the fit using the combined Debye-Einstein heat capacity model, consisting of electronic and phonon (C_{Debye} and $C_{Einstein}$, marked in Figure 6.9 in red and green, respectively) contributions, where k determines the weight of the Debye component:

$$C_p = \gamma T + (1-k)C_{\text{Einstein}} + kC_{\text{Debye}} \tag{6.8}$$

The $C_{Einstein}$ and C_{Debye} are defined as:

$$C_{\text{Einstein}} = n_E R\left(\frac{\Theta_E}{T}\right)^2 \exp\left(\frac{\Theta_E}{T}\right)\left(\exp\left(\frac{\Theta_E}{T}\right) - 1\right)^{-2} \tag{6.9}$$

$$C_{\text{Debye}} = 3n_D R\left(\frac{T}{\Theta_D}\right)^3 \int_0^{\frac{\Theta_D}{T}} \frac{x^4 \exp(x)}{(\exp(x)-1)^2} dx \tag{6.10}$$

The fit resulted in the Debye temperature equal to $\theta_D = 351(4)$ K, the Einstein temperature $\theta_D = 104(3)$ K and $k = 0.72(2)$.

Figure 6.10(a) shows the close-up of the low temperature specific heat data in the absence of applied magnetic field, presented as C_p/T versus T. The characteristic lambda-shaped anomaly, associated with the transition to the superconducting state, can be seen at the temperature of 5.45 K, determined through the equal entropy construction marked in the Figure by blue lines. The T_c obtained from this method is very slightly lower than the values obtained from the magnetization and resistivity measurements.

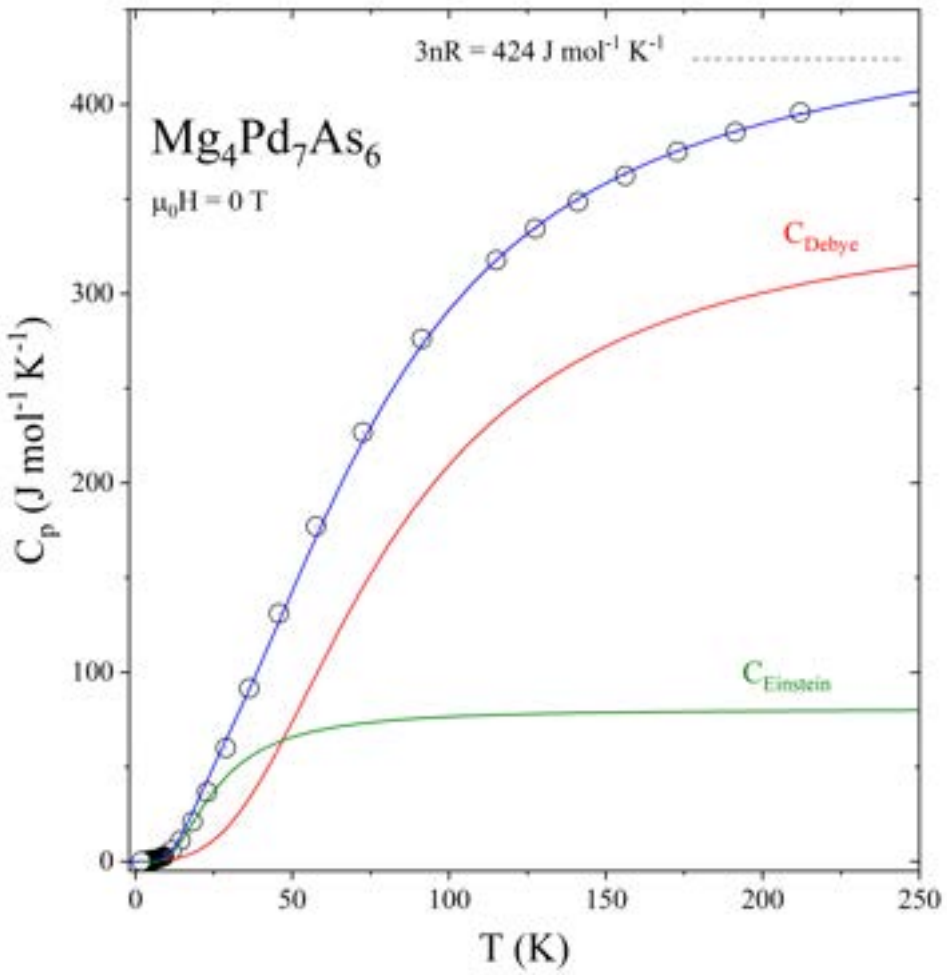

FIGURE 6.9: The temperature dependence of specific heat of $Mg_4Pd_7As_6$ in zero magnetic field with a fit to a combined model $C_p = \gamma T + (1-k)C_{\text{Einstein}} + kC_{\text{Debye}}$.

The normal-state data, collected under the applied magnetic field of $\mu_0 H = 3.5$ T, is presented in Figure 6.10(b) as C_p/T versus T^2. In this way, the expected linear behaviour can be clearly seen. The data below 20 K^2 was fitted using the relation:

$$\frac{C_p}{T} = \gamma + \beta T^2 \tag{6.11}$$

resulting in the following values: γ = 48(1) mJ mol^{-1} K^{-2} and β = 2.80(6) mJ mol^{-1} K^{-4}.

Knowing the value of γ the normalized superconducting specific heat jump can be determined according to $\frac{\Delta C_p}{\gamma T_c}$. The obtained value of 1.27 is

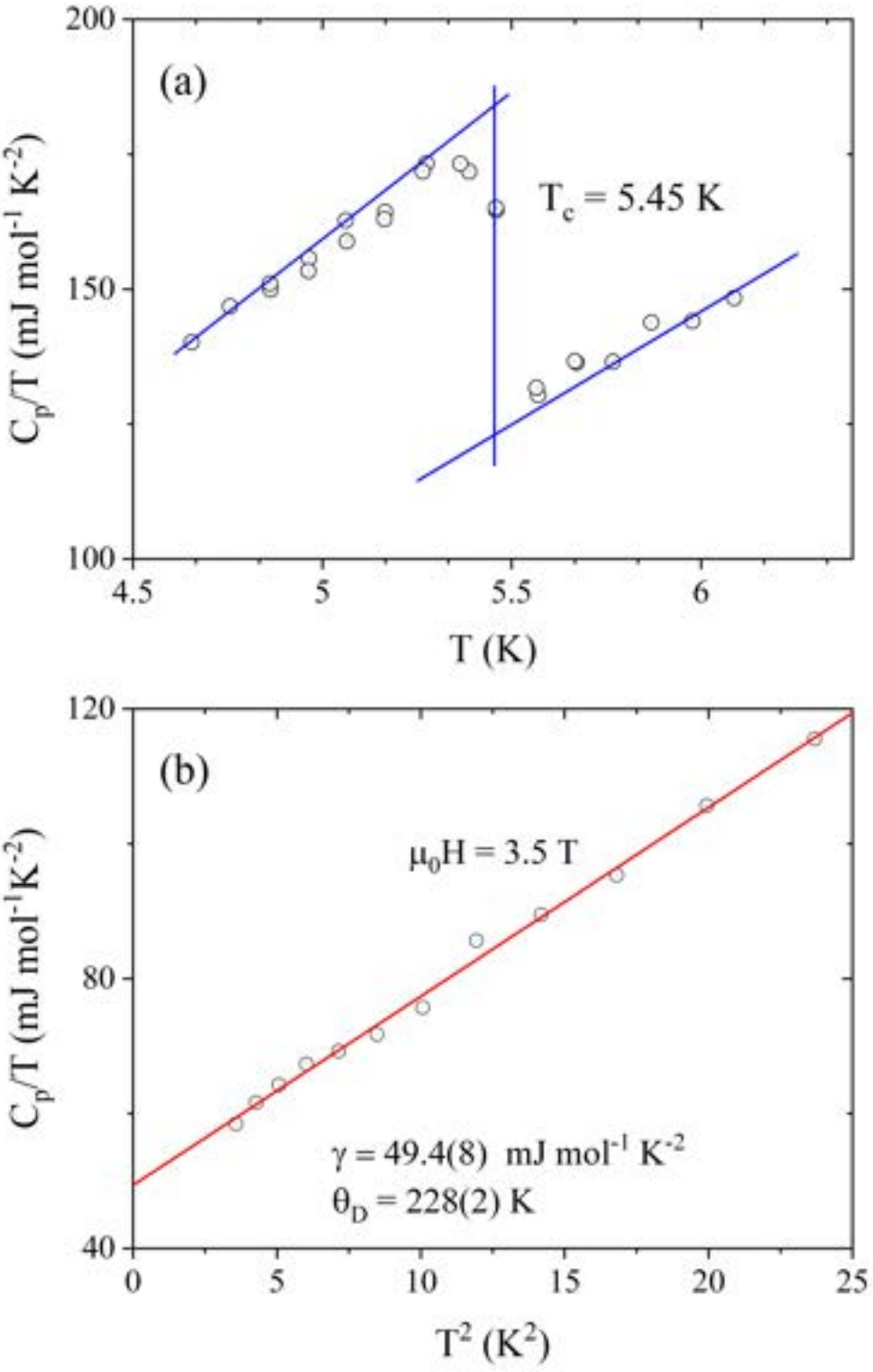

FIGURE 6.10: (a) Zero-field C_p/T versus T data showing the specific heat anomaly. The blue lines represent the equal-entropy construction used to determine the normalized specific heat jump. (b) Normal-state C_p/T versus T^2 data in the low temperature region measured at $\mu_0 H$ = 3.5 T. The red line represents the linear fit used to determine electronic and phonon contributions to specific heat.

slightly lower than the 1.43 predicted by the BCS theory for a weakly-coupled superconductor, but this phenomenon is commonly observed for many superconductors i.e. OsB_2 [84]. Using this value of β, the Debye temperature can be calculated according to:

$$\theta_D = \sqrt[3]{\frac{12\pi^4 nR}{5\beta}} \tag{6.12}$$

The obtained value of $\theta_D = 228(2)$ K is in a similar range to that of $Yb_4Ru_7As_6$, where $\theta_D = 250$ K [69], but significantly lower than the other isostructural materials $Yb_4T_7Ge_6$ ($\theta_D \simeq 330$ K) and $U_4Ru_7Ge_6$ ($\theta_D = 330$ K) [85, 86].

The electron-phonon coupling parameter λ was calculated by inserting θ_D and T_c into the inverted McMillan's relation:

$$\lambda = \frac{1.04 + \mu^* \ln(\frac{\theta_D}{1.45T_c})}{(1 - 0.62\mu^*)\ln(\frac{\theta_D}{1.45T_c}) - 1.04} \tag{6.13}$$

where $\mu*$ is the Coulomb pseudopotential parameter, typically ranging between 0.10 - 0.15. Taking $T_c = 5.45$ K and $\theta_D = 228$ K together with $\mu^* = 0.13$, commonly assumed for conventional superconductors, results in $\lambda = 0.72$. This value indicates moderate coupling.

All of the calculated parameters characterizing $Mg_4Pd_7As_6$ are collected in the Table 6.2.

TABLE 6.2: Superconducting parameters of $Mg_4Pd_7As_6$

Parameter	Unit	Value
T_c	K	5.45
$\mu_0 H_{c1}(0)$	mT	22.6
$\mu_0 H_{c2}(0)$	T	2.09
$\mu_0 H_c(0)$	mT	136
λ	-	0.72
$\xi_{GL}(0)$	Å	125
$\lambda_{GL}(0)$	Å	1346
κ_{GL}	-	10.7
γ	$\frac{\text{mJ}}{\text{mol}\cdot\text{K}^2}$	48
β	$\frac{\text{mJ}}{\text{mol}\cdot\text{K}^4}$	2.8
θ_D	K	228
$\frac{\Delta C_p}{\gamma T_c}$	-	1.27
RRR	-	4

6.2 $Mg_4Ir_7As_6$

A synthesis route for single crystals of $Mg_4Ir_7As_6$ as outlined by Wurth et al. [66] was described in a previous section. The same report briefly mentions the attempts at obtaining single-phase polycrystalline samples of Ir- and Rh-bearing compounds via solid-state synthesis using pure elements, with limited success.

An attempt to grow single crystals following the described route proved unsuccessful with no observed crystal growth, either of the 4-7-6 or any other compound.

A polycrystalline sample of $Mg_4Ir_7As_6$ was prepared, once again using the 4:21:10 ratio of the previously synthesized Mg_3As_2, iridium powder and arsenic. Initially, the temperature of the first heat treatment was the same as for $Mg_4Pd_7As_6$, but it turned out to be too low for iridium to react. The temperature was gradually increased, with recurrent re-grinding, until first traces of the 4-7-6 phase were found in the pXRD pattern after reaching 610 °C. As the pattern still indicated predominantly unreacted iridium, the temperature was further increased. This resulted in some part of Ir reacting directly with arsenic resulting in the appearance of $IrAs_2$; this issue was also encountered in [66]. At this point, further temperature treatment focused on exploring the balance of secondary phases, Ir and $IrAs_2$. The temperature could be raised to 810°C without noticeably increasing the amount of $IrAs_2$, however, its levels rose significantly above 900°C. Thus, the sample annealed at 810 °C was selected for further characterization, on the basis of having the best balance of the main phase and the side phases. The pXRD pattern is presented in Figure 6.11. The lattice parameter obtained from the LeBail analysis was a = 8.0852(3) Å, consistent with the value of 8.082(2) Åwhich was reported previously [66].

Preliminary magnetic measurements of the $Mg_4Ir_7As_6$ sample showed a possible onset of superconductivity at temperatures close to 2 K. The same sample was later tested on a Dynacool Helium-3 system down to 0.4 K, however, no transition was observed.

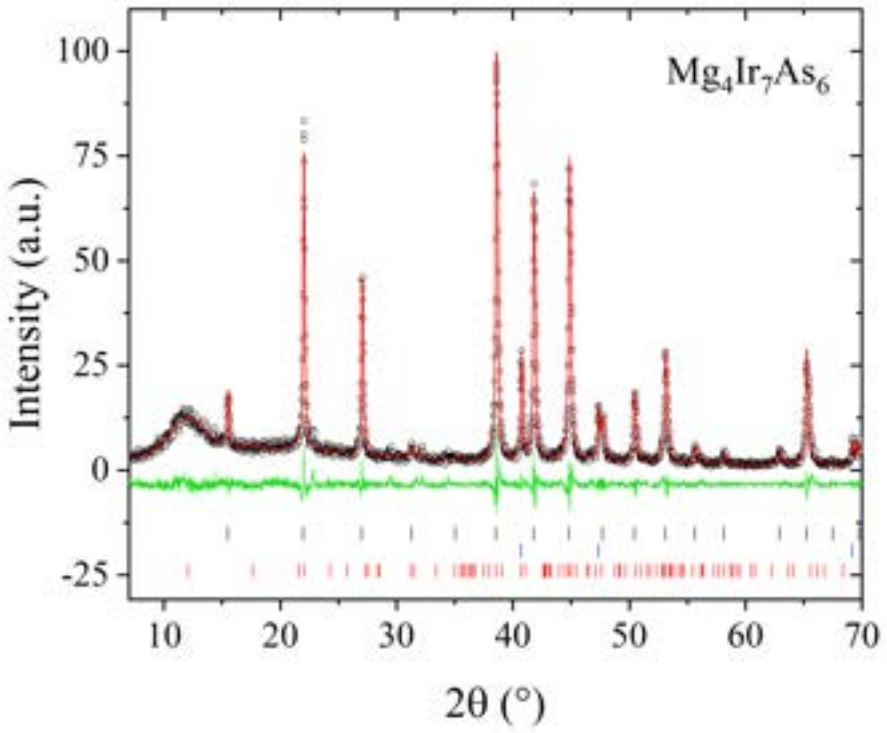

FIGURE 6.11: pXRD pattern of $Mg_4Ir_7As_6$ (black points), with a LeBail fit (red line) and vertical bars marking the expected positions of the Bragg reflections of the target compound (upper row, black), metallic iridium (middle row, blue) and$IrAs_2$ (lower row, red). The difference between the observed and calculated intensities is shown below in green.

6.3 $Mg_4Rh_7As_6$

$Mg_4Rh_7As_6$ was successfully obtained using Pb flux, Mg flakes, Rh powder and As pieces taken in a 1:2:2:20 Pb ratio. Due to unsatisfactory results of the previous attempts, which closely followed the previously reported procedure, the temperature profile of the growth was slightly altered. The sealed ampule was placed in a chamber furnace at 400 °C, heated to 1000 °C at a rate of 40 °C/h and held there for 2 hours. After that time, to improve homogenization, the temperature was rapidly cycled between 960 °C (T_{f1}) and 1040 °C (T_{f2}) several times, and subsequently held at the higher end for another 8 hours. Finally, the furnace was slowly cooled down to 1000 °C at a rate of 1 °C/h, at which point the sample was taken out to finish cooling to RT naturally. The markings on the crucibles were still present (as was the case for $Mg_4Pd_7As_6$), however, no damage to the quartz tubes was observed this time. After etching, small, irregularly shaped crystals could be found in the collected precipitate, with no visible changes observed once exposed to air

and dried.

Several of the crystals were collected for a magnetic measurement. A beginning of a superconducting transition could be observed around 7.2 K which can be ascribed to un-etched Pb left on the sample. Since the diamagnetic signal was weak and no other transition could be seen as the temperature was lowered, it can be concluded that $Mg_4Rh_7As_6$ does not show superconductivity down to 1.9 K.

6.4 Summary of other synthesis attempts

6.4.1 $Mg_4Pt_7As_6$

The first solid-state synthesis attempt of $Mg_4Pt_7As_6$, using the previously prepared Mg_3As_2, platinum powder and arsenic at the temperatures used for the other 4-7-6 compounds resulted in a mixture of $PtAs_2$ and another unidentified phase, with no $Mg_4Pt_7As_6$ detected in the sample. Lowering the reaction temperatures to 520 °C followed by a second heating at 530 °C quite unexpectedly produced a single-phase sample of $MgPt_7$. None of the subsequent attempts of varying the temperature profiles or element ratios were successful.

6.4.2 $Mg_4Rh_7P_6$

Repeating the procedure used for $Mg_4Rh_7As_6$ (element ratio of 1:2:2:20 Pb) resulted in a dark grey powder, with two distinct types of small crystals mixed in it - small cubes and larger, elongated rectangles. The pXRD pattern revealed the obtained material to be a mixture of $Mg_4Rh_6P_4$ and RhP_2. The former compound also appeared as a side phase during solid-state reactions in [66]; nothing other than the structural information has been reported (hexagonal crystal structure, space group $P\bar{6}m2$) [87].

The target compound $Mg_4Rh_7P_6$ was not obtained, even when following the reported procedure exactly. Despite the unintended results, the obtained compounds were still tested for superconductivity (via magnetization measurement) but it was not observed down to 1.9 K.

6.4.3 $Mg_4Pd_7P_6$

When the steps of the $Mg_4Rh_7As_6$ growth were once again repeated for $Mg_4Pd_7P_6$, the pXRD pattern of the obtained powder matched PdP_2. As before, the sample was tested for superconductivity but it was not observed. For the second growth, the ratio of Pd:P was adjusted according to the phase diagram [88] to 65:35, resulting in a final element ratio of 1:2.6:1.4:20 Pb. The temperature of the reaction was also raised to 1060 °C and no slow cooling was used, in order to avoid the conditions promoting the growth of PdP_2. Nevertheless, even after incorporating these changes PdP_2 remained the main phase in the reaction products and no signs of $Mg_4Pd_7P_6$ were detected.

6.4.4 $RE_4Ir_7Sb_6$ and $T_4Ir_7Ge_6$ series

An attempt to obtain a series of pollycrystalline $RE_4Ir_7Sb_6$ was undertaken following the synthesis method described for Rh and Ru analogs, as reported in [64]. Pieces of the rare earth metals (Sc, Y, Lu, Sc), iridium and antimony were taken in a near-stoichiometric ratio, with a 2 % excess of Sb, to account for its possible evaporation, and arc-melted under slight underpressure of argon. In later attempts, Sb was also re-added after significant mass loss was noticed following the first melting.

Deviating from the pnictides, arc-melting was also employed to briefly investigate a series of $T_4Ir_7Ge_6$ germanides, where T = group 4 transition metal, since Ge- and Si-based compounds constitute the majority of the 4-7-6 family. The constituent elements were taken in a stoichiometric ratio and no significant losses were observed.

The obtained samples were subjected to additional heat treatment in a range of temperatures (500 - 1000 °C) for several days. All of the pXRD measurements, of both the as-cast and heat-treated samples, showed a mixture of binary or equiatomic ternary phases (e.g. ZrIrGe, HfIrGe); no 4-7-6 phase was observed in any of the attempts.

Chapter 7

Summary

In this work selected families of ternary pnictide compounds were investigated.

The work on the 111 pnictides focused on improving or developing single crystal flux growth procedures, in order to obtain high-quality samples which would facilitate further measurements. Altogether, single crystals of ten different compounds were obtained and the influence of various growth parameters on the crystals were investigated. Chemical doping of selected samples was attempted, but ultimately proved not possible. It did, however, lead to an improvement in the growth of BaAgAs crystals. Adding small amounts of Eu to the starting element mixture affected the growing conditions and resulted in larger crystals with well-defined shape, despite not actually incorporating Eu into the crystal structure.

Physical properties of selected compounds were investigated, including electrical resistivity, heat capacity and magnetization. The signs of superconductivity in SrAgBi and YbAgBi could be seen in ρ(T) measurements, but no transition was observed in the heat capacity (in case of SrAgBi) or magnetization data (in case of YbAgBi), putting into doubt the intrinsic character of this phenomenon. For selected samples (CaCuSb, CaAgSb, YbCuBi, YbAgBi) magentoresistance was measured and was found to be positive in all cases, with the highest value of $\sim$ 110 % obtained for YbCuBi (for T = 1.9 K and $\mu_0 H$ = 9 T). The Ba- and Sr-bearing compounds were a subject of further study via ARPES measurements, in order to investigate their electronic structures.

High-quality single crystals of AMg$_2$$Pn_2$ compounds, where A = Ba, Sr and Pn = Sb or Bi were also obtained from flux growth. It is the first time that the antimonides, $BaMg_2Sb_2$ and $SrMg_2Sb_2$, have been grown in a form of bulk crystals. The electronic structure of these compounds was also investigated via ARPES.

Finally, a new superconductor $Mg_4Pd_7As_6$ was found. The previously unreported material is the first Pd-bearing compound crystallizing in the $U_4Re_7Si_6$ structure and the first one in the ternary Mg–Pd–As system. As it is also the only 4-7-6 compound that contains both a group 10 element and a pnictogen, it makes it the new member with the highest electron valence count (overtaking $Lu_4Rh_7Sb_6$, VEC = 105). For $Mg_4Pd_7As_6$ VEC = 108, which gives 6.35/atom. The measurements of physical properties of $Mg_4Pd_7As_6$ confirm it to be a bulk type-II superconductor, with the superconducting transition taking place at T_c = 5.5 K. The lower critical field, obtained from the isothermal field-dependent magnetization measurements, was found to be $\mu_0 H_{c1}(0) = 22.6$ mT, while the upper critical field was determined to be $\mu_0 H_{c2}(0) = 2.09$ T, based on the electrical resistivity measurements. The calculated electron–phonon coupling constant indicates moderate-coupling (λ = 0.72).

The search for other superconducting compounds in the 4-7-6 family was conducted, first by replacing Pd with other transition metals (i.e. Ir, Pt) and later extending the scope beyond Mg-bearing arsenides ($RE_4Ir_7Sb_6$ and $T_4Ir_7Ge_6$ series). As of the writing of this thesis, $Mg_4Pd_7As_6$ remains the only superconducting member of this family.

Appendix A

Supplementary Material for Chapter 5

Attached is the manuscript titled "Uncovering surface states of the Dirac semimetal $BaMg_2Bi_2$" which has been submitted to *Physical Review B*, including the Supplementary Information.

Uncovering surface states of the Dirac semimetal $BaMg_2Bi_2$

A. De Vita**, [1]J. Bakkelund**, [2]H. Świątek**, [3]M. J. Winiarski,[3] C. V. Nielsen,[4] F. Bertran,[5] F. Miletto Granozio,[6] J. A. Miwa,[4] T. Klimczuk,[3,*] C. Bigi,[7,†] and F. Mazzola[6,‡]

[1]*Fritz Haber Institut der Max Planck Gesellshaft, Faradayweg 4–6, 14195 Berlin, Germany*

[2]*Department of Engineering Sciences, University of Agder, NO-4879 Grimstad, Norway*

[3]*Faculty of Applied Physics and Mathematics, Advanced Materials Centre, Gdansk University of Technology, Narutowicza 11/12, 80-233, Gdansk, Poland*

[4]*Department of Physics and Astronomy, Interdisciplinary Nanoscience Center, Aarhus University, 8000 Aarhus C, Denmark*

[5]*Synchrotron SOLEIL, L'Orme des Merisiers, Départementale 128, F-91190 Saint-Aubin, France*

[6]*CNR-SPIN, c/o Complesso di Monte S. Angelo, IT-80126 Napoli, Italy*

[7]*Synchrotron SOLEIL, L'Orme des Merisiers, Départementale 28, 91190 Saint-Aubin, France*

Abstract

$BaMg_2Bi_2$ is a Dirac semimetal characterized by a simple Dirac cone crossing the Fermi level at the center of the Brillouin zone, protected by C_3 rotational symmetry. Together with its Sr-based analogue $SrMg_2Bi_2$, it has been proposed as a promising candidate for a chemically driven topological switch: while $SrMg_2Bi_2$ is an insulator, $BaMg_2Bi_2$ exhibits non-trivial topological features. A detailed understanding of its electronic structure is essential to elucidate its electronic and transport properties. Previous photoemission studies confirmed the Dirac nature of $BaMg_2Bi_2$, but were limited to high photon energies, which compromised the resolution and hindered direct comparison with theoretical predictions. In this work, we employ high-resolution angle-resolved photoemission spectroscopy (ARPES) to overcome this limitation, providing a comprehensive picture of the low-energy electronic structure. Our measurements reveal the presence of previously unobserved surface states, which, however, remain topologically trivial and elucidate more comprehensively the electronic structure of this semimetal filling previous discrepancies between theory and experiment.

** These authors contributed equally.

The interplay between crystalline symmetry and band inversion – often facilitated by spin-orbit coupling – plays a central role in the emergence of novel topological phases of matter [1–4]. Among these, topological Dirac semimetals (TDS) represent a distinct class, differing fundamentally from conventional topological insulators. TDS materials have garnered significant interest due to their exceptionally high carrier mobility [5, 6], the presence of surface Fermi arcs that give rise to unconventional transport phenomena [7–9], and their typically large, non-saturating magnetoresistance [10, 11]. From a band structure perspective, a TDS is characterized by massless Dirac fermions, manifested as linear band crossings (Dirac nodes) at or near the Fermi level. Importantly, under external perturbations such as strain or applied magnetic fields, Dirac nodes can split into Weyl nodes, thereby inducing non-trivial topological transitions. These tunable responses make TDSs highly promising for applications in next-generation electronic and spintronic devices.

* Corresponding author: tomasz.klimczuk@pg.edu.pl

† Corresponding author: chiara.bigi@synchrotron-soleil.fr

‡ Corresponding author: mazzola@iom.cnr.it

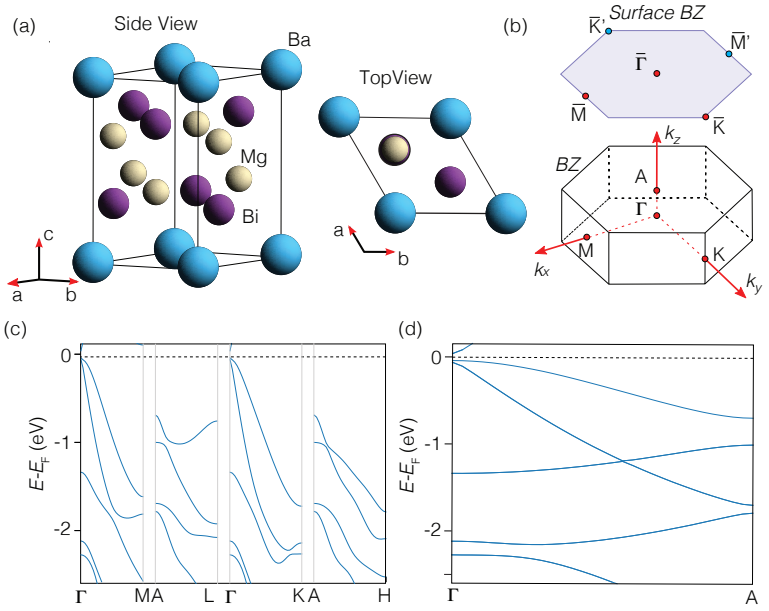

FIG. 1. (a) Side and top view of the structure and unit cell of $BaMg_2Bi_2$ crystal, showing the typical $CaAl_2Si_2$ structure. (b) Resulting Brilluoin zone with high symmetry directions indicated. The surface Brillouin zone is also indicated. (c) Bulk electronic structure along the in-plane high symmetry directions. (d) Same of (c) but along the out of plane.

$BaMg_2Bi_2$ crystallizes in the $CaAl_2Si_2$-type structure, corresponding to space group $P\bar{3}m1$ (No. 164). This crystallographic configuration enforces a C_3 rotational symmetry, which plays a pivotal role in stabilizing the system's only Dirac cone—located at the center of the Brillouin zone and linearly dispersing across the Fermi level (See Fig.1.) [12]. Crucially, despite hosting a symmetry-protected Dirac node, $BaMg_2Bi_2$ is topologically trivial, thus providing a clean, model platform for investigating textbook Dirac fermions in the absence of additional topological features [13]. Moreover, this structure exhibits considerable chemical flexibility; for instance, substituting Ba with other alkaline earth or rare-earth elements [14, 15] can effectively modulate the spin-orbit coupling strength by altering the local atomic environment. Such tunability is particularly valuable for exploring topological phase transitions in this material family.

Previous experimental studies have explored the electronic structure of $BaMg_2Bi_2$ us-

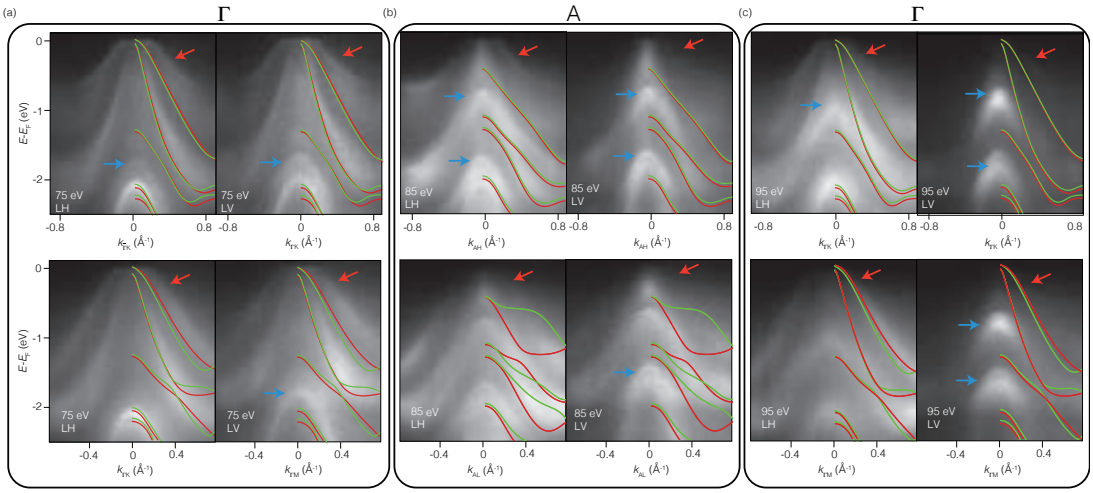

FIG. 2. (a) Electronic structure of $BaMg_2Bi_2$ along the Γ-K (top) Γ-M (bottom) directions for both light polarizations indicated in the figure. (b) Same but with photon centered at the A point and (c) Next bulk Γ.

ing angle-resolved photoemission spectroscopy (ARPES), confirming the Dirac nature of this compound through the observation of dispersing massless fermions [13]. However, measurements conducted at relatively high photon energies suffer from limited resolution, which hinders a clear visualization of other electronic states. Furthermore, the absence of polarization-dependent measurements and systematic photon energy scans in the low-energy regime motivates further investigation to shed light on additional features important for transport. Here, by combining high-resolution angle-resolved photoemission spectroscopy (ARPES) with variable light polarization and photon energy [16, 17], together with density functional theory (DFT) calculations, we address this shortcoming. Our study reveals the presence of additional states—some arising from k_z broadening artifacts, and others which we attribute to the surface state manifold of $BaMg_2Bi_2$.

High-quality single crystals of $BaMg_2Bi_2$ were grown via a self-flux method using the constituent elements in a 1.5:5:9 molar ratio (Ba:Mg:Bi). The mixture was loaded into an alumina crucible, sealed in an evacuated quartz tube, and heated to 900°C for 12 h. It was then slowly cooled to 650°C at a rate of 1°C/h. The crystals were separated from the flux by centrifugation. The resulting crystals exhibited smooth surfaces and a pronounced metallic lustre. ARPES measurements were carried out at the CASSIOPEE beamline of the

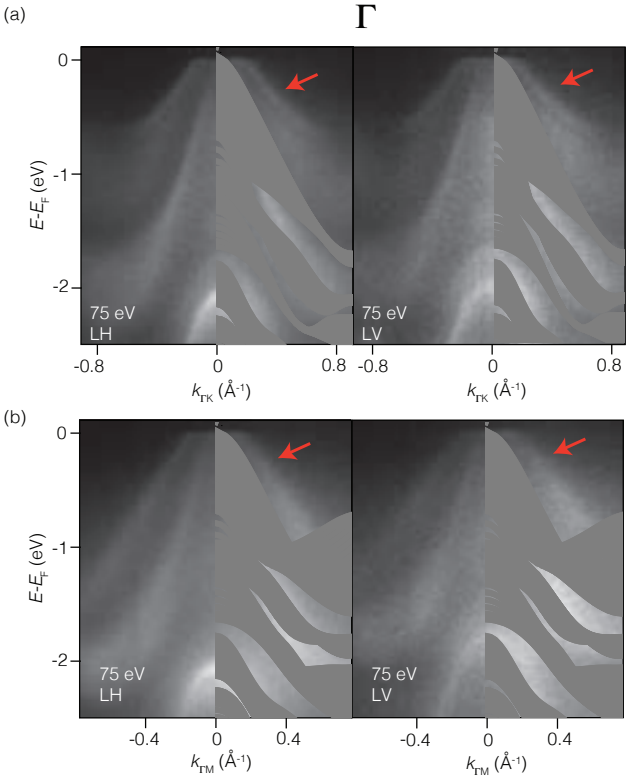

FIG. 3. (a) Electronic structure of $BaMg_2Bi_2$ along the Γ-K and (b) Γ-M (bottom) directions for both light polarizations indicated in the figure. DFT calculations have been overlaid and the gray colour indicates the projected bulk continuum.

synchrotron radiation facility SOLEIL (Paris), using both linear vertical (LV, *s*-polarized) and linear horizontal (LH, *p*-polarized) polarizations. In the geometry of this experimental setup, LV-polarized photons have their electric field vector entirely confined within the sample plane, while LH polarization introduces both in-plane and out-of-plane components of equal magnitude. ARPES was performed under ultrahigh vacuum conditions (UHV) at the base temperature of circa 20 K. The samples were prepared in a glovebox environment by affixing them to the sample plate using silver epoxy. They were subsequently top-posted and cleaved under UHV conditions at 20 K. This procedure ensures that the surface properties are not destroyed by low vacuum and adsorption of impurities, a situation that can often occur if samples are cleaved at higher temperature then cooled down.

In addition, first-principles calculations were performed using the QuantumESPRESSO DFT package. The self-consistent calculations were carried out on a $6 \times 6 \times 6$ k-point grid with a 60 Ry energy cutoff, employing fully relativistic projector augmented wave (PAW) pseudopotentials. It is important to note that, due to the lack of six-fold rotational symmetry in the crystal, there are two inequivalent M-points and two inequivalent K-points, which are related by a 60° rotation of M and K around the (001)-axis. For the (001)-slab model, where the (001)-surface is truncated by vacuum, the system retains only one symmetry, as the truncation breaks inversion symmetry. The remaining symmetry operation is a 180° rotation about the (110)-axis combined with inversion. This breaking of inversion symmetry could permit the existence of spin-split surface states. Time-reversal symmetry is preserved in both the bulk and slab geometries.

Leading from our combined experimental and theoretical data, we present the bulk-calculated electronic structure alongside ARPES spectra acquired at variable photon energies—hence variable k_z—and polarizations, as displayed in Fig.2. Overall, and consistent with previous literature [13], there is broad agreement between the ARPES data and the DFT calculations. Nevertheless, as indicated by the red and blue arrows in Fig.2, several bands at each k_z value are neither captured by DFT nor reported in earlier experiments. The measurements span a photon-energy range that covers multiple Brillouin zones; for brevity, we show one repetition in the main text, while additional energies are provided in the Supplementary Information (Supplementary Figs. 1 and 2). Because the unidentified features persist across the entire k_z range and for both light polarizations, they cannot be attributed to photoemission matrix-element effects; instead, they point to an intrinsic characteristic of the electronic structure. These discrepancies are evident along both the Γ–K and Γ–M high-symmetry directions.

Mapped in Fig. 2, the calculated dispersions along Γ–K and the symmetry-inequivalent Γ–K′ directions are shown in red and green, respectively.. Given the photon beam's lateral size of approximately 100 μm, domains rotated by 180° are likely probed simultaneously. The resulting superposition of Γ–K and Γ–K′ contributions renders the experimental spectra more symmetric and partially broadens the linewidths. To account for this, we overlay both inequivalent cuts in the theoretical plot. However, domain averaging alone cannot reproduce

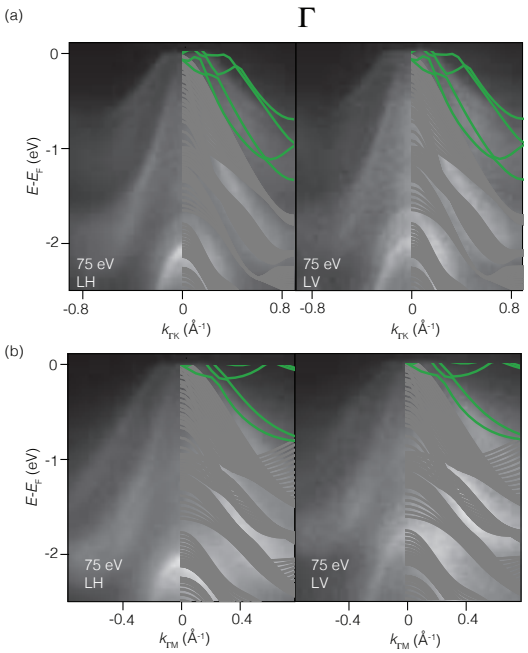

FIG. 4. (a) Electronic structure of $BaMg_2Bi_2$ along the Γ-K and (b) Γ-M (bottom) directions for both light polarizations indicated in the figure. DFT calculations have been overlaid and the gray colour indicates the projected bulk continuum. The green colour indicate the surface states, calculated as described in the text.

the additional spectral weight highlighted above, indicating that further mechanisms must be considered.

Examining the data presented in Fig.2, we note that the photon energy spans a full k_z period, covering the path from Γ to the next Γ point. The bands reach their maximum binding energy at the center of the Brillouin zone and their minimum at the A point. This implies that no spectral weight should appear above the calculated bands shown in Fig.2a and Fig. 2c; in particular, the features indicated by the red arrows are not expected to be present. In contrast, additional features appearing at lower binding energies—still previously unobserved—could be more straightforwardly explained. We now focus on these latter bands, highlighted by the blue arrows.

Remarkably, despite an overall modulation and redistribution of intensity, all bands re-

main visible across the entire photon energy range. Although this may initially seem inconsistent with previous studies, the observed phenomenology can be reconciled by considering the strong k_z broadening in both the ARPES spectra and the bulk-projected simulations. Experimentally, k_z broadening manifests as a general filling of spectral intensity over the entire k_z-dependent dispersion range. This effect arises because, despite tuning to a specific photon energy, multiple k_z values are effectively probed simultaneously. Such a condition is common in materials with strongly three-dimensional electronic structures [18, 19], and it is therefore not surprising that it occurs in $BaMg_2Bi_2$.

Driven by this interpretation, our bulk-projected DFT calculations successfully reproduce the spectral broadening observed in the ARPES data. This comparison is shown in Fig.3 for the bulk Γ point, along both the Γ–K and Γ–M directions. As clearly illustrated, the filling of the electronic states seen in the ARPES measurements finds a simple yet compelling explanation: several of the states that appeared experimentally—previously unreported—are now accounted for. However, other features in the electronic structure, highlighted with red arrows in both Fig.2 and Fig. 3, remain unexplained within the framework of bulk-projected DFT, suggesting a non-bulk origin.

As a means of verification, we performed surface-state calculations using a slab geometry that is infinite in the x- and y-directions but truncated along z (the (001)-axis). The slab consisted of 24 atomic layers with a 12 Å vacuum separating the two surfaces. In Fig. 4, the projected bulk continuum is shown in gray (obtained by projecting the bulk band structure onto the (001)-plane), while the surface states extracted from the slab calculation are highlighted in green (identified based on their probability density).

Since the Γ and M points are time-reversal invariant momenta, the surface states remain degenerate at these points, meaning that their spin splitting vanishes. However, this does not hold at K, as time-reversal symmetry alone does not enforce degeneracy there due to the crystal symmetry. Examining the number of Fermi-level crossings of the surface states between high-symmetry points, we find that it is always even. This indicates that the surface states are topologically trivial. If they were nontrivial, we would expect them to exhibit an odd number of Fermi-level crossings and ultimately connect the bulk conduction

and valence bands.

In summary, we have conducted a comprehensive investigation of the electronic structure of $BaMg_2Bi_2$ using high-resolution angle-resolved photoemission spectroscopy, combined with polarization- and photon-energy-dependent measurements, and supported by both bulk and slab-based density functional theory calculations. Our results confirm that $BaMg_2Bi_2$ hosts a symmetry-protected Dirac node at the center of the Brillouin zone, stabilized by the underlying threefold rotational symmetry of the $CaAl_2Si_2$-type structure. While the Dirac dispersion has been previously reported, our experiments reveal additional features in the spectral function—some attributable to strong out-of-plane momentum (k_z) broadening and others not accounted for by calculations of the bulk electronic structure.

Through bulk-projected simulations, we demonstrate that the observed intensity filling in the photoemission spectra is a natural consequence of momentum broadening along the out-of-plane direction in a material with significant three-dimensional electronic character. However, distinct features that remain unexplained within the bulk framework are successfully captured by calculations performed on a finite slab geometry. These slab-derived bands, while not topologically nontrivial, constitute an essential part of the low-energy electronic structure and are likely to contribute to the transport properties of $BaMg_2Bi_2$.

Altogether, our work not only reinforces $BaMg_2Bi_2$ as a model Dirac semimetal with topologically trivial character, but also uncovers additional electronic states—originating from both bulk and surface effects—that have gone undetected in previous studies. These findings highlight the importance of combining energy-, momentum-, and polarization-resolved spectroscopy with carefully constructed theoretical models in order to fully capture the complexity of the electronic landscape in candidate Dirac materials.

Acknowledgments:
F.M. greatly acknowledges the NFFA-DI funded by the European Union – NextGenerationEU, M4C2, within the PNRR project NFFA-DI, CUP B53C22004310006, IR0000015.

---

[1] B. M. Wojek, P. Dziawa, B. J. Kowalski, A. Szczerbakow, A. M. Black-Schaffer, M. H. Berntsen, T. Balasubramanian, T. Story, and O. Tjernberg, Band inversion and the topo-

logical phase transition in (pb,sn)se, Phys. Rev. B **90**, 161202 (2014).

[2] P. Narang, C. A. C. Garcia, and C. Felser, The topology of electronic band structures, Nature Materials **20**, 293 (2021).

[3] F. Mazzola, S. Enzner, P. Eck, C. Bigi, M. Jugovac, I. Cojocariu, V. Feyer, Z. Shu, G. M. Pierantozzi, A. De Vita, P. Carrara, J. Fujii, P. D. C. King, G. Vinai, P. Orgiani, C. Cacho, M. D. Watson, G. Rossi, I. Vobornik, T. Kong, D. Di Sante, G. Sangiovanni, and G. Panaccione, Observation of termination-dependent topological connectivity in a magnetic weyl kagome lattice, Nano Letters **23**, 8035 (2023).

[4] F. Mazzola, Y. Zhang, N. Olszowska, M. Rosmus, G. D'Olimpio, M. C. Istrate, G. G. Politano, I. Vobornik, R. Sankar, C. Ghica, J. Gao, and A. Politano, Fermiology of chiral cadmium diarsenide cdas2, a candidate for hosting kramers–weyl fermions, The Journal of Physical Chemistry Letters **14**, 3120 (2023).

[5] M. Neupane, S.-Y. Xu, R. Sankar, N. Alidoust, G. Bian, C. Liu, I. Belopolski, T.-R. Chang, H.-T. Jeng, H. Lin, A. Bansil, F. Chou, and M. Z. Hasan, Observation of a three-dimensional topological dirac semimetal phase in high-mobility cd3as2, Nature Communications **5**, 3786 (2014).

[6] J. Fujioka, R. Yamada, M. Kawamura, S. Sakai, M. Hirayama, R. Arita, T. Okawa, D. Hashizume, M. Hoshino, and Y. Tokura, Strong-correlation induced high-mobility electrons in dirac semimetal of perovskite oxide, Nature Communications **10**, 362 (2019).

[7] B. J. Wieder, Z. Wang, J. Cano, X. Dai, L. M. Schoop, B. Bradlyn, and B. A. Bernevig, Strong and fragile topological dirac semimetals with higher-order fermi arcs, Nature Communications **11**, 627 (2020).

[8] A. C. Potter, I. Kimchi, and A. Vishwanath, Quantum oscillations from surface fermi arcs in weyl and dirac semimetals, Nature Communications **5**, 5161 (2014).

[9] S.-Y. Xu, I. Belopolski, N. Alidoust, M. Neupane, G. Bian, C. Zhang, R. Sankar, G. Chang, Z. Yuan, C.-C. Lee, S.-M. Huang, H. Zheng, J. Ma, D. S. Sanchez, B. Wang, A. Bansil, F. Chou, P. P. Shibayev, H. Lin, S. Jia, and M. Z. Hasan, Discovery of a weyl fermion semimetal and topological fermi arcs, Science **349**, 613 (2015), https://www.science.org/doi/pdf/10.1126/science.aaa9297.

[10] I. A. Leahy, Y.-P. Lin, P. E. Siegfried, A. C. Treglia, J. C. W. Song, R. M. Nandkishore, and M. Lee, Nonsaturating large magnetoresistance in semimet-

als, Proceedings of the National Academy of Sciences **115**, 10570 (2018), https://www.pnas.org/doi/pdf/10.1073/pnas.1808747115.

[11] Y. He, J. Gayles, M. Yao, T. Helm, T. Reimann, V. N. Strocov, W. Schnelle, M. Nicklas, Y. Sun, G. H. Fecher, and C. Felser, Large linear non-saturating magnetoresistance and high mobility in ferromagnetic mnbi, Nature Communications **12**, 4576 (2021).

[12] Q. Liu, P.-J. Guo, X.-Y. Yue, Z.-K. Yi, Q.-X. Dong, H. Liang, D.-D. Wu, Y. Sun, Q.-J. Li, W.-L. Zhu, T.-L. Xia, X.-F. Sun, and Y.-Y. Wang, Observation of surface superconductivity in a 3d dirac material, Advanced Functional Materials **32**, 2208616 (2022), https://advanced.onlinelibrary.wiley.com/doi/pdf/10.1002/adfm.202208616.

[13] D. Takane, Y. Kubota, K. Nakayama, T. Kawakami, K. Yamauchi, S. Souma, T. Kato, K. Sugawara, S.-i. Ideta, K. Tanaka, M. Kitamura, K. Horiba, H. Kumigashira, T. Oguchi, T. Takahashi, K. Segawa, and T. Sato, Dirac semimetal phase and switching of band inversion in xmg2bi2 (x = ba and sr), Scientific Reports **11**, 21937 (2021).

[14] A. K. Kundu, S. Pakhira, T. Roy, T. Yilmaz, M. Tsujikawa, M. Shirai, E. Vescovo, D. C. Johnston, A. N. Pasupathy, and T. Valla, Electronic and magnetic properties of the topological semimetal $smmg_2bi_2$, Phys. Rev. B **106**, 245131 (2022).

[15] Y. Zhang, Y. Deng, R. Xiong, K. Cheng, B. Chen, C. Wen, K. Cao, and W. Li, Multiband transport enables thermoelectric enhancements in the srmg2bi2 compound, Journal of Applied Physics **131**, 135101 (2022), https://pubs.aip.org/aip/jap/article-pdf/doi/10.1063/5.0081785/16457540/135101_1_online.pdf.

[16] C. Bigi, C. Jego, V. Polewczyk, A. De Vita, T. Jaouen, H. C. Tchouekem, F. Bertran, P. Le Fèvre, P. Turban, J.-F. Jacquot, J. A. Miwa, O. J. Clark, A. Jana, S. K. Chaluvadi, P. Orgiani, M. Cuoco, M. Leandersson, T. Balasubramanian, T. Olsen, Y. Hwang, M. Jamet, and F. Mazzola, Bilayer orthogonal ferromagnetism in crte2-based van der waals system, Nature Communications **16**, 4495 (2025).

[17] C. Bigi, M. Dürrnagel, L. Klebl, A. Consiglio, G. Pokharel, F. Bertran, P. L. Févre, T. Jaouen, H. C. Tchouekem, P. Turban, A. D. Vita, J. A. Miwa, J. W. Wells, D. Oh, R. Comin, R. Thomale, I. Zeljkovic, B. R. Ortiz, S. D. Wilson, G. Sangiovanni, F. Mazzola, and D. D. Sante, Pomeranchuk instability from electronic correlations in $csti_3bi_5$ kagome metal (2024), arXiv:2410.22929 [cond-mat.str-el].

[18] A. C. Pakpour-Tabrizi, A. K. Schenk, A. J. U. Holt, S. K. Mahatha, F. Arnold, M. Bianchi,

R. B. Jackman, J. E. Butler, A. Vikharev, J. A. Miwa, P. Hofmann, S. P. Cooil, J. W. Wells, and F. Mazzola, The occupied electronic structure of ultrathin boron doped diamond, Nanoscale Adv. **2**, 1358 (2020).

[19] A. D. Vita, C. Bigi, D. Romanin, M. D. Watson, V. Polewczyk, M. Zonno, F. Bertran, M. B. Petersen, F. Motti, G. Vinai, M. Tuniz, F. Cilento, M. Cuoco, B. M. Andersen, A. Kreisel, L. J. D'Onofrio, O. J. Clark, M. T. Edmonds, C. Candelora, M. Xu, S. Cheng, A. LaFleur, T. Antonelli, G. Sangiovanni, L. D. Re, I. Vobornik, J. Fujii, F. M. Granozio, A. Sambri, E. D. Gennaro, J. B. Jacobsen, H. Jacobsen, R. Ernstorfer, I. Zeljkovic, Y. Hwang, M. Calandra, J. A. Miwa, and F. Mazzola, Optical switching in a layered altermagnet (2025), arXiv:2502.20010 [cond-mat.str-el].

Supplementary Information: Uncovering surface states of the Dirac semimetal $BaMg_2Bi_2$

A. De Vita**, [1]J. Bakkelund**, [2]H. Świątek**, [3]M. J. Winiarski,[3] C. V. Nielsen,[4] F. Bertran,[5] F. Miletto Granozio,[6] J. A. Miwa,[4] T. Klimczuk,[3,*] C. Bigi,[7,†] and F. Mazzola[6,‡]

[1]*Fritz Haber Institut der Max Planck Gesellshaft, Faradayweg 4–6, 14195 Berlin, Germany*

[2]*Department of Engineering Sciences, University of Agder, NO-4879 Grimstad, Norway*

[3]*Faculty of Applied Physics and Mathematics, Advanced Materials Centre, Gdansk University of Technology, Narutowicza 11/12, 80-233, Gdansk, Poland*

[4]*Department of Physics and Astronomy, Interdisciplinary Nanoscience Center, Aarhus University, 8000 Aarhus C, Denmark*

[5]*Synchrotron SOLEIL, L'Orme des Merisiers, Départementale 128, F-91190 Saint-Aubin, France*

[6]*CNR-SPIN, c/o Complesso di Monte S. Angelo, IT-80126 Napoli, Italy*

[7]*Synchrotron SOLEIL, L'Orme des Merisiers, Départementale 28, 91190 Saint-Aubin, France*

** These authors contributed equally.

---

[*] Corresponding author: tomasz.klimczuk@pg.edu.pl

[†] Corresponding author: chiara.bigi@synchrotron-soleil.fr

[‡] Corresponding author: mazzola@iom.cnr.it

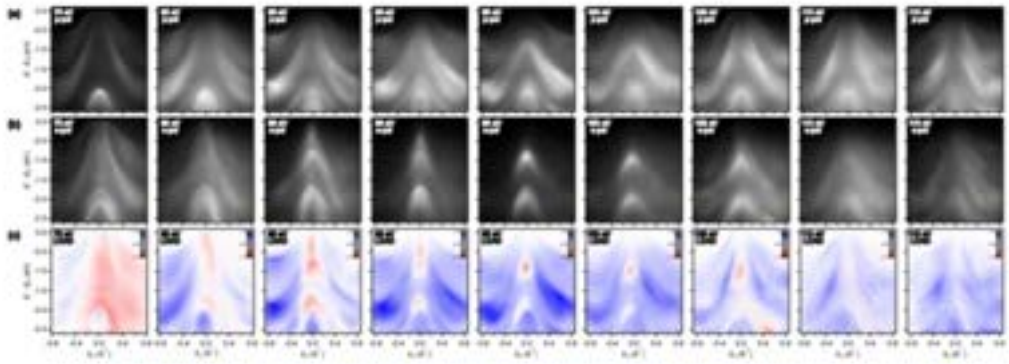

Figure 1. (a) Photon energy scans collected with linear horizontal (p-type) and (b) linear vertical (s-type) polarizations. (c) Corresponding linear dichroism obtained as 2×LH-LV. Blue color indicates a prevalence of states excited by the LH radiation. The data are collected with the slit parallel to the Γ-K direction.

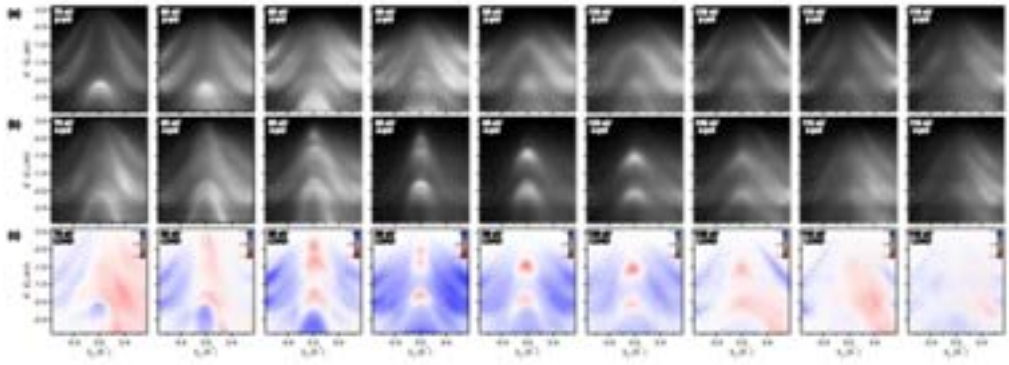

Figure 2. (a) Photon energy scans collected with linear horizontal (p-type) and (b) linear vertical (s-type) polarizations. (c) Corresponding linear dichroism obtained as 2×LH-LV. Blue color indicates a prevalence of states excited by the LH radiation. The data are collected with the slit parallel to the Γ-M direction.

Bibliography

[1] B. Keimer and J. E. Moore. "The physics of quantum materials". In: *Nature Physics* 13.11 (Oct. 2017), 1045–1055. ISSN: 1745-2481. DOI: 10.1038/nphys4302. URL: http://dx.doi.org/10.1038/nphys4302.

[2] Philip Ball. "Quantum materials: Where many paths meet". In: *MRS Bulletin* 42.10 (Oct. 2017), 698–705. ISSN: 1938-1425. DOI: 10.1557/mrs.2017.220. URL: http://dx.doi.org/10.1557/mrs.2017.220.

[3] Feliciano Giustino et al. "The 2021 quantum materials roadmap". In: *Journal of Physics: Materials* 3.4 (Oct. 2020), p. 042006. ISSN: 2515-7639. DOI: 10.1088/2515-7639/abb74e. URL: http://dx.doi.org/10.1088/2515-7639/abb74e.

[4] Vincent G. Harris and Parisa Andalib. "Modern quantum materials". In: *Frontiers in Materials* Volume 11 - 2024 (2024). ISSN: 2296-8016. DOI: 10.3389/fmats.2024.1343005. URL: https://www.frontiersin.org/journals/materials/articles/10.3389/fmats.2024.1343005.

[5] D. J. Thouless et al. "Quantized Hall Conductance in a Two-Dimensional Periodic Potential". In: *Physical Review Letters* 49.6 (Aug. 1982), 405–408. ISSN: 0031-9007. DOI: 10.1103/physrevlett.49.405. URL: http://dx.doi.org/10.1103/PhysRevLett.49.405.

[6] K. v. Klitzing, G. Dorda, and M. Pepper. "New Method for High-Accuracy Determination of the Fine-Structure Constant Based on Quantized Hall Resistance". In: *Physical Review Letters* 45.6 (Aug. 1980), 494–497. ISSN: 0031-9007. DOI: 10.1103/physrevlett.45.494. URL: http://dx.doi.org/10.1103/PhysRevLett.45.494.

[7] F. D. M. Haldane. "Model for a Quantum Hall Effect without Landau Levels: Condensed-Matter Realization of the "Parity Anomaly"". In: *Physical Review Letters* 61.18 (Oct. 1988), 2015–2018. ISSN: 0031-9007. DOI: 10.1103/physrevlett.61.2015. URL: http://dx.doi.org/10.1103/PhysRevLett.61.2015.

[8] C. L. Kane and E. J. Mele. "Quantum Spin Hall Effect in Graphene". In: *Physical Review Letters* 95.22 (Nov. 2005). ISSN: 1079-7114. DOI: 10.1103/physrevlett.95.226801. URL: http://dx.doi.org/10.1103/PhysRevLett.95.226801.

[9] C. L. Kane and E. J. Mele. "Z_2 Topological Order and the Quantum Spin Hall Effect". In: *Physical Review Letters* 95.14 (Sept. 2005). ISSN: 1079-7114. DOI: 10.1103/physrevlett.95.146802. URL: http://dx.doi.org/10.1103/PhysRevLett.95.146802.

[10] B. Andrei Bernevig, Taylor L. Hughes, and Shou-Cheng Zhang. "Quantum Spin Hall Effect and Topological Phase Transition in HgTe Quantum Wells". In: *Science* 314.5806 (Dec. 2006), 1757–1761. ISSN: 1095-9203. DOI: 10.1126/science.1133734. URL: http://dx.doi.org/10.1126/science.1133734.

[11] Markus Konig et al. "Quantum Spin Hall Insulator State in HgTe Quantum Wells". In: *Science* 318.5851 (Nov. 2007), 766–770. ISSN: 1095-9203. DOI: 10.1126/science.1148047. URL: http://dx.doi.org/10.1126/science.1148047.

[12] Y. Xia et al. "Observation of a large-gap topological-insulator class with a single Dirac cone on the surface". In: *Nature Physics* 5.6 (May 2009), 398–402. ISSN: 1745-2481. DOI: 10.1038/nphys1274. URL: http://dx.doi.org/10.1038/nphys1274.

[13] D. Hsieh et al. "A topological Dirac insulator in a quantum spin Hall phase". In: *Nature* 452.7190 (Apr. 2008), 970–974. ISSN: 1476-4687. DOI: 10.1038/nature06843. URL: http://dx.doi.org/10.1038/nature06843.

[14] D. Hsieh et al. "Observation of Unconventional Quantum Spin Textures in Topological Insulators". In: *Science* 323.5916 (Feb. 2009), 919–922. ISSN: 1095-9203. DOI: 10.1126/science.1167733. URL: http://dx.doi.org/10.1126/science.1167733.

[15] Nitesh Kumar et al. "Topological Quantum Materials from the Viewpoint of Chemistry". In: *Chemical Reviews* 121.5 (Nov. 2020), 2780–2815. ISSN: 1520-6890. DOI: 10.1021/acs.chemrev.0c00732. URL: http://dx.doi.org/10.1021/acs.chemrev.0c00732.

[16] M. G. Vergniory et al. "A complete catalogue of high-quality topological materials". In: *Nature* 566.7745 (2019), pp. 480–485. ISSN: 1476-4687. DOI: 10.1038/s41586-019-0954-4. URL: https://doi.org/10.1038/s41586-019-0954-4.

[17] Barry Bradlyn et al. "Topological quantum chemistry". In: *Nature* 547.7663 (2017), pp. 298–305. ISSN: 1476-4687. DOI: 10.1038/nature23268. URL: https://doi.org/10.1038/nature23268.

[18] URL: https://physics.ucf.edu/~rep/EDII/Onnes1911.pdf.

[19] 2025. URL: https://en.wikipedia.org/wiki/Meissner_effect.

[20] In: *Proceedings of the Royal Society of London. Series A - Mathematical and Physical Sciences* 149.866 (Mar. 1935), 71–88. ISSN: 2053-9169. DOI: 10.1098/rspa.1935.0048. URL: http://dx.doi.org/10.1098/rspa.1935.0048.

[21] V. L. Ginzburg and L. D. Landau. "On the Theory of Superconductivity". In: *On Superconductivity and Superfluidity*. Springer Berlin Heidelberg, 113–137. ISBN: 9783540680086. DOI: 10.1007/978-3-540-68008-6_4. URL: http://dx.doi.org/10.1007/978-3-540-68008-6_4.

[22] J. Bardeen, L. N. Cooper, and J. R. Schrieffer. "Theory of Superconductivity". In: *Physical Review* 108.5 (Dec. 1957), 1175–1204. ISSN: 0031-899X. DOI: 10.1103/physrev.108.1175. URL: http://dx.doi.org/10.1103/PhysRev.108.1175.

[23] J. Bardeen, L. N. Cooper, and J. R. Schrieffer. "Microscopic Theory of Superconductivity". In: *Physical Review* 106.1 (Apr. 1957), 162–164. ISSN: 0031-899X. DOI: 10.1103/physrev.106.162. URL: http://dx.doi.org/10.1103/PhysRev.106.162.

[24] M.L. Fornasini and F. Merlo. "Equiatomic ternary phases formed by alkaline earths and rare earths". In: *Journal of Alloys and Compounds* 219.1 (1995). Eleventh international conference on solid compounds of transition elements, pp. 63–68. ISSN: 0925-8388. DOI: https://doi.org/10.1016/0925-8388(94)05010-4. URL: https://www.sciencedirect.com/science/article/pii/0925838894050104.

[25] B. Eisenmann, G. Cordier, and Herbert Schäfer. "CaCuSb(Bi) und SrCuSb(Bi) - Ternäre Phasen im „aufgefüllten" NiAs-(Ni_2In)-Typ / CaCuSb(Bi) and SrCuSb(Bi) - Ternary Phases in the „Filled" NiAs-(Ni_2In)-Structure". In: *Zeitschrift für Naturforschung B* 29.7-8 (1974), pp. 457–459. DOI: doi:10.1515/znb-1974-7-801. URL: https://doi.org/10.1515/znb-1974-7-801.

[26] Albrecht Mewis. "Darstellung und Struktur der Verbindungen MgCuP, BaCuP(As) und BaAgP(As) / Preparation and Crystal Structure of MgCuP, BaCuP(As), and BaAgP(As)". In: *Zeitschrift für Naturforschung B* 34.10 (1979), pp. 1373–1376. DOI: doi:10.1515/znb-1979-1006. URL: https://doi.org/10.1515/znb-1979-1006.

[27] Albrecht Mewis. "CaAgP und CaAgAs -Zwei Verbindungen mit Fe2P-Struktur/CaAgP and CaAgAs -Two Compounds with the Fe2P-Structure". In: *Zeitschrift für Naturforschung B* 34.1 (1979), pp. 14–17. DOI: doi:10.1515/znb-1979-0105. URL: https://doi.org/10.1515/znb-1979-0105.

[28] Albrecht Mewis. "ABX-Verbindungen mit Ni2In-Struktur Darstellung und Struktur der Verbindungen CaCuP(As), SrCuP(As), SrAgP(As) und EuCuAs / ABX Compounds with the Structure Ni2In Preparation and Crystal Structure of CaCuP(As), SrCuP(As), SrAgP(As), and EuCuAs". In: *Zeitschrift für Naturforschung B* 33.9 (1978), pp. 983–986. DOI: doi:10.1515/znb-1978-0906. URL: https://doi.org/10.1515/znb-1978-0906.

[29] Dirk Johrendt, Reiner Miericke, and Albrecht Mewis. "Neue Pnictide mit modifizierten AIB2-Strukturen / New Pnictides with Modified AIB2-Type Structures". In: *Zeitschrift für Naturforschung B* 51.6 (1996), pp. 905–906. DOI: doi:10.1515/znb-1996-0625. URL: https://doi.org/10.1515/znb-1996-0625.

[30] F. Merlo, M. Pani, and M.L. Fornasini. "RMX compounds formed by alkaline earths, europium and ytterbium—I. Ternary phases with M Cu, Ag, Au; X Sb, Bi". In: *Journal of the Less Common Metals* 166.2 (1990), pp. 319–327. ISSN: 0022-5088. DOI: https://doi.org/10.1016/0022-5088(90)90014-B. URL: https://www.sciencedirect.com/science/article/pii/002250889090014B.

[31] R.-D. Hoffmann and Rainer Pöttgen. "AlB_2-related intermetallic compounds – a comprehensive view based on group-subgroup relations". In: *Zeitschrift für Kristallographie - Crystalline Materials* 216.3 (2001), pp. 127–145. DOI: doi:10.1524/zkri.216.3.127.20327. URL: https://doi.org/10.1524/zkri.216.3.127.20327.

[32] Rainer Pöttgen. "Coloring, Distortions, and Puckering in Selected Intermetallic Structures from the Perspective of Group-Subgroup Relations". In: *Zeitschrift für anorganische und allgemeine Chemie* 640.5 (2014), pp. 869–891. DOI: https://doi.org/10.1002/zaac.201400023. eprint:

https://onlinelibrary.wiley.com/doi/pdf/10.1002/zaac.201400023. URL: https://onlinelibrary.wiley.com/doi/abs/10.1002/zaac.201400023.

[33] K. Momma and F. Izumi. *VESTA 3 for three-dimensional visualization of crystal, volumetric and morphology data*. 2011.

[34] Lilia S. Xie et al. "Pressure-induced structural phase transition in the half-Heusler compound CaAuBi". In: *Solid State Sciences* 30 (2014), pp. 6–10. ISSN: 1293-2558. DOI: https://doi.org/10.1016/j.solidstatesciences.2014.02.001. URL: https://www.sciencedirect.com/science/article/pii/S1293255814000235.

[35] Melanie J. Kirkham et al. "*Abinitio* determination of crystal structures of the thermoelectric material MgAgSb". In: *Phys. Rev. B* 85 (14 2012), p. 144120. DOI: 10.1103/PhysRevB.85.144120. URL: https://link.aps.org/doi/10.1103/PhysRevB.85.144120.

[36] F. Merlo, M. Pani, and M.L. Fornasini. "Electrical resistivity of the RMBi phases with R = Ca, Yb and M = Cu, Ag, Au". In: *Journal of Alloys and Compounds* 221.1 (1995), pp. 280–283. ISSN: 0925-8388. DOI: https://doi.org/10.1016/0925-8388(94)01466-3. URL: https://www.sciencedirect.com/science/article/pii/0925838894014663.

[37] Sheng Xu et al. "Crystal growth of BaAgAs family topological materials via flux method". In: *Journal of Crystal Growth* 531 (2020), p. 125304. ISSN: 0022-0248. DOI: https://doi.org/10.1016/j.jcrysgro.2019.125304. URL: https://www.sciencedirect.com/science/article/pii/S0022024819305196.

[38] M. K. Hooda et al. "Magnetotransport properties of the topological semimetal SrAgBi". In: *Phys. Rev. B* 106 (4 2022), p. 045107. DOI: 10.1103/PhysRevB.106.045107. URL: https://link.aps.org/doi/10.1103/PhysRevB.106.045107.

[39] Nahyun Lee et al. "Pressure-Dependent Superconductivity in Topological Dirac Semimetal SrCuBi". In: *Advanced Materials* 36.29 (2024), p. 2400428. DOI: https://doi.org/10.1002/adma.202400428. eprint: https://advanced.onlinelibrary.wiley.com/doi/pdf/10.1002/adma.202400428. URL: https://advanced.onlinelibrary.wiley.com/doi/abs/10.1002/adma.202400428.

[40] Hidefumi Takahashi et al. "Superconductivity in a ferroelectric-like topological semimetal SrAuBi". In: *npj Quantum Materials* 8.1 (2023), 1–7. DOI: https://doi.org/10.1038/s41535-023-00612-4. URL: https://www.nature.com/articles/s41535-023-00612-4.

[41] Yongping Du et al. "Dirac and Weyl Semimetal in XYBi (X=Ba, Eu; Y=Cu, Ag and Au)". In: *Scientific Reports* 5.1 (2015). DOI: https://doi.org/10.1038/srep14423.

[42] Shengshan Qin et al. "Topological critical materials of ternary compounds". In: *Journal of Physics and Chemistry of Solids* 128 (2019). Spin-Orbit Coupled Materials, pp. 218–224. ISSN: 0022-3697. DOI: https://doi.org/10.1016/j.jpcs.2017.12.006. URL: https://www.sciencedirect.com/science/article/pii/S0022369717316396.

[43] Q. D. Gibson et al. "Three-dimensional Dirac semimetals: Design principles and predictions of new materials". In: *Phys. Rev. B* 91 (20 2015), p. 205128. DOI: 10.1103/PhysRevB.91.205128. URL: https://link.aps.org/doi/10.1103/PhysRevB.91.205128.

[44] Chanchal K. Barman et al. "Symmetry-driven topological phases in XAgBi(X = Ba, Sr): An ab initio hybrid functional calculation". In: *Phys. Rev. Mater.* 4 (8 2020), p. 084201. DOI: 10.1103/PhysRevMaterials.4.084201. URL: https://link.aps.org/doi/10.1103/PhysRevMaterials.4.084201.

[45] Sougata Mardanya et al. "Prediction of threefold fermions in a nearly ideal Dirac semimetal BaAgAs". In: *Phys. Rev. Mater.* 3 (7 2019), p. 071201. DOI: 10.1103/PhysRevMaterials.3.071201. URL: https://link.aps.org/doi/10.1103/PhysRevMaterials.3.071201.

[46] Chiranjit Mondal et al. "Broken symmetry driven phase transitions from a topological semimetal to a gapped topological phase in SrAgAs". In: *Phys. Rev. B* 99 (20 2019), p. 205112. DOI: 10.1103/PhysRevB.99.205112. URL: https://link.aps.org/doi/10.1103/PhysRevB.99.205112.

[47] Zhixiang Hu et al. "Robust three-dimensional type-II Dirac semimetal state in SrAgBi". In: *npj Quantum Materials* 8.1 (2023). DOI: https://doi.org/10.1038/s41535-023-00549-8.

[48] Qinqing Zhu et al. "Shubnikov-de Haas oscillations and electronic structure in the Dirac semimetal SrAgAs". In: 104.14, 144305 (2021), p. 144305. DOI: 10.1103/PhysRevB.104.144305.

[49] Cong Chen et al. "Ternary wurtzite CaAgBi materials family: A playground for essential and accidental, type-I and type-II Dirac fermions". In: *Phys. Rev. Mater.* 1 (4 2017), p. 044201. DOI: 10.1103/PhysRevMaterials.1.044201. URL: https://link.aps.org/doi/10.1103/PhysRevMaterials.1.044201.

[50] Ai Yamakage et al. "Line-Node Dirac Semimetal and Topological Insulating Phase in Noncentrosymmetric Pnictides CaAgX (X = P, As)". In: *Journal of the Physical Society of Japan* 85.1 (2016), p. 013708. DOI: 10.7566/JPSJ.85.013708. eprint: https://doi.org/10.7566/JPSJ.85.013708. URL: https://doi.org/10.7566/JPSJ.85.013708.

[51] Jayita Nayak et al. "Electronic properties of topological insulator candidate CaAgAs". In: *Journal of Physics: Condensed Matter* 30 (Jan. 2018). DOI: 10.1088/1361-648X/aaa1cd.

[52] Eve Emmanouilidou et al. "Magnetotransport properties of the single-crystalline nodal-line semimetal candidates $CaTX(T = \mathrm{Ag, Cd}; X = \mathrm{As, Ge})$". In: *Phys. Rev. B* 95 (24 2017), p. 245113. DOI: 10.1103/PhysRevB.95.245113. URL: https://link.aps.org/doi/10.1103/PhysRevB.95.245113.

[53] Jiawei Zhang et al. "Chemical bonding origin of the unexpected isotropic physical properties in thermoelectric Mg_3Sb_2 and related materials". In: *Nature Communications* 9.1 (2018), p. 4716. ISSN: 2041-1723. DOI: 10.1038/s41467-018-06980-x. URL: https://doi.org/10.1038/s41467-018-06980-x.

[54] Klaus Deller and Brigitte Eisenmann. "Ternäre Erdalkali-Element(V)-Verbindungen AMg_2B_2 mit A = Ca, Sr, Ba und B = As, Sb, Bi / Ternary Alkaline Earth-Element(V)-Compounds AMg_2B_2 with A = Ca, Sr, Ba and B = As, Sb, Bi". In: *Zeitschrift für Naturforschung B* 32.6 (1977), pp. 612–616. DOI: doi:10.1515/znb-1977-0602. URL: https://doi.org/10.1515/znb-1977-0602.

[55] Peter Klüfers et al. "AB2X2-Verbindungen im CaAl2Si2-Typ, VIII [1] / AB2X2 Compounds with the CaAl2Si2 Structure, VIII [1]". In: *Zeitschrift für Naturforschung B* 35.10 (1980), pp. 1317–1318. DOI: doi:10.1515/znb-1980-1029. URL: https://doi.org/10.1515/znb-1980-1029.

[56] Andrew F. May et al. "Structure and Properties of Single Crystalline $CaMg_2Bi_2$, $EuMg_2Bi_2$, and $YbMg_2Bi_2$". In: *Inorganic Chemistry* 50.21 (2011). PMID: 21999768, pp. 11127–11133. DOI: 10.1021/ic2016808. URL: https://doi.org/10.1021/ic2016808.

[57] Zeying Zhang et al. "High-Throughput Screening and Automated Processing toward Novel Topological Insulators". In: *The Journal of Physical Chemistry Letters* 9.21 (2018), pp. 6224–6231. DOI: 10.1021/acs.jpclett.8b02800. URL: https://doi.org/10.1021/acs.jpclett.8b02800.

[58] D. Takane et al. "Dirac semimetal phase and switching of band inversion in XMg_2Bi_2 (X = Ba and Sr)". In: *Scientific Reports* 11 (2021), p. 21937. DOI: https://doi.org/10.1038/s41598-021-01333-z. URL: https://www.nature.com/articles/s41598-021-01333-z.

[59] Qi Liu et al. "Observation of Surface Superconductivity in a 3D Dirac Material". In: *Advanced Functional Materials* 32.51 (2022), p. 2208616. DOI: https://doi.org/10.1002/adfm.202208616. URL: https://onlinelibrary.wiley.com/doi/abs/10.1002/adfm.202208616.

[60] L.G. Akselrud, Ya. P. Yarmolyuk, and E. I. Gladyshevskii. "Crystal structures of $U_4Re_7Si_6$ and $U_4(Re_{0.17}Si_{0.83})_{13}$, Volume = Ser. A, Year = 1978". In: *Dopov Akad Nauk Ukr RSR* (), p. 359.

[61] N. Engel, B. Chabot, and E. Parthé. "$Sc_4T_7Ge_6$ (T ; Rh, Ir, Os, Ru) and Sc4Ir7Si6 with the cubic $U_4Re_7Si_6$-type structure". In: *Journal of the Less Common Metals* 96 (1984), pp. 291–296. ISSN: 0022-5088. DOI: https://doi.org/10.1016/0022-5088(84)90207-8. URL: https://www.sciencedirect.com/science/article/pii/0022508884902078.

[62] Samir F. Matar, Bernard Chevalier, and Rainer Pöttgen. "The $U_4Re_7Si_6$ type – Trends in electronic structure and chemical bonding". In: *Solid State Sciences* 27 (2014), pp. 5–10. ISSN: 1293-2558. DOI: https://doi.org/10.1016/j.solidstatesciences.2013.10.008. URL: https://www.sciencedirect.com/science/article/pii/S1293255813002914.

[63] F. Wastin et al. "New actinide ternary intermetallic compounds: synthesis, characterization and physical properties". In: *Journal of Alloys and Compounds* 210.1 (1994), pp. 83–89. ISSN: 0925-8388. DOI: https://doi.org/10.1016/0925-8388(94)90119-8. URL: https://www.sciencedirect.com/science/article/pii/0925838894901198.

[64] Inga Schellenberg et al. "Ternary Antimonides RE4T7Sb6 (RE=Gd–Lu; T =Ru, Rh) with Cubic $U_4Re_7Si_6$-type Structure". In: *Zeitschrift für Naturforschung B* 68.9 (2013), pp. 971–978. DOI: doi:10.5560/znb.2013-3181. URL: https://doi.org/10.5560/znb.2013-3181.

[65] H Noël, M Potel, and D Kaczorowski. "A new ternary uranium arsenide, U4Ru7As6". In: *Journal of Alloys and Compounds* 302.1 (2000), pp. L1–L2. ISSN: 0925-8388. DOI: https://doi.org/10.1016/S0925-8388(99)00584-8. URL: https://www.sciencedirect.com/science/article/pii/S0925838899005848.

[66] A. Wurth, A. Löhken, and A. Mewis. "Neue ternäre Rhodium- und Iridium-Phosphide und -Arsenide mit $U_4Re_7Si_6$-Struktur". In: *Zeitschrift für anorganische und allgemeine Chemie* 627.6 (2001), pp. 1213–1216. DOI: https://doi.org/10.1002/1521-3749(200106)627:6<1213::AID-ZAAC1213>3.0.CO;2-Z. URL: https://onlinelibrary.wiley.com/doi/abs/10.1002/1521-3749\%28200106\%29627\%3A6\%3C1213\%3A\%3AAID-ZAAC1213\%3E3.0.CO\%3B2-Z.

[67] A. Leithe-Jasper et al. "Crystal structure of tetraytterbium septarhodium hexaantimony, $Yb_4Rh_7Sb_6$". In: *Zeitschrift für Kristallographie - New Crystal Structures* 221.3 (2006), pp. 255–256. DOI: doi:10.1524/ncrs.2006.0062. URL: https://doi.org/10.1524/ncrs.2006.0062.

[68] Inga Schellenberg, Matthias Eul, and Rainer Pöttgen. "Intermediate-Valent Yb4Rh7Sb6 with Cubic $U_4Re_7Si_6$ type structure". In: *Zeitschrift für Kristallographie* 225.8 (2010), pp. 339–341. DOI: doi:10.1524/zkri.2010.1255. URL: https://doi.org/10.1524/zkri.2010.1255.

[69] Yusuke Hirose et al. "Antiferromagnetic order in $Yb_4Ru_7As_6$ with the cubic $U_4Re_7Si_6$-type structure". In: *Journal of Magnetism and Magnetic Materials* 556 (2022), p. 169327. ISSN: 0304-8853. DOI: https://doi.org/10.1016/j.jmmm.2022.169327. URL: https://www.sciencedirect.com/science/article/pii/S0304885322002712.

[70] J Paglione, N P Butch, and E E Rodriguez. *Fundamentals of Quantum Materials*. WORLD SCIENTIFIC, 2021. DOI: 10.1142/11799. eprint: https://www.worldscientific.com/doi/pdf/10.1142/11799. URL: https://www.worldscientific.com/doi/abs/10.1142/11799.

[71] Brian H. Toby and Robert B. Von Dreele. "GSAS-II: the genesis of a modern open-source all purpose crystallography software package". In: *Journal of Applied Crystallography* 46.2 (2013), pp. 544–549. DOI: https://doi.org/10.1107/S0021889813003531. eprint: https://onlinelibrary.wiley.com/doi/pdf/10.1107/S0021889813003531. URL: https://onlinelibrary.wiley.com/doi/abs/10.1107/S0021889813003531.

[72] Souvik Sasmal et al. "Magnetotransport properties of noncentrosymmetric CaAgBi single crystal". en. In: *J Phys Condens Matter* 32.33 (May 2020).

[73] Zhong-Ming Sun et al. "Synthesis and crystal structure of CaAgBi and $BaAg_{1.837}Bi_2$". In: *Journal of Alloys and Compounds* 430.1 (2007), pp. 71–76. ISSN: 0925-8388. DOI: https://doi.org/10.1016/j.jallcom.2006.05.001. URL: https://www.sciencedirect.com/science/article/pii/S0925838806004889.

[74] Jian Wang et al. "$Ca_{1-x}RE_xAg_{1-y}Sb$ (RE = La, Ce, Pr, Nd, Sm; $0 \leq x \leq 1; 0 \leq y \leq 1$) : $InterestingStructuralTransformationandEnhancedHigh-TemperatureThermoelectricPerformance$". In: *Journal of the American Chemical Society* 135.32 (2013). PMID: 23869609, pp. 11840–11848. DOI: 10.1021/ja403653m. eprint: https://doi.org/10.1021/ja403653m. URL: https://doi.org/10.1021/ja403653m.

[75] A. Moll et al. "SrCuP and SrCuSb Zintl phases as potential thermoelectric materials". In: *Journal of Alloys and Compounds* 942 (2023), p. 169123. ISSN: 0925-8388. DOI: https://doi.org/10.1016/j.jallcom.2023.169123. URL: https://www.sciencedirect.com/science/article/pii/S0925838823004267.

[76] Akira Iyo et al. "Large enhancement of superconducting transition temperature of $SrBi_3$ induced by Na substitution for Sr". In: *Scientific Reports* 5.1 (2015), p. 10089. ISSN: 2045-2322. DOI: 10.1038/srep10089. URL: https://doi.org/10.1038/srep10089.

[77] B. T. Matthias et al. "Many More Superconducting Bismuth Phases". In: *Phys. Rev. Lett.* 17 (12 1966), pp. 640–643. DOI: 10.1103/PhysRevLett.17.640. URL: https://link.aps.org/doi/10.1103/PhysRevLett.17.640.

[78] Zhipeng Hou et al. "Large low-field positive magnetoresistance in nonmagnetic half-Heusler ScPtBi single crystal". In: *Applied Physics Letters* 107.20 (Nov. 2015), p. 202103. ISSN: 0003-6951. DOI: 10.1063/1.4936179. eprint: https://pubs.aip.org/aip/apl/article-pdf/doi/10.1063/1.4936179/14472495/202103_1_online.pdf. URL: https://doi.org/10.1063/1.4936179.

[79] R. M. Moon et al. "Magnetic Structures of Er_2O_3 and Yb_2O_3". In: *Phys. Rev.* 176 (2 1968), pp. 722–731. DOI: 10.1103/PhysRev.176.722. URL: https://link.aps.org/doi/10.1103/PhysRev.176.722.

[80] D. Kaczorowski et al. "Magnetic, thermodynamic, and electrical transport properties of ternary equiatomic ytterbium compounds YbTM(T = transition metal, M = Sn and Bi)". In: *Phys. Rev. B* 60 (1 1999), pp. 422–433. DOI: 10.1103/PhysRevB.60.422. URL: https://link.aps.org/doi/10.1103/PhysRevB.60.422.

[81] Santanu Pakhira, M. A. Tanatar, and D. C. Johnston. "Magnetic, thermal, and electronic-transport properties of $EuMg_2Bi_2$ single crystals". In: *Phys. Rev. B* 101 (21 2020), p. 214407. DOI: 10.1103/PhysRevB.101.214407. URL: https://link.aps.org/doi/10.1103/PhysRevB.101.214407.

[82] Michał Winiarski et al. "$MgPd_2Sb$: A Mg-based Heusler-type superconductor". In: *Physical Review B* 103 (21 June 2021), p. 214501. DOI: 10.1103/PhysRevB.103.214501.

[83] Hanna Świątek et al. "Superconductivity in Ternary $Mg_4Pd_7As_6$". In: *Advanced Electronic Materials* 11.2 (2025), p. 2400284. DOI: https://doi.org/10.1002/aelm.202400284. eprint: https://advanced.onlinelibrary.wiley.com/doi/pdf/10.1002/aelm.202400284. URL: https://advanced.onlinelibrary.wiley.com/doi/abs/10.1002/aelm.202400284.

[84] Yogesh Singh et al. "Multigap superconductivity and Shubnikov–de Haas oscillations in single crystals of the layered boride OsB_2". In: *Phys. Rev. B* 82 (14 2010), p. 144532. DOI: 10.1103/PhysRevB.82.144532. URL: https://link.aps.org/doi/10.1103/PhysRevB.82.144532.

[85] K Katoh et al. "Magnetic and transport properties of $Yb_4Rh_7Ge_6$ and $Yb_4Ir_7Ge_6$". In: *Journal of Magnetism and Magnetic Materials* 279.1 (2004), pp. 118–124. ISSN: 0304-8853. DOI: https://doi.org/10.1016/j.jmmm.2004.01.075. URL: https://www.sciencedirect.com/science/article/pii/S0304885304001337.

[86] S. A. M. Mentink et al. "Thermal, electrical, and magnetic properties of $U_4Ru_7Ge_6$". In: *Journal of Applied Physics* 69.8 (Apr. 1991), pp. 5484–5486. ISSN: 0021-8979. DOI: 10.1063/1.348942.

[87] A. Wurth and A. Mewis. "Neue Rhodiumverbindungen mit $LiCo_6P_4$-Struktur". In: *Zeitschrift für anorganische und allgemeine Chemie* 625.3 (1999), pp. 449–452. DOI: https://doi.org/10.1002/(SICI)1521-3749(199903)625:3<449::AID-ZAAC449>3.0.CO;2-L. URL: https://onlinelibrary.wiley.com/doi/abs/10.1002/\%28SICI\%291521-

3749\%28199903\%29625\%3A3\%3C449\%3A\%3AAID-ZAAC449\%3E3.0.CO\%3B2-L.

[88] H. Okamoto. "The P-Pd (phosphorus-palladium) system". In: *Journal of Phase Equilibria* 15.1 (1994), pp. 1054–9714. DOI: 10.1007/BF02667684. URL: https://doi.org/10.1007/BF02667684.

List of Figures

List of Tables